ABSTRACT

Title of Document: AMOEBOID SHAPE DYNAMICS ON FLAT AND TOPOGRAPHICALLY MODIFIED SURFACES

Meghan Katrien Driscoll,
Doctor of Philosophy, 2012

Directed By: Professor Wolfgang Losert,
Department of Physics

I present an analysis of the shape dynamics of the amoeba *Dictyostelium discoideum*, a model system for the study of cellular migration. To better understand cellular migration in complicated 3-D environments, cell migration was studied on simple 3-D surfaces, such as cliffs and ridges. *D. discoideum* interact with surfaces without forming mature focal adhesion complexes (FACs). The cellular response to the surface topography was characterized by measuring and looking for patterns in cell shape. Dynamic cell shape is a measure of the interaction between the internal biochemical state of a cell and its external environment.

For *D. discoideum* migrating on flat surfaces, waves of high boundary curvature were observed to travel from the cell front to the cell back. Curvature waves are also easily seen in cells that do not adhere to a surface, such as cells that are electrostatically repelled from the coverslip or cells that are extended over the edge of micro-fabricated cliffs. At the leading edge of adhered cells, these curvature

waves are associated with protrusive activity, suggesting that protrusive motion can be thought of as a wave-like process. The wave-like character of protrusions provides a plausible mechanism for the ability of cells to swim in viscous fluids and to navigate complex 3-D topography.

Patterning of focal adhesion complexes has previously been implicated in contact guidance (polarization or migration parallel to linear topographical structures). However, significant contact guidance is observed in *D. discoideum,* which lack focal adhesion complexes. Analyzing the migration of cells on nanogratings of ridges spaced various distances apart, ridges spaced about 1.5 μm apart were found to guide cells best. Contact guidance was modeled as an interaction between wave-like processes internal to the cell and the periodicity of the nanograting. The observed wavelength and speed of the oscillations that best couple to the surface are consistent with those of protrusive dynamics. Dynamic sensing via actin or protrusive dynamics might then play a role in contact guidance.

AMOEBOID SHAPE DYNAMICS
ON FLAT AND TOPOGRAPHICALLY MODIFIED SURFACES

By

Meghan Katrien Driscoll

Dissertation submitted to the Faculty of the Graduate School of the
University of Maryland, College Park, in partial fulfillment
of the requirements for the degree of
Doctor of Philosophy
2012

Advisory Committee:
Professor Wolfgang Losert, Chair
Professor Jose Helim Aranda-Espinoza, Dean's Representative
Professor John T. Fourkas
Adjunct Professor Carole Parent
Professor Arpita Upadhyaya

Acknowledgements

Most of all, I would like to thank my advisor, Wolfgang Losert, who is genuinely kind and always enthusiastic. I would also like to thank John Fourkas, who is always available to give advice. Carole Parent for being so kind to so many physicists for so long. Kan Cao for her willingness to jump into a new field at the spur of the moment. Professor Peter Saeta, my undergraduate research advisor, and Professor Richard Haskell, my instructor for multiple undergrad labs, who never let us follow the procedures in the lab manual.

I would like to thank everyone in the Losert, Fourkas, and Parent labs. Especially the Losert lab's Dicty crowd: Can Guven, Colin McCann, Xiaoyu Sun, and Chenlu Wang. Paul Kriebel, without whom we would not have cells, and Linjie Li, who showed me how to fabricate an amoeba obstacle course. Also, Jason Albanese, Floyd Bates, Beatriz Burrola, Desu Chen, Rafael Gattass, Derin Guven, Deborah Hemingway, Mark Herrera, Tess Homan, Rael Kopace, Peter Kordell, George Kumi, Rachel Lee, Linjie Li, Mitch Mailman, Kathleen Monaco, EChO Ory, Joshua Parker, Andrew Pomerance, Erin Rericha, and Steve Slotterback.

My loving husband, Mark Kegel, who gladly came along for the ride. Thank You! My parents, Matt and Marleigh Driscoll, who always encouraged me to pursue my interests. My grandmother, Sylva Driscoll, who embraced life, perhaps more so than anyone else I've ever met. Audy Sederberg, a friend who feels as if she is family. Anita Roychowdhury and Shane Squires, who are great housemates and great friends. Meem Mahmud, who approaches life so wholeheartedly. And of course,

Emmy, Carrie, Abby, and Chelsea, who over the years have provided me with much support and many hours of entertainment.

Finally, I thank the members of my committee: Professor Wolfgang Losert, Professor Jose Helim Aranda-Espinoza, Professor John T. Fourkas, Adjunct Professor Carole Parent, and Professor Arpita Upadhyaya.

Table of Contents

List of Figures

Chapter 1. Introduction

Almost all nucleated cells migrate at some stage during their development (1). Cellular migration is key to phenomena as diverse as wound healing, embryonic development, angiogenesis, and cancer metastasis (2-5). In this thesis, I study the physics of cellular migration. The amoeba *Dictyostelium discoideum*, a model system for the study of cellular migration, is observed migrating on flat and topographically modified surfaces. The cellular response to the surface topography is characterized by measuring cell shape dynamics. Dynamic cell shape is a measure of the interaction between a cell's internal processes and its external environment.

1.1. A physical approach to cell biology

The two overriding methodologies of contemporary cell biology are genetics and biochemistry. In a genetics-based approach, chemical pathways are discovered by knocking down genes and then observing the resultant characteristics of the mutated cell. In a biochemistry-based approach, the characteristics of proteins are assessed and the interrelationships among proteins are measured. Genetics and biochemistry have both had enormous success in elucidating cellular processes, but they are not the only possible approaches to cell biology. Cell biology can also be approached from a physical perspective.

What is a physical approach to cell biology? The physical approach to the study of biological shape is usually traced back to *On Growth and Form,* which was published by D'arcy Wentworth Thompson in 1917 (6). He wrote

> Cell and tissue, shell and bone, leaf and flower, are so many portions of matter, and it is in obedience to the laws of physics that their particles have been moved, molded and conformed.... Their problems of form are in the first instance mathematical problems, their problems of growth are essentially physical problems, and the morphologist is, *ipso facto*, a student of physical science.

Thompson argued that the biology of his day was dominated by teleological arguments springing from both evolution and religion. While he appreciated the evolution-based teleological arguments, he thought that biological study would benefit from multiple approaches. In particular, he advocated an approach that is quantitative and that uses physical laws to seek underlying mechanisms. The first example he chose to explain his approach was amoeba shape. He chose amoebae, presumably, to emphasize that even their apparently inexplicable shape dynamics could be studied mechanistically via physical laws.

A recent exploration of the physical approach to cell biology is presented in the textbook *Physical Biology of the Cell* written by Rob Phillips, Jane Kondev, and Julie Theriot (7). Quantitative modeling, the authors argue, is at the heart of a physical approach to cell biology. They write that quantitative models provide a necessary quantitative 'view' or perspective from which to understand quantitative data. Nevertheless, ninety years after Thompson presented his case for a physical approach to biology, the authors write

> We wonder whether the quantitative modeling approach we have explored in this book can ever become one of the foundational pillars of biological research on the brink of new discovery, standing

> alongside genetics and biochemistry as an exploratory method, or whether modeling will typically be relegated to the later stages of biological investigation, as a method for dotting the i's and crossing the t's for biological problems that are already fairly well-understood, when the real intrepid explorers have moved on. In our view, the jury is still out on the extent to which the physical biology perspective will shed new light on important biological problems or will lead to new insights into physics.

Unlike the genetics- and biochemistry-based approaches, which can each on their own solve standard problems in cell biology, for such problems the physical approach may only ever act as an accompaniment to the other two. Of course, biochemistry and genetics usually accomplish more in concert than individually. Using sample data sets, Wong *et al.* attempted to determine if a biochemical or genetic approach was better at discovering functional relationships between genes and proteins (8). They found, perhaps unsurprising, that combining both datasets yielded better results than using just one dataset. A physical approach that only aided genetics and biochemistry could still be a powerful and useful addition to the field. Perhaps more importantly, though, a field's reigning methodologies in part determine its essential, open questions. A physical approach has the potential to bring not only new techniques to cell biology but also to partially redefine the field by generating new questions.

1.2. How do cells migrate?

Cell migration is varied and depends upon many factors, including the cell type, the chemical and physical properties of the extracellular matrix, and the interactions between cells (1). Despite this great variety, cell migration can be reduced to a few modes. Friedl *et al.* described typical modes of individual and

collective cell migration (1). The pseudopodial amoeboid mode of cell migration, which is investigated in this thesis, is characterized by weakly adhesive cells, no mature focal adhesion complexes, and relatively rapid migration (1). Leukocytes, dendritic cells, and *D. discoideum* are reported to migrate in a pseudopodial amoeboid fashion (1).

The migration of an individual cell can be summarized as a series of discrete steps. Sheetz *et al.* divided cell migration into five typical steps: extension of the cell front, adhesion of the front to the surface, contraction of the cytoplasm, retraction of the back, and recycling of membrane receptors (9). Pseudopodial amoeboid migration, broken into steps, is shown in Figure 1. An amoeba migrates and changes shape mostly by protruding at its front and retracting at its back.

The shape and motion of amoeboid cells are governed by actin dynamics. Recent reviews describe actin in detail (10-12). Actin, one of the principal components of the cytoskeleton, helps to maintain both cell integrity and cell responsiveness via polymerization and depolymerization. Actin dynamics are controlled by numerous actin-binding proteins and are regulated by various chemical pathways. Protrusive motion is the direct result of the force exerted on the cell membrane by actin polymerization. One of the earlier models of this force posited that it could be understood as an "elastic Brownian ratchet" (13).

Categorizing cell migration into modes and breaking down the process of cell migration into steps can yield insights. However, both cell shape dynamics and the actin dynamics that underlie and govern shape dynamics have been shown to exhibit more complicated behaviors (14, 15). Exploring these more complicated behaviors,

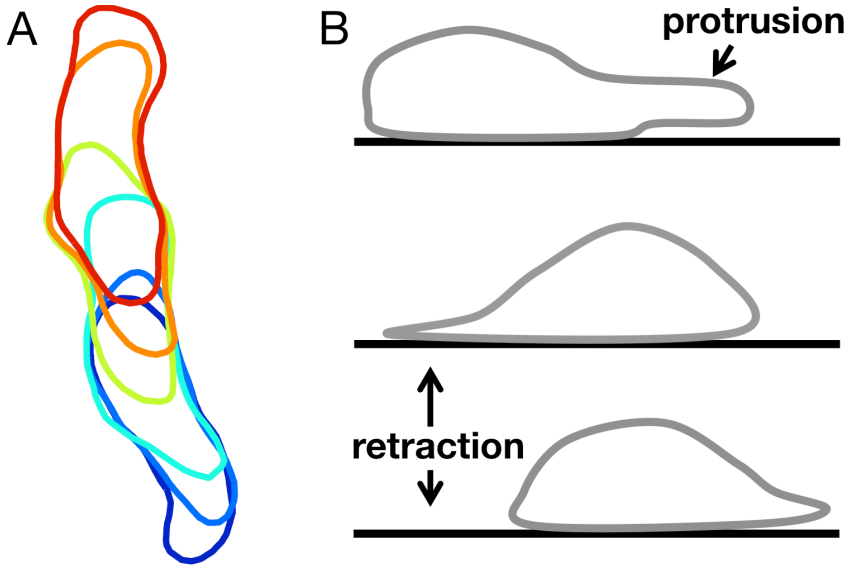

Figure 1.1. **Amoeboid migration. (A) Overlaid shapes of a migrating *D. discoideum* cell. The initial cell shape is blue, while the final shape is red. In general, amoebae migrate by extending protrusions at their front in a zig-zagging manner and retracting their back. (These shapes were measured from microscopy images as described in Chapter 2.) (B) A schematic that shows a side-view of amoeboid migration. *D. discoideum* do not extend and adhere protrusions simultaneously. Instead, protrusions are extended and then ~20 sec later planted on the surface (16).**

may yield insights into how cells avoid obstacles and migrate in 3-D environments. Early studies found waves of protrusive movement in the cell shape dynamics of *D. discoideum* and keratocytes (17, 18). Actin polymerization was also found to exhibit wave-like dynamics (19, 20). For example, Gerisch *et al*. observed actin waves in *D. discoideum* cells recovering from actin depolymerization (19). Weiner *et al.* found that Hem-1, an activator of actin nucleation in HL-60 cells, spreads outward from foci in waves (see Figure 1.2) (20). Waves in cell shape, protrusive motion, and actin

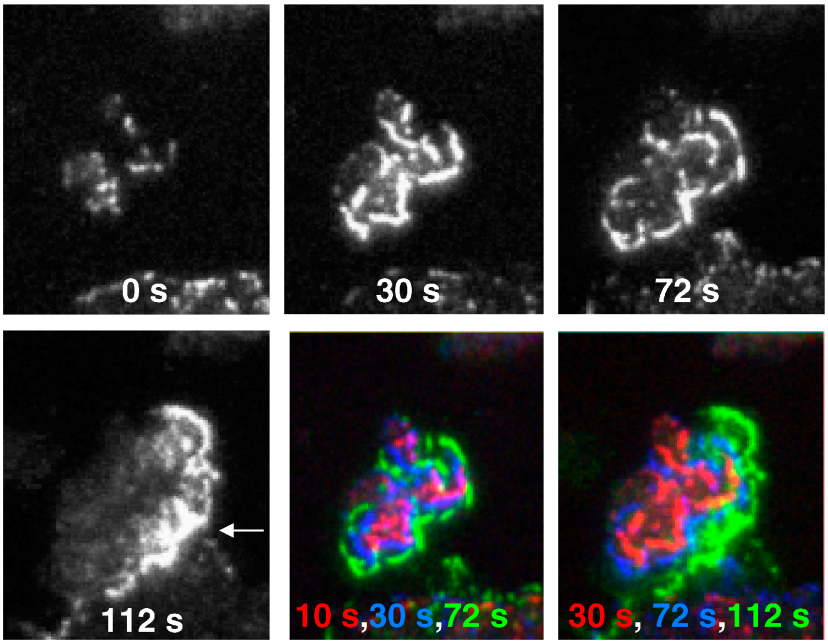

Figure 1.2. **Hem-1 waves in HL-60 cells exposed to a chemoattractant. Hem-1 is a component of the WAVE2 complex, an activator of actin nucleation in HL-60 cells. Here, Hem-1 waves propagate outward from foci and form a band at the cell's leading edge, which is denoted by the arrow. (This figure was reproduced from (20) under the CC BY License.)**

dynamics have now been observed in multiple cell types by multiple groups (21-25). Actin polymerization has recently been hypothesized to be an excitable system (14, 25, 26). In an excitable system a perturbation above a threshold results in a large response, while a perturbation below that threshold results in no response or a small response. Like waves in some excitable systems, colliding actin waves have been observed to annihilate one another (20, 27, 28).

1.3. Surface properties affect cell migration and shape

The surface on which cells migrate is an important, but sometimes overlooked, component of the cell migration machinery. Cellular behavior is affected by physical and chemical properties of the surface, such as rigidity, adhesivity, and shape. In particular, multiple studies have found that substrate rigidity affects cell behavior (29-32). Pelham and Wang found that fibroblasts and epithelial cells that are adhered to soft substrates show reduced spreading and increased protrusive activity compared to cells adhered to more rigid surfaces (30). Substrate rigidity also affects cellular differentiation (33, 34).

Another characteristic of the surface, its adhesivity, alters the shape dynamics of keratocytes (22). On a surface of low adhesion strength the keratocyte front moves forward irregularly, on a surface of intermediate adhesion strength the entire cell front moves forward smoothly, and on a surface of high adhesion strength regions of the cell front move forward in waves (see Figure 1.3). Surface adhesion does not obviously affect the shape dynamics of the amoeba *D. discoideum* (35). Chapter 3 describes the cell shape dynamics of *D. discoideum* that are not adhered to a surface.

Confining cells to 2-D regions of various sizes and shapes can also affect cells. 2-D patterns of cell-binding proteins can be fabricated using micro-contact printing (36). Culturing human mesenchymal stem cells (hMSCs) on small islands of binding proteins promotes adipogenesis, while culturing them on large islands promotes osteogenesis (37). For islands of the same area, shapes with high local curvature (i.e., pointy shapes) promote osteogenesis, while smoother island shapes promote adipogenesis (38).

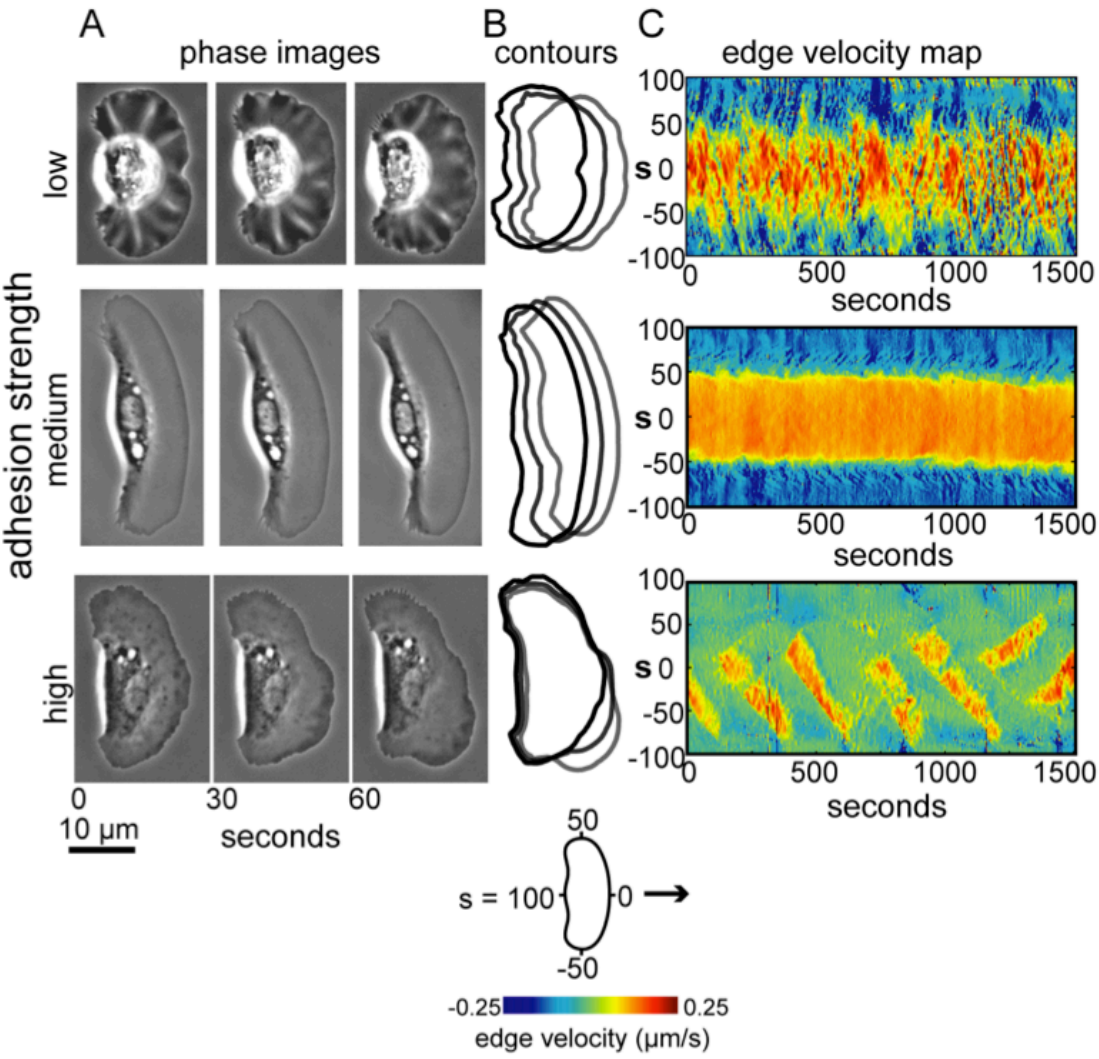

Figure 1.3. **Surface adhesion strength affects the shape dynamics of keratocytes. (A) Phase contrast images, (B) contours, and (C) edge velocities of keratocytes on surfaces of various adhesion strengths. On a low adhesion strength surface the cell front moves forward irregularly, on an intermediate adhesion strength surface the entire cell front moves forward smoothly, and on a high adhesion strength surface the cell front moves forward in waves. (This figure was reproduced from (22) under the CC BY License.)**

The effects of various micro and nanoscale 3-D substrates have also been investigated (39-47). Fibroblasts on nanocolumns have smaller mean areas and have

more filopodia per perimeter length than do cells on flat surfaces (41). Various cell types are guided by linear topographical structures, such as ridges and grooves (39, 48, 49). Cellular orientation or migration parallel to linear topographical structures is termed contact guidance. Chapter 5 describes the contact guidance and cell shape dynamics of *D. discoideum* migrating on nano-ridges and grooves.

1.4. Dictyostelium discoideum*: Our model organism for cellular migration*

In this thesis, I analyze the effect of surface topography on the shape dynamics of *Dictyostelium discoideum*. The social amoeba *D. discoideum* is a model system for the study of cellular migration and chemotaxis. Key components of the gradient-sensing pathway and the actin polymerization machinery are conserved between *D. discoideum* and neutrophils (50). However, unlike mammalian cells, *D. discoideum* do not have focal adhesion complexes.

D. discoideum were first isolated in 1933 from forest soil in North Carolina (51). While normally unicellular, when starved, these social amoebae aggregate to become a slug-like multi-cellular organism (52). The slug migrates to a new location, differentiates into spore and stalk cells, and then releases spores. Figure 1.4A shows the lifecycle of *D. discoideum*. The self-aggregation of cells is mediated by their controlled release of the chemoattractant cyclic adenosine monophosphate (cAMP). The intricate, spatially and temporally evolving pattern of cAMP release can result in multiple aggregations centers, each of which develop into a multi-cellular organism (see Figure 1.4B). Starved cells both release and follow cAMP. As a result, cells

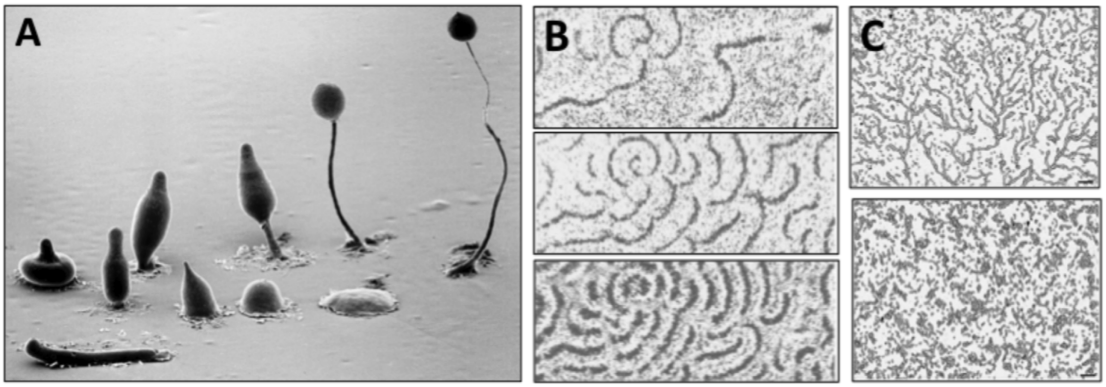

Figure 1.4. **The lifecycle of *Dictyostelium discoideum*. (A) When starved, *D. discoideum* amoebae can aggregate to form a slug-like organism. This multi-cellular organism migrates to a new location, differentiates into spore and stalk cells, and then releases spores. In this image, a slug is shown in the lower left corner, while the remaining structures show the transformation from a slug into a spore-producing organism. (Image Copyright, M. J. Grimson & R. L. Blanton, Biological Sciences Electron Microscopy Laboratory, Texas Tech University) (B) *D. discoideum* aggregate by releasing coordinated waves of cAMP. This image sequence shows cAMP wave patterns at 321, 368, and 422 minutes after the cells were placed on the surface. (These images were reproduced from (53) with permission. Copyright (1997) National Academy of Sciences, USA.) (C) Aggregating *D. discoideum* form characteristic streaming patterns. Wild-type streaming patterns (upper image) are different than some mutant streaming patterns, for example *pdsA*- cells (lower image) patterns. *pdsA*- cells lack pdsA, the main phosphodiesterase that degrades extracellular cAMP. (This figure was reproduced from (54) under the CC BY-NC-SA 3.0 License.)**

follow one another in a head to tail manner known as streaming. Streaming cells can form complicated spatial patterns that vary from mutant to mutant (see Figure 1.4C).

The enzyme adenylyl cyclase generates cAMP. *Aca-* cells migrate towards, but do not release, cAMP, and so do not self-aggregate (55).

The release of cAMP is the most studied oscillation in *D. discoideum*. In order to avoid the complexities of aggregation into a multi-cellular organism, early studies of cAMP oscillations were sometimes conducted as light scattering experiments in stirred solutions of cells (56). These cAMP oscillations have a 5-10 minute period, which shortens by about 25% over ten periods (56). While light-scattering oscillations were later found to be associated with oscillations in cAMP, light-scattering oscillations are most likely the direct result of shape oscillations (56, 57).

1.5. Measuring and analyzing the shapes of migrating cells

When an amoeba moves, it changes shape by extending protrusions or retracting its back. Conversely, an amoeba's shape is the result of its protrusive and retractive activity over the last few minutes. Biological structure (cellular shape) and function (cellular motion) are here thus closely related. Cellular shape is a highly visible measure of the interaction between a cell's internal cytoskeleton and its external environment. Measuring dynamic cell shapes then allows us to probe not only the internal cellular state but also the cellular response to the external environment.

A wide variety of methods have been used to measure dynamic cell shape. The measurement process is usually broken up into multiple steps (58). First, image segmentation (i.e., splitting an image into discrete, distinct regions) is performed to find the cell boundaries in each frame. Next, the boundary points in each frame (or

boundary regions) are associated with boundary points in the next frame. Finally, patterns in the dynamic cell shape are found and analyzed.

Image segmentation of fluorescence images can be performed using simple image analysis operations, for example smoothing and then thresholding the image. Phase-contrast and Differential Interference Contrast (DIC) images require a more complicated image segmentation algorithm, such as that described in (59). However, a sequence of such simple operations will likely neither be robust to variation between images nor detect cell boundaries to sub-pixel resolution. Snake, or active contour, algorithms (60) can fix both of these problems. In a snake algorithm, a force field is calculated from the image. Next, an object, such as a loop or a line segment, with physical properties is allowed to deform iteratively in response to the force field. If the algorithm has run correctly, the position of the object will converge to the position of the cell boundary.

To measure the dynamic cell shape, we need not only the cell boundaries but also the local evolution of the boundaries from frame to frame. One way to track boundary motion locally is via level sets (61), which were first used by Machacek and Danuser to analyze dynamic cell shape (21). In the level-set tracking algorithm, each boundary is defined as the level set (at height zero) of a surface in three dimensions. The magnitude of the surface height, which is a function of the spatial image coordinates x and y, is the distance in image space from (x,y) to the nearest point on the cellular boundary. The surface height is defined as positive inside the boundary and negative outside of it. The local boundary is tracked by continuously evolving the surface in each frame into the surface in the next frame. The ability to propagate

the boundary continuously from one frame to the next is an advantage of using level sets, which could allow some measures to be defined simply and intuitively. However, while level-set methods are conceptually appealing, they tend to be computationally slow.

An alternative to level sets is parameterization of the boundary as a series of landmarks, such as boundary points, and then tracking of those landmarks from frame to frame. Landmarks have been used in multiple studies (62-65). The software suite Quimp2 (63) uses a modified snake algorithm both to extract cell shapes and to track boundary points from frame to frame. In most snake algorithms, the snake is parameterized by a variable number of boundary points. During convergence of the snake, if adjacent boundary points become closer or farther apart than distances preset by the user, boundary points are removed or added. In the algorithm that Quimp2 uses, boundary points in the initial frame are first labeled. Next, the boundary is expanded and new boundary points with higher-valued labels are added between existing boundary points. This expanded boundary is used to initialize an active contour algorithm in the next frame. When the boundary converges, boundary points with higher valued labels are preferentially removed. Same-labeled boundary points then essentially act as tracking markers that float along the cell boundary as the cell moves. Incorporating tracking into the snake algorithm is computationally efficient; however, since the resultant boundary point mapping from frame to frame is not 1:1, the measures that can use this mapping are limited. In Chapter 2, we describe a tracking algorithm that is computationally faster than level sets but uses 1:1 boundary point mappings from frame to frame.

The high dimensionality of cell shape dynamics has led to a variety of analysis approaches. The approach chosen depends on how the shape dynamics have been parameterized. Analyzing the centroid motion of cells, Li *et al.* found that while *D. discoideum* move with a persistence time of ~10 minutes, they do so by zig-zagging in a left-right-left-right fashion (66, 67). Other studies have looked for patterns in protrusions (68-70). Andrew and Insall studied how protrusions bias the motion of chemotaxing *D. discoideum* (68). They found that while the location of new protrusions is independent of the chemotactic signal, protrusions extended in the signal direction have longer average lifetimes than other protrusions. While patterns in protrusion dynamics can provide insights into the underlying biology, from the cell shape alone there is not one obvious way to distinguish between protrusions. Machacek and Danuser measured protrusive motion as a continuous function of position along the boundary (21). Analyzing the dynamic shape of epithelial cells, they found that these cells are usually in one of two protrusive/retractive states. In the *I-state,* long boundary regions alternately protrude and retract, while in the *V-state*, protrusive bursts initiate waves of protrusive activity that travel transversely along the boundary in both directions. Maeda *et al.* found that *Dictyostelium discoideum,* like epithelial cells, are often in distinct states (71). They measured the distance, as a function of angle, from the cell centroid to the boundary. From the autocorrelations of this measure, they observed that cells were typically in states of elongation, rotation, or oscillation.

1.6. Thesis outline

A metastasizing cancer cell and a lymphocyte chasing an invader both migrate through complex 3-D environments. Cells are often studied migrating on flat surfaces, such as coverslips, or migrating through complex 3-D structures that mimic what they encounter *in vivo*. To develop better understanding of cell migration in complicated 3-D environments, I studied cells migrating on simple 3-D surfaces. I analyzed the motion of the amoeba *Dictyostelium discoideum*, a model system for the study of directed cellular migration. *D. discoideum* interact with surfaces without forming focal adhesion complexes. I characterized the cellular response to the surface shape by measuring and looking for patterns in cell shape. Dynamic cell shape is a highly visible manifestation of the interaction between the internal biochemical state of a cell and its external environment.

I observed cells traversing various simple 3-D obstacles, such as tall ridges, cliffs, and tight ropes. A published movie, *The Adventures of Dicty the* Dictyostelium *Cell* shows cells on these topographies (see Appendix A). On 3-D surfaces cells exhibit more complex behavior than simple migration. For instance, cells are observed to swing from the tops of tall ridges and cliffs.

To quantify the dynamic shapes of cells migrating on flat, glass coverslips, I developed a suite of shape-analysis tools. Global and local metrics highlight distinct cellular processes. For example, a global measure of shape shows rhythmic oscillations suggestive of contractions, whereas a local measure of shape shows wave-like dynamics indicative of protrusions. I extracted the times and locations of

protrusions and retractions and observed that protrusions zigzag, while retractions remain roughly stationary along the boundary. For more details, see Chapter 2.

In Chapter 2 I analyze the migration of *D. discoideum* moving on flat surfaces, whereas in Chapter 3 I analyze the migration of *D. discoideum* moving without a surface. Cell interaction with the null surface (no surface) provides a control for understanding the cellular response to 3-D shapes. For cells adhered to flat surfaces, waves of high boundary curvature travel from the cell front to the cell back. In adhered cells, these waves are stationary relative to the surface. Curvature waves can also be seen in cells not adhered to a surface, such as cells that are electrostatically repelled from the coverslip or cells that are extended over the edge of micro-fabricated cliffs. Without surface contact, curvature waves travel from the leading edge to the back of a cell at ~35 mm/min. At the leading edge of adhered cells, curvature waves are associated with protrusive activity, suggesting that protrusive motion could be thought of as a wave-like process. The wave-like character of protrusions provides a plausible mechanism for the swimming of cells in viscous fluids and the navigation of cells in complex 3-D topography.

An application of my shape analysis tools to prematurely aged nuclei, a system very different than amoeba, is shown in Chapter 4. The phenotypic hallmark of the premature aging disorder Hutchinson-Gilford progeria syndrome (HGPS) is abnormally shaped, blebbed nuclei (76, 77). Blebbing is normally measured by manual, blind counting; however, the extent of blebbing varies considerably within each cell population. I developed automated nuclear shape analysis software that quantitatively measures blebbing as well as other nuclear morphology features.

I next analyzed the migration of cells on simple surfaces, periodic nanogratings composed of parallel ridges. Many types of cells have been observed to exhibit contact guidance. Contact guidance is polarization or migration parallel to linear topographical structures (40, 45, 46, 48, 49, 72, 73). Patterning of focal adhesion complexes has previously been implicated in contact guidance (49, 74, 75). However, I observed significant contact guidance of *D. discoideum* along ridges and grooves, even though *D. discoideum* lack focal adhesion complexes. Since we previously (see Chapter 3) found that protrusive motion can be thought of as a wave-like process, we hypothesized that contact guidance might result from an interaction between a wave-like process internal to the cell and the periodicity of the nanograting. Analyzing the migration of cells on nanogratings of ridges spaced various distances apart, it is found that ridges spaced about 1.5 μm apart best guide cells. Contact guidance was modeled in terms of cellular stochastic harmonic oscillators that couple to the ridge periodicity. The oscillation wavelength that is in resonance with the nanograting is consistent with that of protrusive dynamics, which suggests a dynamic contact guidance process. For more details, see Chapter 5. Appendix B describes the shape analysis software used in Chapter 5.

Cell shape dynamics are high dimensional. This high dimensionality presents a barrier to both our qualitative and quantitative understanding of shape dynamics. In Chapter 6, we present some preliminary dimensionality reductions of cell shape dynamics. We used principal component analysis to find the principal components of shape, the global shape measure (the distance from the shape's centroid to each boundary point), and boundary curvature. In future, we plan to analyze the principal

component dynamics, compare ensembles of cells, and examine how topographical and chemical signals couple to cell shape.

Chapter 2. Local and global measures of shape dynamics

This chapter is adapted from Driscoll, Fourkas, and Losert (78). Text and figures are reproduced here with permission. Meghan Driscoll performed the experiments and analyzed the data.

2.1. Overview

The shape and motion of cells can yield significant insights into the internal operation of a cell. We present a simple, yet versatile framework that provides multiple metrics of cell shape and cell shape dynamics. Analysis of migrating *Dictyostelium discoideum* cells shows that global and local metrics highlight distinct cellular processes. For example, a global measure of shape shows rhythmic oscillations suggestive of contractions, whereas a local measure of shape shows wave-like dynamics indicative of protrusions. From a local measure of dynamic shape, or boundary motion, we extract the times and locations of protrusions and retractions. We find that protrusions zigzag, while retractions remain roughly stationary along the boundary. We do not observe any temporal relationship between protrusions and retractions. Our analysis framework also provides metrics of the boundary as whole. For example, as the cell speed increases, we find that the cell shape becomes more elongated. We also observe that while extensions and retractions have similar areas, their shapes differ.

2.2. Background

In this chapter, we analyze the shape dynamics of amoebae moving on flat surfaces. We also introduce a set of shape analysis tools that will be used throughout this thesis.

The quantitative study of shapes has been applied successfully to distinguish and classify a wide range of biological organisms and organs (21, 64, 79-81). At the cellular scale, the shapes of cell groups, individual cells, and intracellular components yield significant insights into cell behavior. For example, the shapes of cell nuclei in tumor tissues can assist in predicting therapy response (82).

While the above examples involve static shape analysis, the time dependence of cell shape can provide important information about the underlying dynamics. Studies of activated cell spreading reveal that the shapes of spreading cells have wave-like dynamics, which hints at a relationship to underlying actin polymerization waves (28). The dynamic shapes of migrating cells and their nuclei were measured in pioneering studies by the Soll group. They found, for example, that nuclear speed is linked to the establishment of surface contacts, and that nuclear shape changes with cell speed (83). The amoeba *Dictyostelium discoideum*, which was used in the Soll study, is a model system for amoeboid migration and chemotactic signaling. Since *D. discoideum* is able to migrate at speeds of up to tens of micrometers per second, it is well suited to the study of shape dynamics. Advances in imaging speed, in resolution, and in the ability to analyze large numbers of images are now allowing for further insights from the systematic study of cell shape dynamics.

Several approaches have emerged for measuring shape dynamics and integrating shape information with other data, such as the location of intracellular biochemical signals. The Danuser group developed a technique that uses the local shape dynamics of leading edge protrusions to connect fluorescent signals from multiple experiments (84). They used this approach to show that GTPases operate in sequence by first generating (RhoA) and then stabilizing (Rac1 and CDC42) protrusions at the leading edge of migrating mouse embryonic fibroblasts.

The shapes of migrating *D. discoideum* cells are being investigated by multiple researchers, including Insall (85) and van Haastert (69). They have found that protrusions alternate in an ordered way, which leads to a zigzaging migratory pattern on short time-scales. Maeda *et al.* found ordered patterns in cell shape (71).

Here we introduce a modular, robust approach for measuring shape dynamics that allows for the systematic quantification of multiple aspects of cell behavior. We apply this approach to the study of protrusions and retractions during amoeboid cell migration. We show that analysis of the shape dynamics of large numbers of cells can provide new insights into the mechanisms of cell migration. By combining different analysis modules, we capture how different underlying processes operate together, providing a more complete description of cell dynamics. A key aspect of our analysis is the use of complementary complete representations of cell shape that provide different perspectives and highlight distinct physical processes.

2.3. Results

2.3.1. Local and global measures of shape highlight different processes

We extracted the shape of self-aggregating, wild-type *D. discoideum* cells using a modified snake algorithm (86). A snake can be thought of as a physical object that has properties such as rigidity and tension, and that moves in response to a force. A force field that is generated from the image of the cell causes the snake's position to converge towards the cellular boundary. Figure 2.1A shows the overlapped, extracted shapes of a cell that was imaged every 4 seconds.

In each frame, our modified snake algorithm outputs the cell boundary as a list of 400 equally-spaced boundary points. To analyze how cell shape evolves in time, we track the local boundary by defining a 1:1 mapping between boundary points in successive frames. For each pair of frames, we chose the 1:1 mapping that kept neighboring boundary points neighboring and that minimized the sum of the distances between each boundary point and the point to which it maps. Combined, these two choices select a unique 1:1 mapping. By minimizing the sum of the distances between mapped to boundary points, we minimize the rotation of the boundary between frames. Note that the mapping is not intended to reflect motion of specific lipids or membrane proteins, which may drift apart in regions in which the plasma membrane is renewed and converge in regions in which the plasma membrane is recycled. If the movement of a membrane marker were tracked, that information could also be incorporated into the mapping. Figure 2.1C shows an example of our 1:1 mapping. In this figure, the initial boundary is shown with a solid black line, the

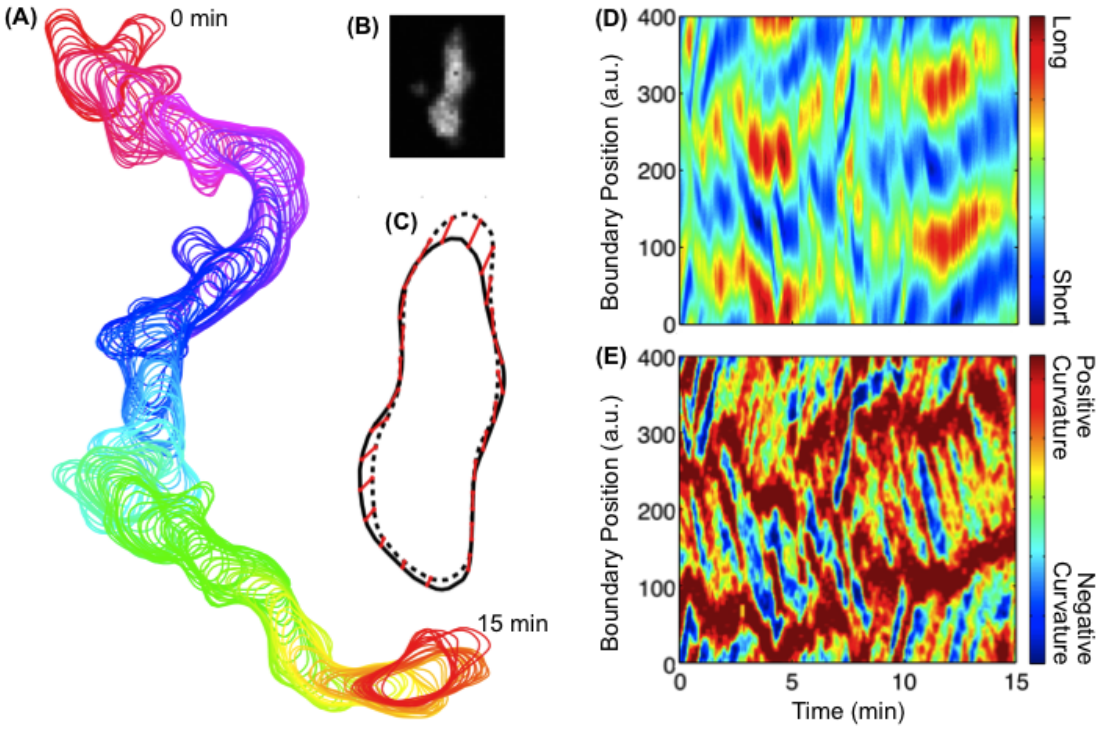

Figure 2.2. **Analysis of dynamic cell shape. (A) The extracted cell shapes of a self-aggregating, wildtype *D. discoideum* cell imaged every 4 seconds for 15 minutes. (B) A fluorescence image of a cytoplasmically dyed *D. discoideum* cell. (C) To track the boundary from frame to frame we defined a 1:1 tracking mapping between the boundary points in successive frames. Shown is an example of this least-squares tracking mapping. The boundary of the same cell is shown as a solid black line, the boundary in the next frame as a dashed black line, and every 15th mapping vector as a red line. (D) The global shape kymograph of the cell shown. We defined global shape as the distance from each boundary point to the centroid of the boundary. Here, red represents boundary regions that are far from the centroid, while blue represents regions that are near to the centroid. (E) The boundary curvature, or local shape, kymograph of the same cell. Regions of high curvature travel from the front to the back of the cell.**

boundary in the subsequent frame is shown with a dashed black line, and every 15th mapping vector is shown with a red line.

Tracking each boundary point from frame to frame allows us to follow the evolution of measures that are associated with boundary points. To explore cell shape dynamics, we used two boundary-point-associated measures of shape, one of which was global and the other local. Here, we distinguish global and local measures by their response to a local perturbation. With a global measure, changing the position of one boundary point affects the measure along the entire boundary. With a local measure, changing the position of one boundary point only affects the measure near that boundary point. We used the distance from each boundary point to the centroid of the boundary as a global measure of shape and used the boundary curvature as a local measure of shape. Both of these measures are complete descriptions of shape. (The fundamental theory of curves is that curvature is a complete description of cell shape (87).)

Measures associated with boundary points can be plotted as kymographs. Imagine coloring the cell boundaries by the value of a specific measure, cutting each boundary at boundary point zero, pulling the boundaries straight and then lining them up next to each other. This procedure yields space-time plots, or kymographs such as those shown in Figures 2.1D and 1E, which represent the global and local shape of the cell shown in Figure 21A. In both of these plots, the horizontal axis is time and the vertical axis is the position along the boundary. In both kymographs, the front of the cell is initially between boundary points 200 and 300 while the back is between boundary points 0 and 100.

In the global shape kymograph, redder regions are farther from the boundary centroid, while bluer regions are nearer to the centroid. Thus, the more intense the red and blue in a particular frame, the more polarized the cell is. Looking at the global shape kymograph, we see that the direction of polarization stays roughly the same, but that the amount of polarization increases and decreases in bursts. Additionally, thin lines connect the front and the back of the cell. These lines are regions that are an unusually large distance from the centroid and that travel from the cell front to the cell back. While barely visible in the global shape kymograph, these lines are readily apparent in the curvature, or local shape, kymograph. Based on analysis of many such curvature kymographs, we find that waves of high boundary curvature are generally generated at the fronts of cells and propagate towards their backs along roughly alternating sides (see Chapter 3).

The 1:1 tracking mapping described above allows us to define, visualize, and compare multiple measures. The ability to define new measures quickly and to compare those measures easily to existing measures can be more useful than having one excellent, but complicated, measure. Even if we were only interested in one measure, a measure of a complex system can sometimes be more easily understood in the context of other, related measures of that system than on its own.

2.3.2. Comparison of our 1:1 tracking mapping to other mapping approaches

A constant number of boundary points and the 1:1 tracking mapping described above are helpful when visualizing cell shape dynamics. However, the curvature

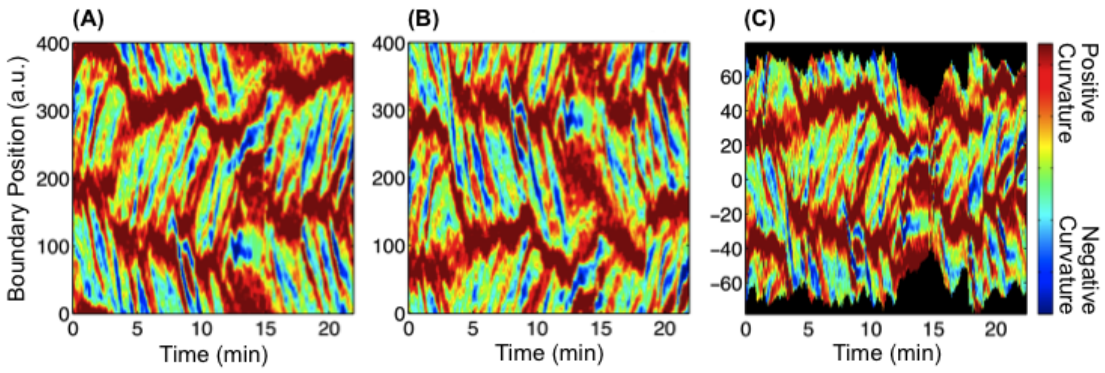

Figure 2.2. **Curvature waves can be visualized using multiple boundary point mappings. (A) The boundary curvature kymograph of a self-aggregating wild-type cell. (B) A boundary curvature kymograph for the same cell made with a different tracking mapping. The boundary point closest to 0° was used to align the boundary points from frame to frame. (C) The same cell's curvature with the distance between boundary points kept constant for all frames, so that a variable number of boundary points are aligned using the boundary point closest to 0°.**

waves require neither a specific tracking mapping nor a constant number of boundary points for visualization. Kymographs can be constructed from boundaries with a variable number of boundary points by using some specific boundary point, such as the one closest to 0° relative to the center of the cell, to align the boundaries from frame to frame. Figure 2.2A shows a standard curvature kymograph, as described above, while Figure 2.2B shows the corresponding plot with the boundary point closest to 0° used to define a 1:1 tracking mapping. As long as the boundary movement between frames is small, these two mappings usually yield similar kymographs. In Figure 2.2C the distance between boundary points is kept constant for all frames, and so a variable number of boundary points are aligned using the boundary point closest to 0°. Curvature waves are still present with this different

tracking mapping and a variable number of boundary points. However, with a variable number of boundary points, the kymograph is only informative near the alignment point - the location of a point on the other side of the cell will appear to fluctuate in the kymograph simply because the cell diameter changes. This kymograph is thus unnecessarily difficult to analyze directly.

2.3.3. Extracting local and global motion measures for dynamic cell shapes

To compare cell shape to cell motion, we require a measure of motion. Since the 1:1 mapping tracks boundary points from frame to frame, the magnitude of the displacement of a boundary point can be thought of as its speed. Figure 2.3A shows the magnitude of this displacement over 3 frames, or 12 seconds. The speed of a boundary point moving away from the cell boundary was made positive, while the speed of a boundary point moving towards the cell boundary was made negative. In this figure, we see bursts of protrusive activity, which appear as dark red vertical lines. While this global measure shows that cells move forward, at least in part, via bursts of activity, it gives information about the shape of protrusions. Instead, we can subtract the centroid position before defining the tracking mapping. Figure 2.3B shows the magnitude of the resultant displacement between the same labeled boundary points. Here, we again see bursts of activity, which appear as red and blue lines. As we might expect from the boundary curvature kymographs, however, some of these red and blue lines are slanted, indicating that motion sometimes travels along the cell boundary.

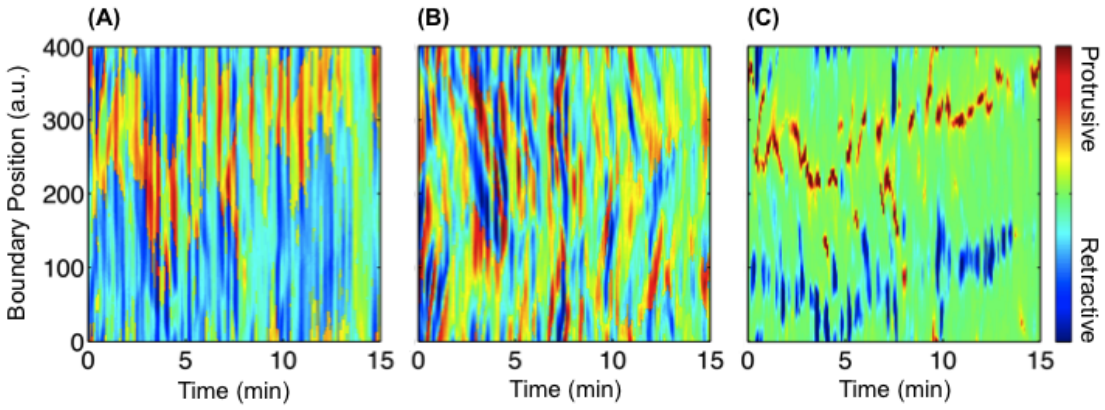

***Figure 2.3*. Analyzing boundary motion. (A) The global motion kymograph of the cell shown in Figure 2.1. Red and yellow represent boundary regions that are moving away from the cell boundary, while blue represents regions that are moving towards the cell boundary. (B) A global motion kymograph of the same cell with the centroid position subtracted before the tracking mapping was found. (C) The local motion kymograph of the same cell. Red represents protrusive boundary regions, while blue represents retractive boundary regions.**

The kymographs in Figures 2.3A and B both show global measures of motion. We usually think of protrusions, however, as localized events. We define a local measure of motion by mapping each boundary point to the closest boundary point in the frame 12 seconds later, smoothing the list of mapped-to boundary points, and then taking the magnitude of each mapping vector. For boundary points moving away from the cell, the local motion measure is made positive, while for boundary points moving towards the cell, the local motion measure is made negative. Figure 2.3C shows a kymograph of this local motion measure.

2.3.4. Protrusion and retraction statistics extracted for local motion metrics

The local motion kymograph in Figure 2.3 shows the motion of the entire boundary over the duration of an image sequence. Since we quantified all of the boundary motion in the image sequence, we can analyze protrusive motion as continuous boundary motion. We analyze the wave-like nature of protrusive boundary motion in Chapter 3. However, one can also analyze protrusive motion as a series of protrusions. Looking at the local motion measure in Figure 2.3, we see that protrusions (and retractions) have varying magnitudes and sometimes blend into one another. Individual protrusions and retractions might then be difficult to distinguish. However, in order to compare our results to the work of others and to show that our method can be used to distinguish protrusions, we analyzed individual protrusion and retraction statistics.

We extract individual protrusions by first smoothing the local motion measure over a window of 3 frames and 3 boundary points. Next, we set negative values, which correspond to retractive motion, of the smoothed measure to zero. We also set to zero positive values that are less than a noise threshold of 1 pixel moved over 12 seconds (3 frames). A protrusion is then defined as a peak in this processed local motion measure. Retractions are defined similarly. Note that this procedure finds even very small protrusions and retractions as long as the smoothed measure is larger than the noise threshold. Figure 2.4A shows an example of extracted protrusions and retractions. In the analysis of 26 wildtype, self-aggregating cells, we found a total of 2219 protrusions and 2220 retractions. Cells on average experienced 2.9 ± 0.2

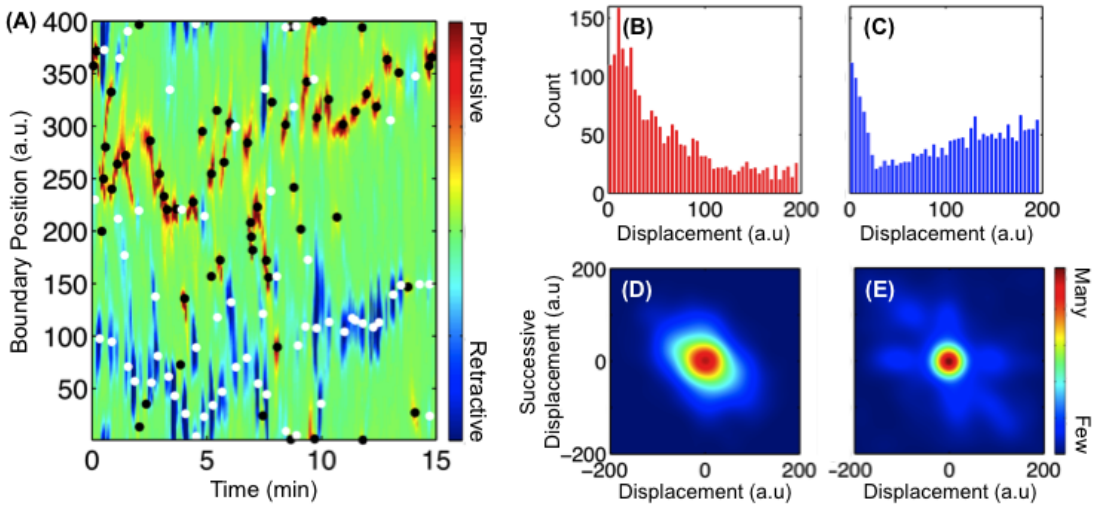

Figure 2.4. **Protrusions and retractions can be analyzed as discrete events. (A) The positions of protrusions and retractions were extracted from the plot shown in Figure 2.3C. Protrusions are shown as black dots, while retractions are shown as white dots. We extracted protrusions and retractions for 26 cells. (B) The distributions of the magnitude of the separations along the boundary between successive protrusions and (C) successive retractions. (D) The separation along the boundary between successive protrusions at the front plotted against the separation between the previous pair of successive protrusions at the front. The tilted distribution indicates that protrusions zig-zag. (E) The corresponding plot for retractions at the back. The predominately circular distribution indicates that successive retractions do not zig-zag.**

protrusions/minute and 2.9 ± 0.2 retractions/minute. Boosgraaf *et al.* found a similar frequency of four protrusions/minute (69).

We might expect a regular spatial relationship between successive protrusions or retractions. For example, a protrusion might occur some regular distance away from the previous protrusion. We measured the displacement along the boundary between successive protrusions and successive retractions (see Figures 2.4B and C).

For retractions, the peak in the distribution of the displacement magnitude occurs near zero. However, for protrusions the peak occurs at 3% of the boundary length. In other words, while a retraction tends to occur close to the location of the previous retractions, a protrusion is more likely to be slightly offset from the location of the previous protrusion. We also find that retractions are least likely to occur 8% of the boundary length away from the previous retraction. A retraction is then more likely to occur far from the previous retraction (at some location greater than 8% of the boundary away) than it is to occur nearby (8% of the boundary away), but not close to (a location less than 8% of the boundary away), the location of the previous retraction. The spatial relationship between successive retractions is not surprising since retractions can be caused by either a contraction of the cell back or a pulling in of a failed protrusion.

Not all protrusions occur in the front of the cell, and not all retractions occur in the back. To calculate statistics specifically for protrusions at the front of the cell and retractions at the back, we split each cell boundary into front and back regions. First, we smoothed the local motion measure using a Gaussian filter with a standard deviation of 25 frames and 25 boundary points. Then, boundary points with a smoothed value greater than zero were defined as being in the front of the cell, while those with a value less than zero were defined as being in the back. In other words, a retraction that is surrounded, both along the boundary and in time, by mostly protrusive motion would be defined as occurring in the front of the cell, while a protrusion that is mostly surrounded by retractive motion would be defined as occurring in the back of the cell.

Next, we measured the displacement along the boundary between successive protrusions at the front and successive retractions at the back. To explore the history dependence of these displacements, we plotted the displacement between successive protrusions against the displacement between the next set of successive protrusions. We made a similar scatter-plot for retractions. While such scatter-plots can be used to distinguish regions of low point density from regions of high point density, in regions in which plotted points overlap, they cannot be used to distinguish among high-density regions. Since the scatter-plots for protrusions and retractions have both low and high-density regions, we blurred the scatter-plots in order to compare them. First, the scatter-plots were pixelated by rounding each point to the nearest boundary point displacements. An image filter was next applied to the pixelated scatter-plots. (The filter was a Gaussian of size 200 by 200 boundary points and standard deviation 20 boundary points.)

Figures 2.4D and E show the blurred scatter-plots. The plot for successive protrusions is asymmetric, appearing as a thick, negatively sloped line that is brightest at the origin. This asymmetry indicates that protrusions zig-zag. In other words, if a protrusion occurs to the right of the previous protrusion, the next protrusion is most likely to occur to the left of the current protrusion. The plot for successive retractions appears as a strong peak centered at the origin with faint vertical, horizontal, and negatively sloped lines. The strong central peak indicates that a retraction is most likely to occur in the same location as the previous retraction. The faint vertical and horizontal lines indicate occasional, highly offset retractions, while the faint,

negatively sloped line indicates slight zig-zagging. While retractions remain at the same location, protrusions zig-zag.

We might expect to find a regular temporal relationship between protrusions and retractions. For example, a protrusion in the front might be followed regularly by a retraction in the back. To search for such a correlation, we cross-correlated protrusions and retractions. We created a time series of protrusions by setting a vector to 1 in every frame there was a protrusion, and 0 in every frame there was not a protrusion. We similarly defined a time series of retractions. Cross-correlating the two vectors we found zero correlation, to within error, between protrusions and retractions on time scales of less than a few minutes. We further blurred the two vectors by setting the frames before and after 1s to 0.5, and again cross-correlated the vectors. These blurred vectors also showed zero cross-correlation.

2.3.5. The shapes of protrusions and retractions are different

Playing a video of *D. discoideum* migration both backwards and forwards shows that time-reversed *D. discoideum* migration does not look like regular *D. discoideum* migration. On the whole, reversed protrusions do not resemble retractions, and reversed retractions do not resemble protrusions. But how are protrusions different from reversed retractions? One way to contrast the two is to compare the protrusive area (the area that the cell will occupy in the next frame but does not occupy in the current frame) to the retractive area (the area that the cell occupied in the previous frame, but does not occupy in the current frame). To reduce the effects of noise in this procedure, we calculated the protrusive and retractive areas

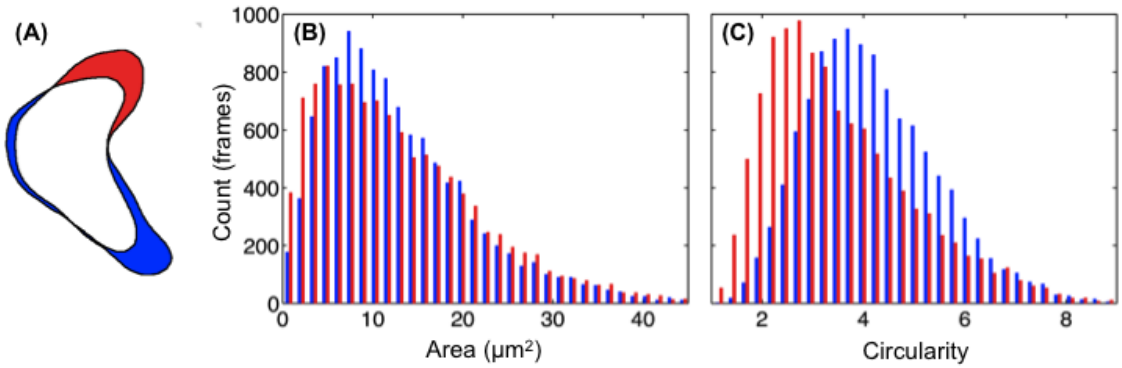

Figure 2.5. **Analyzing protrusive and retractive regions. (A) Here, a cell boundary and the cell boundary 12 seconds later are shown as black lines. The protrusive area, which is area that the cell occupied in the later frame, but not in the earlier frame, is shown as red. The retractive area, which is the area that the cell occupied in the earlier frame, but not in the later frame, is shown as blue. We analyzed the protrusive and retractive areas of 26 cells. (B) The distribution of protrusive areas, shown as red, and retractive areas, shown as blue. (C) The distribution of protrusive and retractive Heywood circularities. Again, shown as red and blue respectively. The Heywood circularity factor is defined as the ratio of a shape's perimeter to the perimeter of a circle that has the same area.**

over three frames (12 seconds). Figure 2.5A shows an example of the protrusive areas, shown in red, and the retractive areas, shown in blue. On average, there are 2.4 ± 1.2, (where 1.2 is the standard deviation) protrusive regions and 2.4 ± 1.2 retractive regions present in each frame.

We measured the distribution of protrusive and retractive areas in 26 cells (shown in Figure 2.5B). The distributions are similar, although slightly more frames have low or high protrusive areas than have low or high retractive areas. Similarly, more frames have an intermediate retractive area than have an intermediate protrusive area.

The difference is particularly pronounced in the smallest area range, over which more than twice the number of frames have protrusive areas than have retractive areas.

The size distributions of the protrusive and retractive areas appear similar, so we next consider the shape distribution of the areas. For each shape, we found the Heywood circularity factor, which is defined as the ratio of a shape's perimeter to the perimeter of a circle with the same area as that shape (88). For frames with more than one protrusive or retractive area, we sum the perimeters and areas before calculating the circularity. Figure 2.5C shows the shape distributions of protrusive and retractive areas. As expected, protrusive areas have a smaller average circularity than do retractive areas. In other words, while protrusive movement is concentrated and fast, retractive movement is spread out and slow.

2.3.6. Cell non-circularity increases with cell speed

When *D. discoideum* cells are first placed on a surface, they are stationary and round, but when they begin to migrate, they polarize, or elongate. Since cells do not start moving until they polarize, an increase in velocity is correlated with this initial polarization. For cells that have already polarized, though, do faster cells show increased elongation?

To address this question, we measured the Heywood circularity and the cell speed for each cell in every frame. The speed was calculated from the magnitude of the displacement of the boundary centroid over three frames (12 seconds), and then the frames were binned by centroid speed. Figure 2.6A shows the average circularity in each bin. The dashed line is a linear fit to the data. Even at higher speeds,

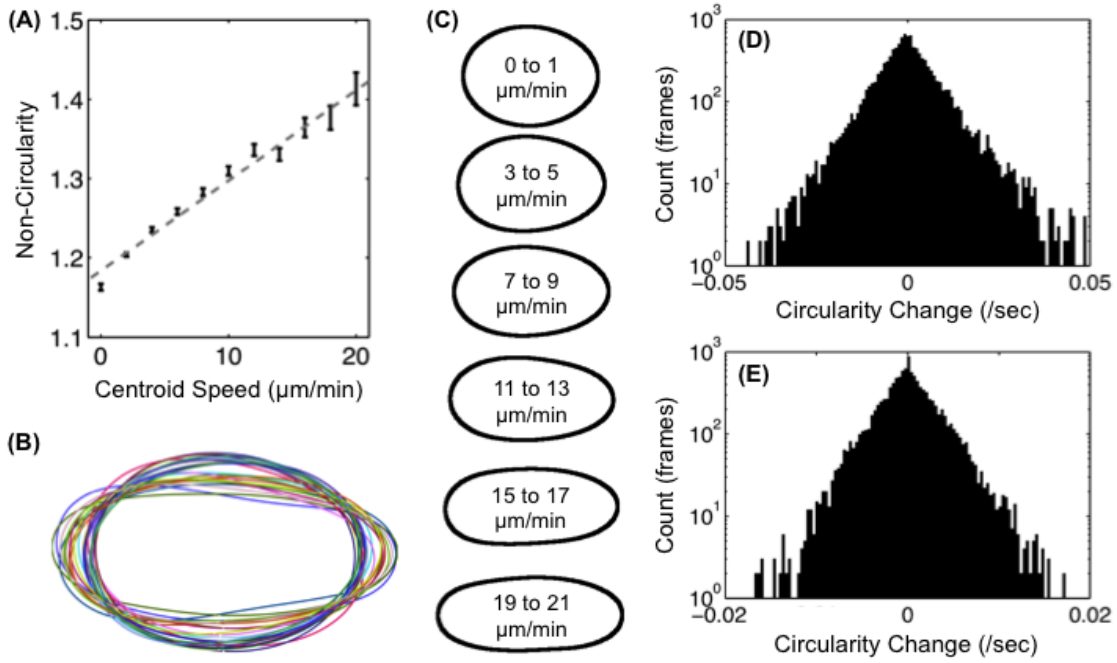

Figure 2.6. **Cell polarization increases with increasing centroid speed. (A) Cells were binned by centroid speed on a frame by frame basis, and then the average circularity of each bin was calculated. (The error bars represent the standard error of the mean). The dashed line, which is a linear fit to the data, indicates that circularity increases with increasing centroid speed. (B) The average shapes of each of twenty-six self-aggregating, wildtype cells. Each shape was normalized by the average distance from the boundary points to the boundary centroid. Some cells have rounder average shapes than others. This phenomenon is in part because movie lengths defer and cells take varied amounts of time to polarize after placement on the surface. (C) Cell boundaries were binned by centroid speed. Here, the average shape of every other bin is shown. (D) The distribution of change in circularity over four seconds and (E) thirty-two seconds. Both log-linear plots appear tent-like, although the x-axis magnitudes differ.**

circularity increases with increasing centroid speed, which suggests that among already polarized cells, faster cells are more non-circular. The Heywood circularity

factor measures not only how elongated a shape is, but also how curvy it is. For example, a circle with many small blebs would have a high circularity, even if it were not elongated. The number of curvature bumps could then affect a cell's circularity.

To visualize how cell shape varies with increasing centroid speed, we plotted the average cell shape in each binned range of speeds. In each frame, we first rotated the cell so that its back was at 0°. We also rotated the boundary point labels so that its back was labeled boundary point 0. The back of the cell was found by smoothing the local motion measure (over nine boundary points and nine frames), setting all positive, or protrusive, values to zero, and defining the cell back as the average of the remaining negative, or retractive, values. Since cell size varies, shapes were next normalized by the average radius of each cell. We then determined the average cell shape of a set of shapes by finding the average location of each same labeled boundary point. Figure 2.6B *s*hows the average shape of each cell analyzed. The cell shapes vary, at least in part, because cells polarize at different times in their image sequences. Figure 2.6C shows the average shape of each binned range of centroid speeds. As expected, as centroid speed increases, the cells become more elongated.

To explore how the circularity varies in time, we plotted the distribution of the change in circularity over 4 seconds and over 32 seconds (see Figures 2.6D and E). On log-linear scales both distributions appear tent-like. The chance of a jump or fall in circularity thus decreases exponentially with the size of the event. While the distributions appear symmetric about zero change in circularity, there may be slightly more large positive changes in circularity than large negative changes.

2.4. Discussion

In summary, we have introduced a simple, yet flexible, method that allows for the study of many aspects of migrating cell shape. Using the migration of the amoeboid *D. discoideum* as an example, we demonstrated the utility of measuring both the overall, global shape dynamics, and the local, protrusion and retraction dynamics of migrating cells.

There are many local and global measures of shape. How should we decide which measures to use? In answering that question, we consider that each measure imposes a certain perspective on the further analysis of shape dynamics. That perspective effectively biases our plots, and affects further analysis of shape dynamics.

Ideally, we would like to begin by choosing a neutral perspective. For local measures, such a neutral perspective exists. The mathematics of curves tells us that a neutral perspective is provided by the Frenet frame, which is defined at each point along a curve as the direction of the tangent to the curve and the direction of the normal to the tangent. The Frenet-Serret equations describe how the Frenet frame evolves with arc length. In 2-D, the only variable in the Frenet-Serret equations is curvature (87). Curvature, parameterized by arc length, thus provides a complete, neutral perspective for the analysis of shape dynamics. The boundary curvature, a local shape measure (see Figure 2.1E), exhibits curvature waves, i.e. regions of high local curvature that originate near the leading edge of the cell and travel toward the back of the cell. Like local protrusions, these waves occur on roughly alternating sides of the cell.

Curvature provides a complete, neutral description of shape because it is based on the perspective of the curve itself. In mathematics, the only neutral, and hence special, perspective is that imposed locally by the curve. In biology, however, there are additional special perspectives because the cell machinery that interacts with and determines cell shape itself provides useful reference points. The biologically imposed perspective on which we focus is the distance from the center of the cell to each boundary point, which provides a global perspective that highlights global processes such as cortex contractions. Indeed, the distance from the center of the cell to each boundary point (see Figure 2.1D), exhibits oscillatory dynamics. These oscillations are likely related to the quasiperiodic contractions of the entire cell driven by the actomyosin cortex that are seen as, e.g., oscillations in strain energy (89).

Each metric can provide insights into a distinct biological phenomenon: oscillations of the shape metric indicate global contraction cycles, and the local protrusion metric is a good indicator of actin polymerization waves at the leading edge. Note that the metrics are complementary: in the global metric, localized waves are barely visible, and in the local metric the overall shape oscillation is mostly masked. Indeed, the need for multiple metrics may be a reflection of the fact that the actin cytoskeleton has several components, among them the dynamic leading edge, which generates local protrusions and is best captured via local metrics, and the actomyosin cortex, which yields contractions of the whole cell and is best captured via global metrics (90). Additional perspectives that should be explored include the distance from the microtubule organizing center, or the distance from the center of the nucleus.

Additional metrics and insights can be gained by connecting local and global shape metrics to the motion of the cell. We find that the speed of the cell is correlated with another simple measure of global shape, the Heywood circularity, as shown in Figure 2.6. In other words, faster cells are more non-circular. The local protrusive and retractive motion of the cell boundary can be analyzed as individual protrusions and retractions, which are defined by averaging and thresholding local shape changes in time and space. Individual protrusions, as shown in Figure 2.4, exhibit characteristic zig-zag dynamics that yield the directional persistence of cell migration, which is consistent with prior observations (68, 69). Analysis reveals that the protrusive motion is generally not localized but that regions of peak protrusive activity travel along the leading edge of the cell with wave-like dynamics. This phenomenon is seen in Figure 2.4, and is analyzed in depth in Chapter 3.

We have used different metrics that give complementary information. The complementary nature of the different metrics is based on the distinct perspectives through which shape is parameterized – including the neutral perspective of curvature – and is likely a reflection of the diversity of biological contributions to cell migration. Our method allows for the simple integration of multiple perspectives and the addition of new measures for both local and global aspects of cell shape.

2.5. Materials and methods

2.5.1. Cell culture and imaging

Wildtype (AX3) *D. discoideum* cells were prepared as described previously (91). Cells were developed for either 3.5, 5 or 6.5 hours and then cytoplasmically

dyed with CellTracker Green CDMFA (Invitrogen) (91). Fluorescence images were taken on a Leica TCS SP2 confocal microscope with a 40× objective every 4 seconds.

2.5.2. Image sequence pre-processing

Individual cells were selected for analysis, and their image sequences were pre-processed using ImageJ (NIH). Any feature that might make automatic extraction of the contour via snake algorithms difficult, such as a nearby cell, or materials shed by the cell, was painted the background color. Image contrast and brightness were then enhanced until the cell interior was white, the cell exterior black, and the cell edge varying shades of gray. Each sequence was then despeckled to remove noise, and the gradient was subsequently taken.

2.5.3. Snake algorithm parameters

Cell boundaries were extracted using a snake algorithm. We modified sample code from (86) to process entire image sequences. While the boundary in the first frame was initialized manually, subsequent frames were initialized with the extracted boundary from the previous frame. The extracted boundary in each frame was also interpolated to output 400 boundary points. Note that while, within each frame, pairs of adjacent boundary points are equidistant, since there are a constant number of boundary points per frame, pairs of adjacent boundary points are not equidistant across frames. Boundary point labels were, if necessary, flipped so that boundary point indices increased counter-clockwise. When snaking, we used an unnormalized gradient vector field. We also set the tension (alpha) to 0.0002, the rigidity (beta) to 0.001, the step size (gamma) to 1, and the external force (kappa) to 0.6.

2.5.4. Tracking and motion mappings

The snake algorithm outputs cell shapes as a list of boundary points. Note that while within each frame neighboring points are equidistant along the perimeter, the distance between neighboring points varies across frames as the length of the cell perimeter changes. Tracking the local boundary requires mapping the boundary points in each frame to the boundary points in the next frame. This procedure will be called the "Tracking Mapping". For ease of visualization and quantification, we would like to have a constant number of boundary points per frame, and we would like to track all of the boundary points from frame to frame. We therefore need to define a 1:1 tracking mapping. Mappings with crossing mapping vectors can be excluded, since these crossings are topological violations (21). (For instance, mapping point 1 in frame A to point 2 in frame B and point 2 in frame A to point 1 in frame B is a topological violation.) Thus, the only possible remaining 1:1 mappings are rotations of one another. Among those, we chose the mapping that introduces the least rotation by minimizing the sum of the square distances between mapped points. An example of a tracking mapping is shown in Video 10 of (24).

The magnitude of the tracking mapping is a measure of global boundary point motion. However, this measure is not well suited to protrusive motion, since a single protrusion results in the measured movement of every boundary point. Instead, we would like a measure that finds motion in only the boundary points that comprise the protrusion. We then need a local measure that is not based on a 1:1 mapping and that does not induce topological violations. One such measure is the distance from each boundary point to the boundary in a later frame. We mapped points in one frame

(source points) to the boundary in a frame obtained 12 seconds later (target points), rather than to the one in the next frame, to reduce noise and to allow consistency across differing frame rates. Mapping each source boundary point to the closest target point in a later frame does not map boundary points into protrusions (Figure 2.7A) and can lead to large gaps or clusters in the mapped-to point sequence. Therefore, we smoothed over the list of target points. In other words, in each frame the mapping can be represented by a list in which the *i*th value is the index of the boundary point to which boundary point *i* maps. These lists were twice smoothed over using an averaging window (Figure 2.7B). Notice that this method of smoothing does not induce topological violations. (The first smoothing had a window size of 19 boundary points, while the second had a size of 15 boundary points.) The magnitude of the local motion measure was then defined as the distance between a source point and the corresponding target boundary point in the smoothed list. If the target boundary point is outside of the current boundary, the local motion measure was defined to be positive; otherwise it was defined to be negative. The color scale for local motion was cut off at a maximum magnitude for visualization. Also, boundary point labels were rotated, such that for each cell the greatest protrusive motion occurs at boundary point 300.

2.5.5. Measuring boundary curvature

At each boundary point, we calculated the boundary curvature by fitting a circle to that boundary point and the two points that are 10 boundary points away from it. The magnitude of the boundary curvature was then defined as the reciprocal

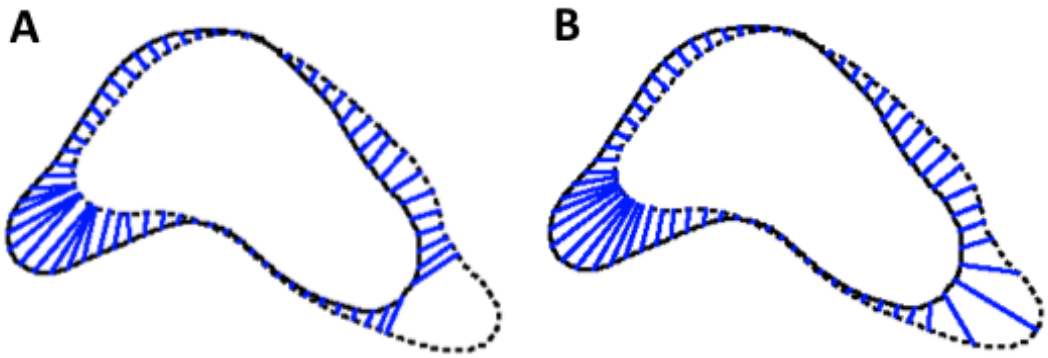

Figure 2.7. The local motion mapping. (A) First, each boundary point in a frame is mapped to the closest boundary point in the frame 12 seconds later. A representative frame's boundary is shown as a solid line, the boundary in the frame 12 seconds later by a dashed line, and the mapping between boundary points by blue lines. (B) Next, we smooth over target boundary points, pulling mapping vectors into protrusions, and more evenly distributing vectors in retractions. The magnitude of these blue mapping vectors is then defined as the magnitude of our local motion measure.

of the radius of that circle. If the midpoint of the two points 10 boundary points away was inside the cell, the curvature was defined as positive, otherwise it was defined as negative. For visualization, the curvature was smoothed over 3 boundary points and 3 frames, and the color scale was cut off at a maximum curvature magnitude.

2.5.6. Analyzing protrusive and retractive motion as discrete events

To analyze protrusive and retractive motion as discrete events, we calculated the location and the time of individual protrusions and retractions. First, we smoothed the local motion measure with an averaging window of 3 frames and 3 boundary points. Next, in order to find protrusions, negative elements of the smoothed measure were set to zero. Elements with a value less than a noise threshold

(1 pixel moved/12 seconds) were also set to zero. An individual protrusion was then defined as a peak in this processed local motion measure. Individual retractions were defined similarly.

Chapter 3. Cell shape dynamics: From waves to migration

This chapter is adapted from Driscoll, McCann, Kopace, Homan, Fourkas, Parent, and Losert (24). The text and figures are reproduced here under the CC BY License. Meghan Driscoll fabricated the cliffs, performed the fluorescence microscopy experiments, and analyzed the data. Colin McCann, along with Meghan Driscoll, mentored two undergraduates, Rael Kopace, who imaged cells on cliffs, and Tess Homan, who did preliminary shape analysis. Colin McCann performed the reflection microscopy experiments.

3.1. Overview

We observe and quantify wave-like characteristics of amoeboid migration. Using the amoeba *Dictyostelium discoideum*, a model system for the study of chemotaxis, we demonstrate that cell shape changes in a wave-like manner. Cells have regions of high boundary curvature that propagate from the leading edge toward the back, usually along alternating sides of the cell. Curvature waves are easily seen in cells that do not adhere to a surface, such as cells that are electrostatically repelled from surfaces or cells that extend over the edge of micro-fabricated cliffs. Without surface contact, curvature waves travel from the leading edge to the back of a cell at ~35 mm/min. Non-adherent, myosin II null cells do not exhibit these curvature waves. At the leading edge of adherent cells, curvature waves are associated with protrusive activity. Like regions of high curvature, protrusive activity travels along

the boundary in a wave-like manner. Upon contact with a surface, the protrusions stop moving relative to the surface, and the boundary shape thus reflects the history of protrusive motion. The wave-like character of protrusions provides a plausible mechanism for the zig-zagging of pseudopods and for the ability of cells both to swim in viscous fluids and to navigate complex three-dimensional topography.

3.2. Background

In this chapter, we analyze the shape dynamics of suspended amoebae whose fronts are not in contact with a surface. We also further analyze the shape dynamics of cells migrating on flat surfaces, including how cellular shape is related to the cellular footprint, which is the region over which cells contact the surface.

During chemotaxis, a chemical gradient directs cell migration. Chemotaxis occurs in phenomena as diverse as wound healing (2) and embryonic development (3), and has also been implicated in a wide array of pathological processes including aberrant angiogenesis (4) and cancer metastasis (5). Chemotaxing cells can migrate individually during immune responses and neuronal patterning, or in cooperative groups during embryogenesis, wound healing, and organ and vasculature formation.

The social amoeba *Dictyostelium discoideum* is a model system for directed cell migration, and has been used to elucidate the regulatory processes of chemotaxis. *D. discoideum* chemotaxis is of comparable speed to neutrophil chemotaxis and involves similar regulatory processes (50). The chemotaxis of *D. discoideum* is also more than an order of magnitude faster than typical epithelial cell migration and does not involve mature focal adhesion complexes (92). *D. discoideum* cells migrate directionally in gradients of cyclic adenosine monophosphate (cAMP). The binding

of cAMP to specific cell surface receptors leads to the activation of various effectors, including adenylyl cyclase, resulting in the production and secretion of additional cAMP and the relay of the signal to neighboring cells (93). This signal relay guides the cells to migrate collectively in a head-to-tail fashion toward aggregation centers and to maintain a preferred migration direction over distances much larger than the characteristic diffusion lengths of molecules (91). Cells with the *aca*$^{-}$ mutation do not produce cAMP and, in its absence, are mostly round and immotile (55). However, when stimulated with exogenous cAMP, *aca*$^{-}$ cells polarize and begin to migrate. If stimulated with a uniform concentration of cAMP, *aca*$^{-}$ cells exhibit chemokinesis (chemically induced random migration). In response to a cAMP gradient, these cells chemotax effectively (55).

The regulatory processes behind *D. discoideum* chemotaxis have been investigated in great depth. Recent discoveries demonstrate the complexity of key chemotactic signaling pathways, including multiple compensatory mechanisms for sensing the direction of cAMP gradients (94). Models of cell movement often consider migration as the final step in this process and use the output of the directional sensing machinery to assign a probability of forming a protrusion (and subsequently migrating) in a particular direction (95). In most models, the location at which a new protrusion forms determines the direction of the protrusion and ultimately the direction of migration of the cell. For example, Haastert and Bosgraaf found that pseudopods grow in a direction perpendicular to the local boundary (96). Directional migration in response to chemotactic signals is considered to be due to

either the formation of new protrusions (the compass model) or the biased bifurcation of existing protrusions (the bifurcation and bias model) (85).

Quantitative studies of cell shape and motion that follow protrusions are now emerging, and indicate that protrusion dynamics are richer than anticipated (21, 71, 96-99). Machacek and Danuser, tracking a fixed region of the boundary of slow epithelial cells with sub-pixel resolution, found three distinct states of local protrusion activity: local protrusions that grow and retract in a single location along the cell edge, waves that travel along the edge of the cell, and fast, large-scale protrusions (21). Dobereiner *et al.* found that wave-like protrusion dynamics are common to a wide range of slow-moving cells (28), especially during cell spreading.

How are such complex protrusion dynamics relevant to chemotaxis and directed cell migration? For the models of chemotaxis reviewed above, and for fast migration, a local protrusion phenotype is usually assumed in which protrusions are a (noisy) output in response to a chemotactic signal. This view appears to be supported by experiments in which a strong chemotactic signal is placed in close proximity to individual cells, causing a pseudopod to form in the direction of the signal (93).

However, recent experiments and modeling efforts point to a more complex protrusive machinery. Indeed, given signal strengths at physiological levels (and even in the absence of chemotactic gradients), protrusions tend to form on alternating sides of the leading edge of the cell, resulting in a zig-zag migration pattern (69). Such zig-zag motion indicates that protrusion locations are not just described by a noisy output based on a chemical signal, but are also influenced by the prior

protrusion history. The alternating position of pseudopods can be explained, for example, by considering the protrusive machinery as an excitable system (100).

The conclusion that alternating pseudopods are prominent in fast migrating cells relies on thresholds to separate individual pseudopods in a consistent way. However, it is unclear whether the underlying biology of protrusions justifies such thresholding. Instead, zig-zagging and alternating pseudopods may be the result of wave-like behavior of the protrusive machinery. In developing tissues, actin waves can be seen to propagate across groups of cells (101). There is also direct evidence that wave-like intracellular actin polymerization processes are prominent in fast migrating cells. Some of the first indications of this effect were from Vicker and colleagues, who found that *D. discoideum* pseudopod dynamics are not random (17), but rather are associated with actin filament polymerization waves (102) that can drive locomotion (103). Others were able to observe wave-like dynamics directly in actin polymerization and depolymerization (19). The connection between internal waves and forces has also been elucidated (27). Finally, the interaction between waves and surfaces is key to understanding migration. For example, Weiner *et al.* found that when a neutrophil runs into another cell or an obstacle, actin waves are extinguished at the interaction site, allowing cells to change direction and avoid the obstacle (20). This observation indicates that waves may not be observed when cells are confined between boundaries, such as, e.g., in a key paper that reported zig-zagging of *D. discoideum* protrusions (68).

To study the character of protrusions during fast cell migration and chemotaxis, we present new methods for the quantification of the dynamic shape of

migrating cells. Using these methods, we demonstrate that protrusions in *D. discoideum* have a wave-like character. As found in neutrophils, the waves appear to stop moving when touching the surface, so the wave-like character of protrusions is most evident when cells do not touch the surface, or when they extend over the edge of a cliff. While our study highlights that wave-like dynamics exist under many different conditions, we do not directly measure motion of the actin cytoskeleton or membrane, and thus have no conclusive evidence that the wave-like dynamics reflect reaction-diffusion waves (due to actin polymerization or myosin contraction dynamics) or transport of membrane or intracellular material. These results could lead to a model that relates protrusive waves to the zig-zag-like appearance of cell tracks and the directional persistence of cell motion during chemotaxis.

3.3. Results

3.3.1. Peaks in boundary curvature move from the front to the back of cells

We analyzed the shapes of starved, wild-type *D. discoideum* that were self-aggregating. The extracted shape of one such migrating cell is shown in Figure 3.1A. The boundary color represents boundary curvature. As expected, the front and back of the cell have high curvature. Additional peaks in boundary curvature indicate other local protrusions. We find that additional protrusions first become visible near the front of the cell and, with respect to the cell, propagate towards the back as the cell migrates. At the sides of cells, these curvature bumps appear stationary relative to the surface (see Figure 3.1B for a representative image sequence).

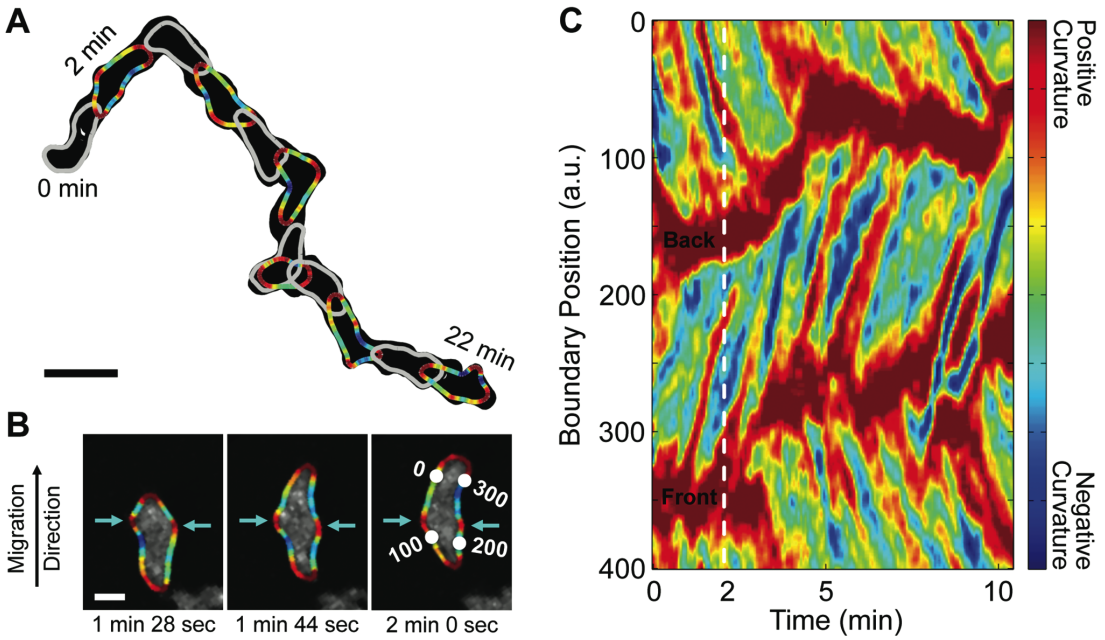

Figure 3.1. **The boundary curvature of a self-aggregating wild-type *D. discoideum* cell. (A) The overlapped light gray boundaries show the shape every 4 seconds, while the alternating dark gray and colored boundaries show the shape every 2 minutes. Colored boundaries represent curvature. (Scale bar, 20 µm.) (B) The boundary curvature overlaid on the original fluorescence images (Video 1 of (24)). Two curvature peaks, indicated by teal arrows, remain at the same location as the cell migrates through them. Numbers label the indices of every 100th boundary point (Video 2 of (24)). (Scale bar, 5 µm.) (C) The spatial and temporal evolution of boundary curvature can be visualized in a kymograph. Peaks in boundary curvature propagate from the cell front (initially near boundary point 150) to the cell back (initially near boundary point 350).**

Figure 3.1C shows a kymograph of boundary curvature (see Chapter 2). The front and back of the cell each appear as thick stripes of high curvature and the additional, lateral peaks appear as thin lines that connect the front to the back. Since the thin lines representing the curvature peaks are approximately parallel, the

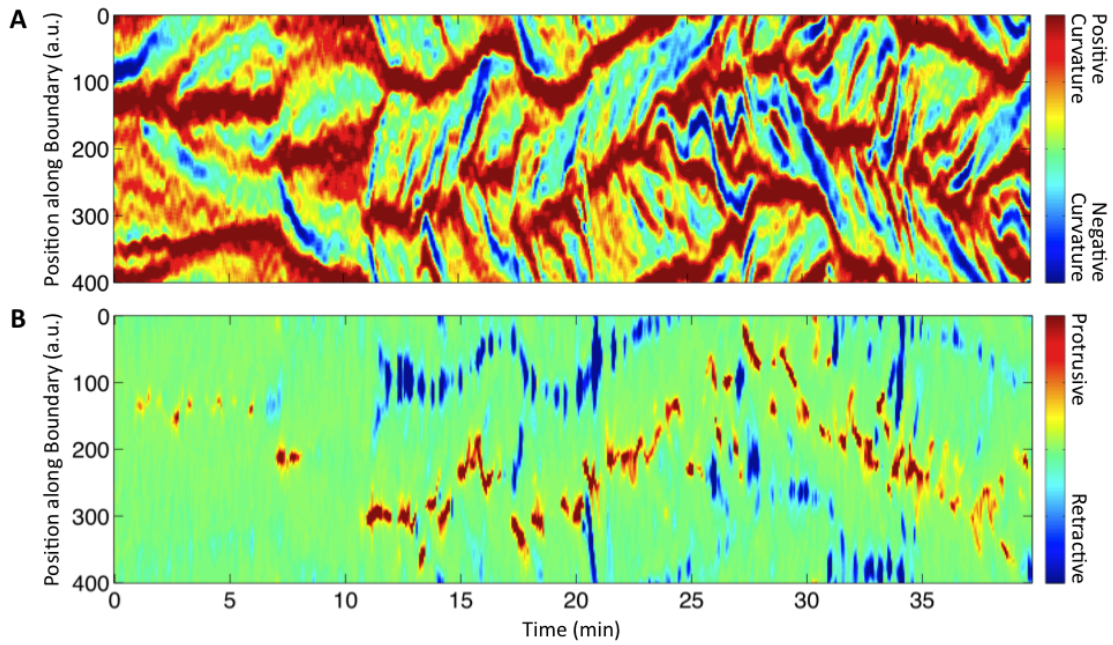

Figure 3.2. **The (A) boundary curvature and (B) local motion kymographs of a self-aggregating, wild-type cell (see Video 3 of (24)).**

curvature peaks travel at equal speed with respect to the cell. The boundary curvature kymograph of an additional, developed, wild-type cell is shown in Figure 3.2A (Video 3 of (24)). Averaging across 26 cells (the same set of cells analyzed in Chapter 2), we find that the peaks move relative to the cell at 10.9 ± 0.7 μm/min, comparable to the average migration speed of *D. discoideum* cells. This finding is consistent with the observation that peaks of high curvature on the side of the cell are stationary with respect to the surface.

Figure 3.1C shows that most high curvature regions on the side of cells start at the leading edge, and thus that the shape of the cell reflects a history of activity at the leading edge. Indeed we find a connection between curvature and protrusions at the leading edge, as described below. The amplitude of each peak varies as it travels

from front to back, but tends to diminish with time, a further indication that the associated local protrusions are passive or shrinking.

3.3.2. At cell sides, cell-surface contact is enhanced near curvature peaks

Migration requires not only pseudopods but also adhesion to a surface. Thus, surface contact can indicate whether bumps on the side of the cell reflect pseudopods that have successfully adhered (and thus can contribute to motion) or unsuccessful pseudopods that failed to adhere. We imaged fluorescently-labeled, developed, wild-type cells, while simultaneously using internal reflection microscopy (IRM) to image the region of cell-surface contact. We extracted both the boundary of the entire cell and the boundary of the surface contact region(s) from the images. Figure 3.3A shows, for a representative cell, an IRM image sequence overlaid with the boundary of the surface contact region and the boundary of the entire cell. In this image sequence, the cell extends a protrusion that is not in contact with the surface, the protrusion makes contact with the surface, and then the area of surface contact under the protrusion grows. Our data reveal that the local protrusions at the side of the cell correspond to regions of enhanced cell-surface contact, and thus likely reflect successful pseudopods. We note that some protrusions retract quickly and never contact the surface. For example, in the movie associated with this image sequence (see Video 4 of (24)), 4 out of 14 large protrusions retract before they contact the surface. Protrusions that do contact the surface are rarely retracted, indicating that contact stabilizes the protrusions.

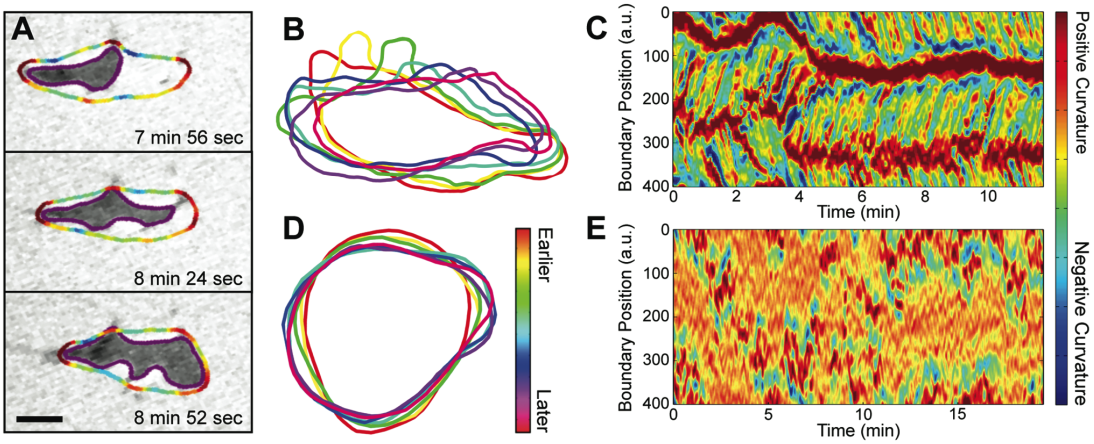

Figure 3.3. **The interaction of boundary curvature waves with the substrate. (A) An IRM image sequence overlaid with the boundary of the surface contact region, shown in purple, and the boundary of the entire cell, shown colored by curvature (see Video 4 of (24)). At the sides of cells, peaks in cell boundary curvature are located near peaks in surface contact region boundary curvature. Both of these curvature peaks are stationary with respect to the substrate. (Scale bar, 5 µm.) (B) The overlaid shapes, imaged 4 seconds apart, of an *aca*- (non cAMP releasing) cell that is electrostatically repulsed from the substrate, and so is not adhered to the surface. The curvature peak that travels from the cell front to the cell back is moving with respect to the substrate. The centroid positions were aligned to account for drift. (C) The boundary curvature kymograph of this non-adherent cell (see Video 5 of (24)). (D) The overlaid shapes, imaged 4 seconds apart, of a non-adherent, myosin II null cell. While the cell extends regions of transient protrusive activity, it has no apparent curvature waves. (E) The boundary curvature kymograph of this non-adherent myosin II null cell.**

3.3.3. Non-adhered cells exhibit traveling curvature waves

At the sides of migrating cells, regions of high curvature are in contact with the surface and remain stationary. However, in analyzing the shapes of migrating

cells it is difficult to determine if regions of high curvature are stationary at the front of cells. To analyze the behavior of high curvature regions in the absence of surface contact, we analyzed the shape of *aca-* cells that were electostatically repelled from the surface. Since cell membranes and glass coverslips are both negatively charged, cells do not adhere to coverslips in a solution at a low salt concentration (104). The cells remain viable – upon addition of standard buffer the cells adhere to the surface and migrate. We found that for non-adherent cells, regions of high curvature actively move in a wave-like manner from the cell front to the cell back (Video 5 of (24), Figure 3.3B). Figure 3.3C shows the curvature kymograph of a non-adherent cell. Here, the curvature waves move at an average speed of 36 ± 2 μm/min (with a standard deviation of 8 μm/min), which is much faster than the average cell speed in the movie of 8 μm/min (with a standard deviation of 5 μm/min). In both adherent and non-adherent cells, the high curvature regions tend to alternate between the left and right sides of the cell.

3.3.4. Non-adhered myosin II null cells show shape oscillations

We also analyzed the shape of *myoII-* cells that were electostatically repelled from the surface (Figures 3.3D and E). Unlike *aca-* cells, *myoII-* cells do not exhibit traveling curvature waves. Instead, *myoII-* cells are round with localized, transient patches of protrusive activity. These protrusive patches are not confined to one region of the cell boundary, as they would be if there were a stable cell front, but rather can appear anywhere along the cell boundary.

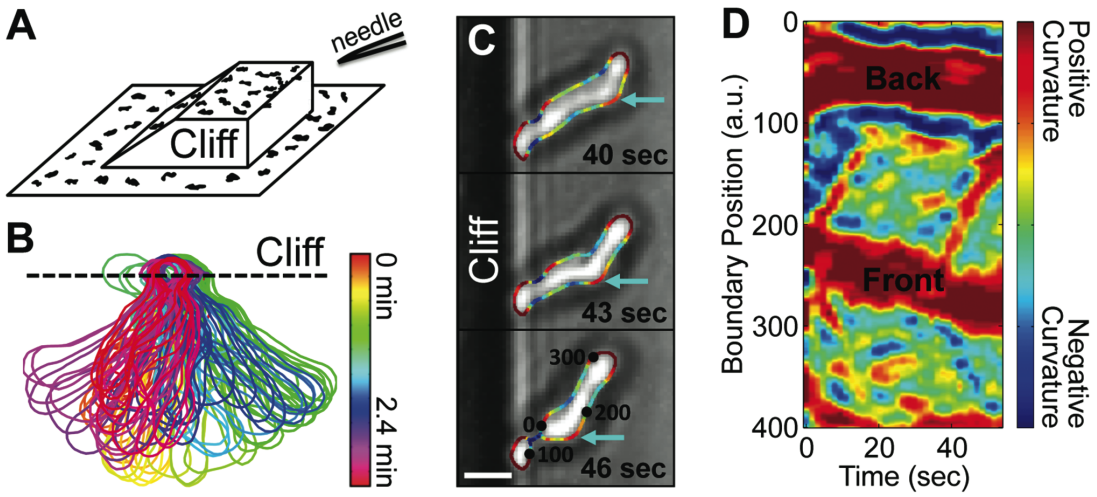

Figure 3.4. **Boundary curvature waves on cells that are extended over the edge of a cliff. (A) A schematic of the 3-D surface on which cells are guided over a cliff edge. The surface closest to a cAMP-releasing needle is the cliff edge. (B) The overlaid boundaries show a cell extended over the edge of a cliff and wiggling rapidly (boundaries are 1.6 seconds apart). (C) An image sequence of a propagating curvature wave. (See Video 5 of (24).) (Scale bar, 5 μm.) (D) The corresponding curvature kymograph, showing multiple curvature waves.**

3.3.5. Cells extended over a cliff also exhibit traveling curvature waves

Using surfaces with three-dimensional topography, we also analyzed the shapes of cells that adhere only at their back, even at standard salt concentrations. To guide a cell to move away from the surface, we placed a point source of cAMP above and over the edge of a microfabricated ramp that terminated with a 75 μm tall cliff, such that the surface closest to the point source was the cliff edge. A schematic of our set-up is shown in Figure 3.4A. The majority of cells that reach the edge of the cliff extend themselves over the cliff edge. Many of those cells also migrate along

the cliff edge to attempt to reach the needle. We never observed a cell falling off of a cliff. Instead, cells at the cliff edge extend up to 80% of their surface area over the edge toward the cAMP source. The shape dynamics at first glance look quite distinct – the cells swing back and forth quickly over the edge (Figure 3.4B). However, curvature waves are again seen in the portion of each cell that is not adhered to the cliff (which represents the majority of the cell). Figure 3.4C shows an image sequence of one such *aca*- cell, in which a curvature wave propagates from the front to the back of the cell (see Video 6 of (24)). (This cell also appears in Appendix A, although the boundary curvature is not analyzed.) Figure 3.4D shows the corresponding curvature kymograph. The average curvature wave speed for the cell shown here is 29 ± 3 μm/min (as calculated from 9 waves over 2.4 minutes). The average curvature wave speed of cells extended over the edge of a cliff is comparable to the curvature wave speed of cells that are electrostatically repelled from their substrate. The swinging of the cell appears correlated with curvature waves hitting the surface, which provides a simple mechanism for cellular reorientation, and hence the exploration of 3-D space.

3.3.6. Curvature peaks are seen only after cell polarization

To explore the onset of curvature peaks at the sides of cells, we analyzed the dynamic shape of polarizing *D. discoideum*. Cells are almost always round when initially placed on a surface, although wild-type cells quickly polarize and begin to migrate. *Aca*- cells, which do not produce cAMP, are more basal (quiescent) than are wild-type cells. However, wild-type and *aca*- cells migrate with comparable speed and directional persistence (91), and exhibit indistinguishable curvature peaks (Figure

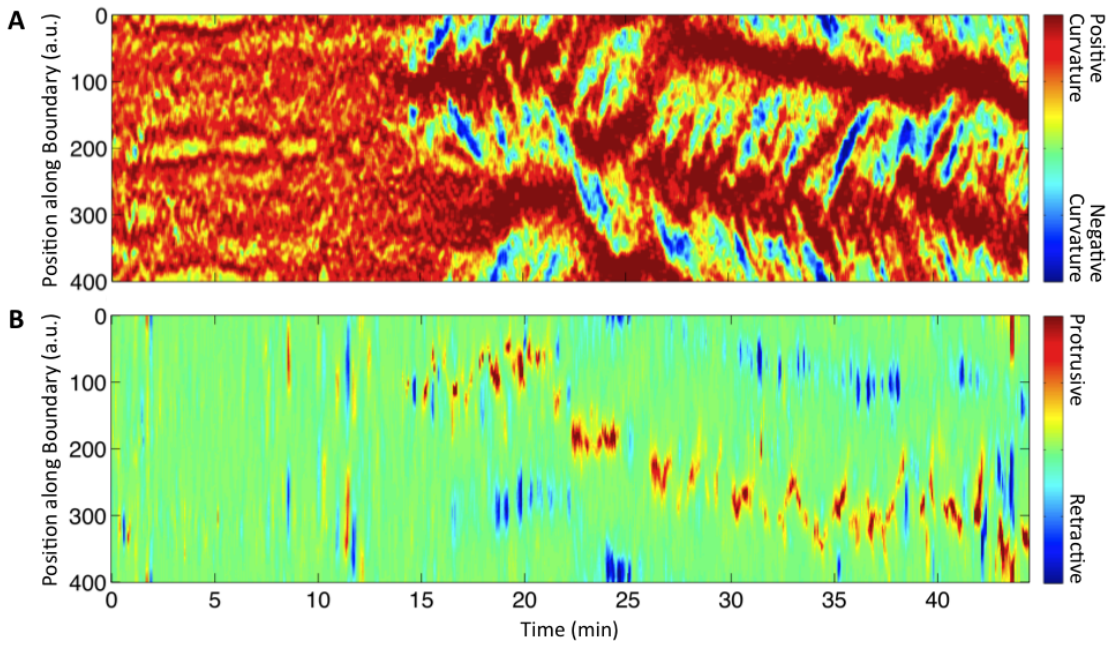

Figure 3.5. **The polarization of a fluorescently dyed *aca-* cell (see Video 8 of (24)). The (A) boundary curvature and (B) local motion kymographs are similar to those of wild-type cells.**

3.5A). We therefore analyzed the onset of curvature peaks in *aca-* cells. Even prior to polarization, cells send out small, quickly retracted protrusions. Since these transient protrusions are more visible in phase-contrast images than in images of fluorescently dyed cells, we also analyzed phase-contrast movies (Figure 3.6). The polarization of a fluorescently dyed *aca-* cell is shown in Figure 3.5A (see Video 8 of (24)).

When a cell polarizes, its shape elongates. To quantify the degree of polarization, we define the non-circularity as the ratio of the cell perimeter to its area, normalized so that the non-circularity of a circle is 1. The non-circularity, centroid velocity, and boundary curvature of a polarizing *aca*$^{-}$ cell are shown in Figure 3.6.

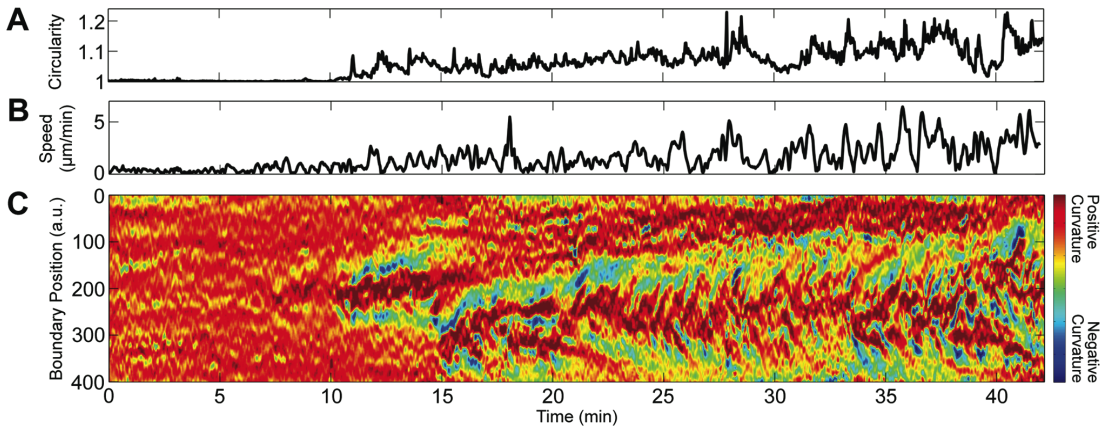

Figure 3.6. **Polarity symmetry-breaking of an *aca*⁻ (non cAMP releasing) cell. (A) During polarization, non-circularity, the normalized ratio of perimeter to the perimeter of a circle with the same area, increases in an oscillatory fashion. (B) The speed of the cell centroid. (C) Boundary curvature, which prior to polarization is mostly static, begins exhibiting organized curvature waves following polarization (see Video 7 of (24)).**

While the non-circularity is initially near one, it soon begins to increase in an oscillatory fashion. The boundary curvature, on the other hand, changes pattern abruptly at the onset of motion. While the curvature prior to polarization is slightly irregular, curvature peaks (tilted red lines in Figure 3.6C) appear only after polarization. Hence, polarization and migration coincide with a change in the nature of protrusions from being localized and intermittent to being more continuous and possibly wave-like.

3.3.7. Curvature peaks are associated with boundary motion

Curvature peaks are suggestive of protrusions, because a localized protrusion is necessarily associated with a localized region of high curvature. To compare

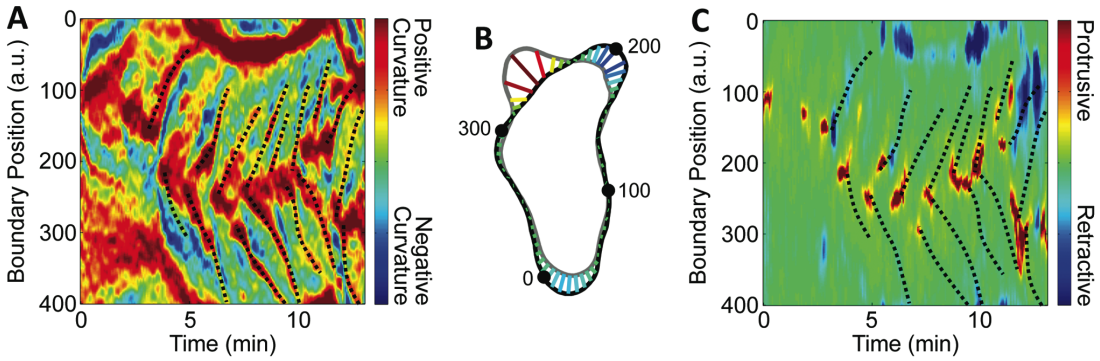

Figure 3.7. **The initialization of curvature waves is associated with protrusive motion. (A) The boundary curvature kymograph of the cell shown in Figure 3.2A. Curvature waves, shown as dashed black lines, are drawn on. (B) One measure of local boundary speed is the magnitude of the motion mapping. Here, the cell shape at 6 minutes is shown as the black boundary, while the shape 12 seconds later is the gray boundary. The motion mapping vectors, shown here colored by magnitude (colormap as in *c*), connect the boundary points in the earlier frame to boundary points in the later frame. Only every eighth mapping vector is shown. (C) The local motion kymograph with the overlaid position of the curvature waves, which appear as dashed black lines. Protrusive events usually coincide with the initialization of curvature waves.**

boundary curvature to motion, we developed a measure of local boundary motion. We calculated the motion of each boundary point by measuring the distance to the closest boundary point in a later frame and then smoothing over the list of mapped to boundary points. Protrusive motion was defined to be positive, while retractive motion was defined to be negative. Figure 3.7B shows representative local motion mapping vectors colored by the value of the local motion measure, while Figure 3.7C shows the local boundary motion kymograph of the same developed, wild-type cell shown in Figure 3.3A, (see Figures 3.2B and 3.5B for additional plots of wild-type

and *aca*$^-$ cells.) From local motion kymographs, we see that cells have two regions of activity, one associated with protrusions and one with retractions. Neither the fronts nor the backs of cells move at constant speed; rather, they start and stop intermittently. However, while the location along the boundary of retractions shifts little from retraction to retraction, protrusions tend to zig-zag.

We can compare boundary curvature to boundary motion by comparing the curvature and local motion kymographs. Curvature peaks (shown as dashed black lines) are overlaid on Figures 3.7A and 3.7C. In general, we find that the initiation of curvature peaks tends to coincide with the growth of protrusions, at the front of the cell. (Also, Figure 3.8 shows how these curvature peaks relate to the distance from the cellular boundary to the footprint.) Thus protrusive motion might travel along the boundary in the same manner as the curvature peaks.

3.3.8. Protrusive motion travels ballistically along the cell boundary

Protrusive motion has often been discretized into pseudopod extension and retraction events. Here we analyze protrusive motion both with and without discretization and show that discretization may hide the wave-like nature of the protrusive process. We first analyze boundary motion under the assumption that protrusions and retractions are discrete events. The times and locations of individual protrusions and retractions along the boundary were defined as the peaks and valleys of the local motion measure, respectively. Figure 3.9B shows the protrusions and retractions extracted from the local motion data shown in Figure 3.9A. Protrusions are shown as black dots, while retractions are shown as white dots. As expected

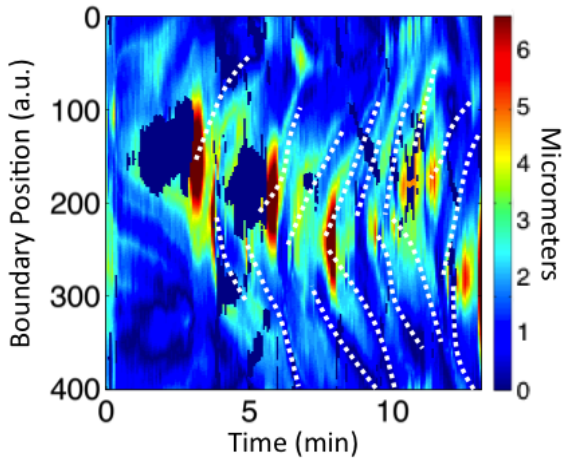

Figure 3.8. **Curvature waves are visible in the cellular footprint (see Video 4 of (24)). The distance between the cell boundary and the cell footprint overlaid by the cell's curvature waves, shown as white dashed lines. This is the same cell shown in Figures 3.3A and 3.7.**

based on the visualization in Figure 3.9A, protrusions are more spread out at the front of the cell than are retractions at the back. However, some retractions do occur at the front of the cell when protrusions are retracted. We calculated temporal and spatial statistics based on data from 26 self-aggregating wild-type cells, including those with developmental times 1.5 hours longer or shorter than our normally used time. We found a total of 2219 protrusions and 2220 retractions in these data. On average, wild-type cells exhibit 2.9 ± 0.2 protrusions/minute and 2.9 ± 0.2 retractions/minute. Boosgraaf *et al.* found a similar frequency of 4 protrusions/minute (69).

While analyzing protrusions as discrete events yields results consistent with prior work (69), two facets of the kymograph of local protrusions and retractions in Figure 3.9A indicate that this discretization can mask continuous or wave-like

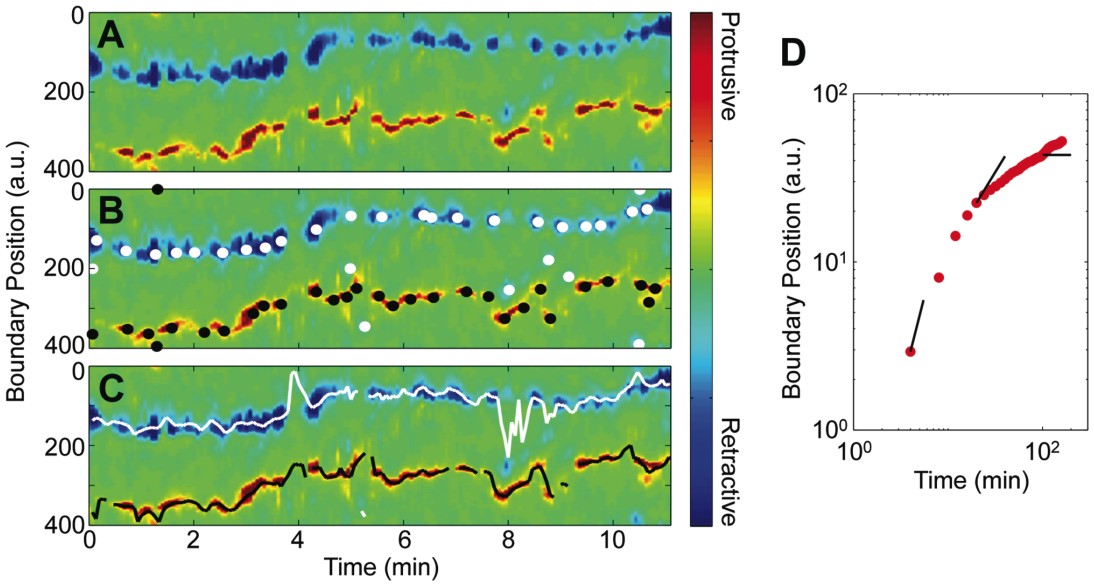

Figure 3.9. **Boundary motion can be analyzed as a series of discrete protrusive and retractive events or as continuous movement. (A) In this plot of the evolution of local boundary motion, protrusive motion appears red, while retractive motion appears blue (see Video 9 of (24)). (B) Extracted individual protrusions are shown as black dots, while extracted retractions are shown as white dots. (C) The averaged location of protrusive and retractive motion, which is defined in each frame where boundary motion is above a noise threshold, are shown here. This cell is also shown in Figure 3.1. (D) The mean squared displacement of the mean protrusive location is ballistic on short time scales. The black lines, from left to right, have slopes of 2, 1 and 0 µm/min.**

characteristics of protrusive motion. First, protrusions are not well separated from each other. Second, many protrusions appear as tilted streaks in the kymograph, indicating that lateral motion occurs during the protrusion.

To analyze protrusive and retractive motion as continuous boundary movement, we define the location of greatest protrusion and retraction activity for

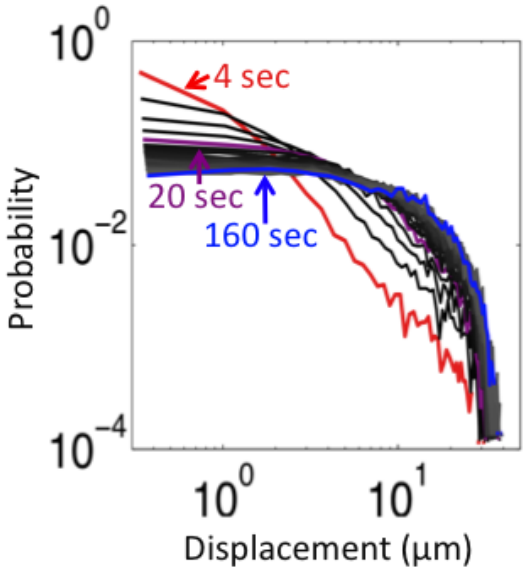

Figure 3.10. **Distributions of the magnitude of mean protrusion displacements along the boundary. The durations of the displacements vary from 4 to 160 seconds.**

each frame as the location of the weighted average of the protrusive or retractive motion. Figure 3.9C shows a representative example of extracted mean protrusion and retraction locations.

We measured the mean squared displacement (MSD) of the average protrusion location along the boundary (Figures 3.9D and 3.10). Note that this is not the MSD of centroid motion, but the MSD of protrusive motion along the boundary of the cell. We find that on short time scales, the protrusive motion along the boundary is nearly ballistic. As the time scale increases, protrusive motion becomes caged to the front of the cell. The transition between the time scales for ballistic and caged motion occurs at roughly 20 seconds, which corresponds to the average frequency of 2.9 ± 0.2 protrusions/minute derived from discrete protrusions. Ballistic motion on short time scales suggests that peak protrusive activity travels along the

boundary in a wave-like manner, similar to the peaks in boundary curvature. We estimate from the MSD at 8 seconds that the speed of these waves is at least 21 μm/min. This estimate is likely to be less than the true wave speed, since local motion (from which the mean protrusion is found) is measured across frames that are obtained 12 seconds apart, and since the displacement is not completely ballistic from 0 to 8 seconds.

Together, these findings indicate that for adherent cells, protrusive activity is continuous and constantly shifts along the leading edge of the cell in a wave-like manner similar to the dynamics of the wave-like high curvature regions observed both in suspended cells and in cells extended over cliff edges.

3.4. Discussion

Using quantitative analysis of cell shape dynamics, we have demonstrated the existence of wave-like characteristics in the local shape of *D. discoideum* and have elucidated their likely role in cell migration.

In order to track the local boundary from frame to frame, we maintained a constant number of boundary points per frame. This approach allows for a robust, 1:1 mapping between points in subsequent frames. Other recent approaches in which the lengths of boundary segments are maintained (64) align the boundary at one predetermined point, and so are most informative only near that point. With a constant number of boundary points per frame, the evolution of the local curvature and local protrusions (or any other metric associated with each boundary point) can be analyzed readily. A constant number of boundary points also makes possible the simple visual representation of shape dynamics through kymographs, which allows us

to represent a movie of a migrating cell in a single image (see Chapter 2). We have two major findings:

(1) The local shape of non-adherent *D. discoideum* exhibits traveling curvature waves. Kymographs of boundary curvature reveal regions of high curvature that start at the leading edge of the cell and travel backward along alternating sides of the cell at an approximately constant speed of ~35 μm/min. Such curvature waves are prominent in cells that are not adherent to the surface (Figure 3.3), and in cells that are extending over the edge of a cliff (Figure 3.4), but are not present in non-adhered *myoII*¯ cells. The curvature waves thus may be associated with acto-myosin dynamics, either actin polymerization waves, which have been found in migrating *D. discoideum* cells (102) and have been observed in other cells such as neutrophils (20), or with dynamic myosin contractility.

(2) The location of protrusive activity shifts continuously and coincides with the source of curvature peaks. Using a measure of local motion, we determined that the locations of protrusive activity are associated with curvature peaks at the fronts of cells (Figure 3.7). In previous studies, protrusions were treated as discrete activities of the cell (68). Some of these studies found that new protrusions often split off from existing protrusions (69), and recent data, which were analyzed by skeletonizing the cell, showed that protrusions can move toward the cell back (99). Other studies found that the direction of the chemotactic signal affects the retractions of existing pseudopods, but not the pattern of generation of new pseudopods (68). Our results show that treating protrusive motion as a continuous process rather than as a series of discrete events provides more detailed information.

Instead of trying to identify individual protrusions, which requires making potentially artificial distinctions among protrusions, we analyze protrusive motion quantitatively as a continuous process, which reveals its fundamentally wave-like character. On short time scales, the location of strongest protrusive activity is not stationary, but shifts along the leading edge of the cell at a speed of at least 21 μm/min for 20 seconds on average.

Local protrusive motion at the cell front transitions from ballistic to caged at about 20 seconds. This 20 second characteristic time is consistent with the finding of Meili *et al.* that, on average, protrusions are extended for 22 seconds before they exert a force on the surface (16). Thus, our findings are consistent with waves of protrusive activity that stop moving when they contact the surface, as observed for neutrophils (20). However, although localized protrusions stop moving relative to the surface, they remain visible as high curvature regions. Curvature peaks then provide insights into the history of protrusive activity, and allow us to compare chemokinesis, chemotaxis, and the motion of non-adherent cells.

Indeed, we find the same results both for self-aggregating wild-type cells and for chemokinesing *aca*$^-$ cells. Chemokinesing cells also have ballistically-traveling curvature waves and zig-zagging protrusions (see Figure 3.5). A group of self-aggregating wild-type cells can be distinguished from a group of chemokinesing *aca*$^-$ cells by their distinct long-term directionality. However, the kymographs of local curvature and local protrusions are not distinguishable. We also present evidence that similar wave processes govern the shape and shape dynamics of both adherent and non-adherent cells. In particular, the kymographs of local curvature are similar for

both types of cells (see Figure 3.1 for adherent cells, compared to Figure 3.3 for non-adherent cells, and Figure 3.4 for cells at the edge of cliffs).

The similarities in protrusive activity and shape dynamics of chemotaxing, chemokinesing, and suspended cells are hard to reconcile with models in which pseudopods are triggered directly by directional chemical signals. Our results are consistent with recent models that treat the cellular migratory apparatus as an excitable system (100), since wave-like and oscillatory dynamics are common in excitable systems.

We hypothesize that wave-like protrusive activity may have three main consequences:

(1) Wave-like protrusions provide a simple and robust mechanism for directed migration. Chemotactic signals are not needed to trigger migration, since protrusive activity is self-sustaining. This view is consistent with observations that cells continue to migrate for hours after a temporary migratory signal (91) without further stimulus and with speed and directional persistence comparable to those of chemotaxing cells. Chemotactic signals merely need to tune the excitability to steer cells (100).

(2) Wave-like protrusions may allow cells to migrate in a viscous environment. Recent reports indicate that both *D. discoideum* and neutrophils can swim in fluids that are significantly more viscous than water (105). Front extension and back retraction, one standard simplified view of amoeboid and neutrophil cell migration, cannot enable migration through a viscous fluid. The traveling protrusive

waves observed here, on the other hand, break symmetry and so could explain the ability of cells to swim.

(3) Wave-like protrusions may allow cells to search for surfaces in 3D environments. Away from a surface, a protrusion that advects backwards along the edge of the cell seems to lead to a wiggling motion (Figure 3.4). This wiggling could in turn act as a search mechanism for surfaces for adhesion. Thus, zig-zag motion, the dominant mode of fast amoeboid migration on a flat surface, may be a side effect of a wave-like migration mechanism that is suitable for both migrating on surfaces and swimming.

3.5. Materials and methods

3.5.1. Cliff fabrication

Micro-cliffs were fabricated using multiphoton absorption polymerization (MAP) (106). The prepolymer resin was composed of 54 wt % dipentaerythritol pentaacrylate (Sartomer), 43 wt % tris(2-hydroxyethyl) isocyanurate triacrylate (Sartomer), and 3 wt % Lucirin TPO-L photoinitiator (BASF). The resin was polymerized using a Ti:sapphire laser (Coherent Mira 900-F) that produced 775 nm, 100 fs pulses at 76 MHz. A 20× objective was used to direct a 17 mW beam into the resin. Using a stage to move the resin through the laser's focal point, 3-D structures were fabricated by polymerizing multiple, closely-spaced lines. The finished cliffs were flat-topped ramps 50 μm tall and 300 μm long (see Figure 3.4A). The horizontal, plateau top and the sloped ramp face were both 100 μm wide, and shared a 300 μm long edge. The cliff was fabricated by polymerizing 300 μm long parallel

lines that were 0.75 μm apart horizontally and 2.5 μm apart vertically. Lines on the top of the ramp (both the plateau and the sloped face) were fabricated with a stage speed of 50 μm/sec, while all other lines were fabricated at a speed of 150 μm/sec. Unpolymerized resin was removed with two, successive, five minute dimethylformamide washes, followed by two, five minute ethanol washes. Each ramp was then replicated with a polydimethylsiloxane mold, as described previously (107). The prepolymer resin described above was cured in the mold for 10 minutes under a UV lamp, the mold was removed, and then the ramp was baked for 10 minutes at 110° C. We previously found that the speed of *D. discoideum* on this cured resin is similar to its speed on glass (108).

3.5.2. Cell culture, imaging, and boundary extraction

D. discoideum cells, wild-type (AX3), adenylyl cyclase A null, and myosin II null (both *aca*$^-$ and *myoII*$^-$ were in an AX3 background) were prepared as described in Chapter 2 and (91). Unless otherwise specified, wild-type and *aca*$^-$ cells were developed for 5 hours. *MyoII*$^-$ cells were developed for 6 hours. Since *myoII*$^-$ cells do not divide in suspension culture, they were harvested directly from plate cultures. In electrostatic repulsion experiments, cells were washed and run in 10^{-3} diluted phosphate buffer. All cells, except in cliff experiments, were cytoplasmically dyed with CellTracker Green CDMFA (Invitrogen) (91). For cliff experiments, phase-contrast images were obtained with a 10× objective every 1.55 seconds. For footprint and polarization experiments, fluorescence, phase contrast and internal reflection microscopy (IRM) images were captured with a 40× objective every 2 or 4 seconds. For electrostatic repulsion experiments, fluorescence images were obtained on a

Leica TCS SP2 confocal microscope with a 100× objective every 2 seconds. For the remaining experiments, fluorescence images were obtained on the same confocal microscope with a 40× objective every 4 seconds.

Image sequences were next pre-processed as described in Section 2.5.2. However, IRM image sequences, which have dark features on a bright background, were first inverted. Phase contrast images were also pre-processed slightly differently. These images were nearly binarized by adjusting the brightness and contrast until the cell interior and exterior were mostly white, and the cell edge mostly black. Unlike fluorescence images, they were not despeckled and the gradient was not taken.

Cell shapes were extracted using a snake algorithm as described in Section 2.5.3.

3.5.3. Analyzing protrusive and retractive motion as continuous motion

The analysis of protrusive and retractive motion as discrete events is described in Section 2.5.6. To analyze protrusive and retractive motion as continuous boundary movement, we found the mean protrusion and retraction locations in frames with boundary movement. Since the first boundary point is adjacent to the 400^{th} boundary point, we used vector addition to calculate the mean values. For each boundary point, a vector was defined with direction $b*(2\pi/400)$, where b is the boundary point label. (Boundary points are labeled counter-clockwise from 1 to 400.) If the motion measure at a boundary point was positive, the magnitude of the associated vector was defined as the magnitude of the motion measure; otherwise, the magnitude was set to zero. We then defined the location of the mean protrusion as the direction of the sum

of a frame's vectors multiplied by $400/2\pi$. If the motion measure at the mean location was below a noise threshold of one pixel, we did not define a mean location for that frame. The mean retraction location was found using an analogous procedure. Figure 3.9C shows extracted mean protrusion and retraction locations. Only mean locations that are defined in consecutive frames and that are less than 200 boundary points apart are shown.

We calculated the mean squared displacement (MSD) of the mean protrusion along the boundary (Figure 3.9D). In the process of calculating the MSD, we found the distributions of the magnitude of mean protrusion displacement over various time intervals, which are shown in Figure 3.10. Notice that from 4 seconds to 20 seconds the distributions flatten quickly, but from 20 seconds to 160 seconds, they flatten much more slowly.

3.5.4. Curvature waves and the cellular footprint

To calculate the distance from the cell boundary to the cell footprint, we first extracted the outlines of the entire cell and of its footprint separately. In frames in which the footprint was composed of multiple disconnected regions, the snake was initialized surrounding all the regions, but upon iteration was allowed to pinch closed between the regions. The resultant snake then appears as outlined regions connected by thin lines. Points in these thin lines were excluded from further analysis by removing points that were extremely close to points with non-adjacent labels. A processed footprint boundary and a cell boundary are both shown overlaid on an IRM image sequence (see Video 8 of (24)).

The distance from the cell boundary to the cell footprint was calculated for each point in the cell boundary. If a cell boundary point was inside the footprint boundary, the distance was defined as zero, otherwise, the distance was defined as the distance from that boundary point to the closest boundary point in the footprint boundary. Figure 3.8 shows the distance from the cell boundary to the cell footprint as a kymograph, while Figures 3.7A and C show the cell boundary curvature and cell boundary motion kymographs for the same cell. Curvature waves, shown as white dashed lines, were drawn on the curvature kymograph and transferred to the distance kymograph. Notice that curvature waves tend to be initiated far from a region of surface contact, but, when they reach the side of the cell, are unusually close to a region of surface contact.

Chapter 4. An application of shape analysis: What can we learn from the shapes of prematurely aged nuclei?

This chapter is adapted from Driscoll, Albanese, Xiong, Mailman, Losert, and Cao (109). The text and figures are used here under the CC BY License. Members of Kan Cao's lab performed all of the experiments, and Meghan Driscoll analyzed the nuclear shapes.

4.1. Overview

The premature aging disorder Hutchinson-Gilford progeria syndrome (HGPS) is caused by mutant lamin A, which affects the nuclear scaffolding. The phenotypic hallmark of HGPS is nuclear blebbing. Interestingly, similar nuclear blebbing has also been observed in aged cells from healthy individuals. Recent work has shown that treatment with rapamycin, an inhibitor of the mTOR pathway, reduced nuclear blebbing in HGPS fibroblasts. However, the extent of blebbing varies considerably within each cell population, which makes manual blind counting challenging and subjective. Here, we demonstrate an automated, high-throughput nuclear shape analysis technique that quantitatively measures boundary curvature, area, perimeter, eccentricity and additional metrics of nuclear morphology for large populations of cells. We examined HGPS fibroblast cells treated with rapamycin and RAD001 (an analogue to rapamycin). Our analysis showed that treatment with RAD001 and

rapamycin similarly reduces nuclear blebbing, consistent with blind counting controls. In addition, we found that rapamycin treatment reduced nuclear area, but left eccentricity unchanged. Our nuclear shape analysis provides an unbiased, multidimensional "fingerprint" for a population of cells, which can be used to quantify treatment efficacy and analyze cellular aging.

4.2. Background

In this chapter, we apply the shape analysis techniques used in Chapters 2 and 3 to a system that is very different from amoebae: prematurely aged nuclei. When analyzing the amoebae we explored patterns in shape dynamics, while, when analyzing the nuclei, we looked for patterns in ensembles of static shapes.

Hutchinson-Gilford progeria syndrome (HGPS) is a rare genetic disease that occurs in approximately 1 out of 4 million live births (76). Visible symptoms of patients with HGPS include a pronounced forehead, short stature, receding mandible, conspicuous veins in the scalp, alopecia and diminished subcutaneous fat (76, 110-112). Internally, such patients undergo accelerated organ degeneration. The average life expectancy of HGPS patients is just 14 years, with death typically resulting from heart attack or stroke (76).

The genetic mutation that leads to HGPS occurs in exon 11 of the human *LMNA* gene, which plays a role in nuclear scaffolding (113, 114). This HGPS mutation is a *de novo* single nucleotide substitution (1824 C => T), which does not change the amino acid coding sequence [GGC (glycine) => GGT (glycine)]. However, this mutation partially activates a cryptic splice donor site, which causes a 150-nucleotide sequence to be spliced out of exon 11 and leads to the production of

the mutant protein progerin, also known as LAΔ50 (115). Because of this internal deletion, progerin does not contain the cleavage site required for the removal of the farnesyl group by protease Zempste 24, so the farnesyl group remains attached to progerin (76, 77). The farnesyl chain is hydrophobic and has a strong affinity for the inner nuclear membrane. As a result, progerin inserts into the nuclear membrane abnormally, causing bulging of the nuclear envelope. The resultant abnormal nuclear shape, commonly referred to as "blebbed nucleus", is the hallmark cellular phenotype for HGPS cells (76, 77), yet the molecular and physical mechanisms of nuclear blebbing are not well understood. In addition, progerin results in alterations in histone methylation, a thickened nuclear lamina, genome instability, clustering of nuclear pores, and loss of heterochromatin (116). As progerin continues to build up inside prematurely aged cells, the nuclear blebbing phenotype and other damaging effects become more severe (116). Cellular division is also affected in HGPS cells: during mitosis, when the nuclear envelope disassembles, progerin forms aggregates with membranes, interferes with nuclear membrane disassembly, and mislocalizes to the cytoplasm after mitosis, leading to chromosome mis-segregation and binucleation (117, 118).

Much work has been done to develop a cure for HGPS and children are currently participating in the first clinical trial for HGPS. This trial tests a drug therapy that uses farnesyl transferase inhibitors (FTIs), which block the addition of the farnesyl group to progerin (77, 119-121). Macrolide antibiotic rapamycin was recently shown to reverse nuclear blebbing and other phenotypes in HGPS cells by down-regulating progerin (122-124). This reversal suggests that rapamycin is a

potential treatment for HGPS. In both FTI and rapamycin studies, the percentage of nuclear blebbing, as scored by blind observers, was used as an indication of drug effectiveness. However, it is not possible to define unambiguously whether a cell is blebbed because many cells in both healthy and diseased populations contain minor abnormalities in nuclear shape. Hence, the fraction of cells counted as blebbed can vary considerably among different observers.

A number of studies have suggested a strong connection between HGPS and the normal aging processes. In 2006, Misteli's group reported the detection of progerin mRNA and protein in cells obtained from healthy individuals, indicating that the cryptic splice site in exon 11 is also used in the presence of the normal sequence of exon 11 (125). Similar to the results described above, low levels of progerin were recently detected in normal cells, and a significant percentage of these cells had mitotic defects similar to those found in HGPS cells (117). A recent study further revealed a causative connection between dysfunctional telomeres and the cryptic splicing of lamin A (126). Moreover, studies using tissues taken from normal human subjects revealed that at any age, the cryptic splicing event takes place in skin, and that as we grow older, progerin-positive fibroblasts become more abundant (127, 128). Thus, one may expect a broad distribution in the severity of blebbing in a normal cell population and an increase in blebbing with aging.

Here, we report an automated, quantitative method that we used to study distributions of blebbing in a large cell population. In this method, nuclear morphology, as visualized by immunofluorescence staining of lamin A/C, is quantified using image analysis software that extracts the nuclear boundary from

optical micrographs and then calculates measures, such as area, perimeter, and curvature, for each nucleus. For each set of treated cells, the curvature of all of the nuclei can be further visualized in a single plot. Since curvature is a mathematically complete description of shape, these plots allow for the quick assessment of the severity of blebbing in a population of nuclei. We applied our method to examine HGPS fibroblasts treated with either mock, rapamycin, or RAD001, a derivative of rapamycin with better tolerance in patients. We found that treatment with RAD001 or rapamycin decreases both blebbing and nuclear area in a dosage dependent manner, but leaves nuclear eccentricity unchanged. Our technique is an unbiased, quantitative method for analyzing HGPS and aging cells. This technique could be useful for future drug screenings for HGPS or other age related diseases, patient diagnostics, and quantitative modeling of nuclear shape.

4.3. Results

4.3.1. Measurement and analysis of nuclear shape

In order to test our automatic analysis of nuclear shape, fibroblasts from two HGPS fibroblast cell lines (HGADFN155-p15 and HGADFN167-p12, HGPS1 and HGPS2 respectively) and from one normal control cell line (HGFDFN168-p14, normal) were cultured. The cells were fed with fresh MEM medium containing 15% FBS and grown at 37 °C. To visualize the nuclei, we performed immunofluorescence staining of the nuclear membrane with a mouse monoclonal antibody raised against lamin A/C (MAB3211) was perfomed. This antibody has been well characterized in HGPS cells and has also been used in studies of other laminopathies. Fluorescence

images of about 100 randomly selected nuclei per cell line were taken with a Zeiss fluorescence microscope at 400X magnification (examples are shown in Figure 4.1A). A custom-written Matlab program was used to extract nuclear shapes and properties of the shape, such as boundary curvature. In Figures 4.1A and B, the nuclear boundaries, which are colored by curvature, are shown overlaid on the microscopy images. Convex curvatures were kept positive, while concave curvatures were made negative. As shown by the color bar in Figure 4.1C blue represents regions of large positive curvature, and red represents regions of large negative

Figure 4.1. **The boundary curvature of HGPS and normal nuclei. (A) The curvature of nuclei is automatically extracted from fluorescence images of anti-laminA/C immunostaining. Here, the curvature of HGPS and normal nuclei is shown as a colored outline, where blue represents regions of large positive curvature and red represents regions of large negative curvature (scale bar: 10 μm). Blebbed nuclei have more regions of negative curvature, and so have more red signals. (B) High-magnification examples of the extracted boundary curvature of a blebbed, HGPS nucleus, and a more oval, normal nucleus (scale bar: 10 μm). (C) The boundary curvature of hundreds of nuclei can be represented in a single heat map. In these heat maps, which here correspond to two HGPS cell lines (HGPS1 and HGPS2, respectively) and one control cell line (Normal), each vertical line is the stretched, colored outline of a single nucleus. Regions of large negative curvature are colored blue while regions of large negative curvature are colored red. (D) The nuclei are ordered from left to right by increasing mean negative curvature (MNC), which is shown in the line plots. (E) The MNC of populations from both HGPS cell lines is statistically different from the population from the normal control, as illustrated in this histogram.**

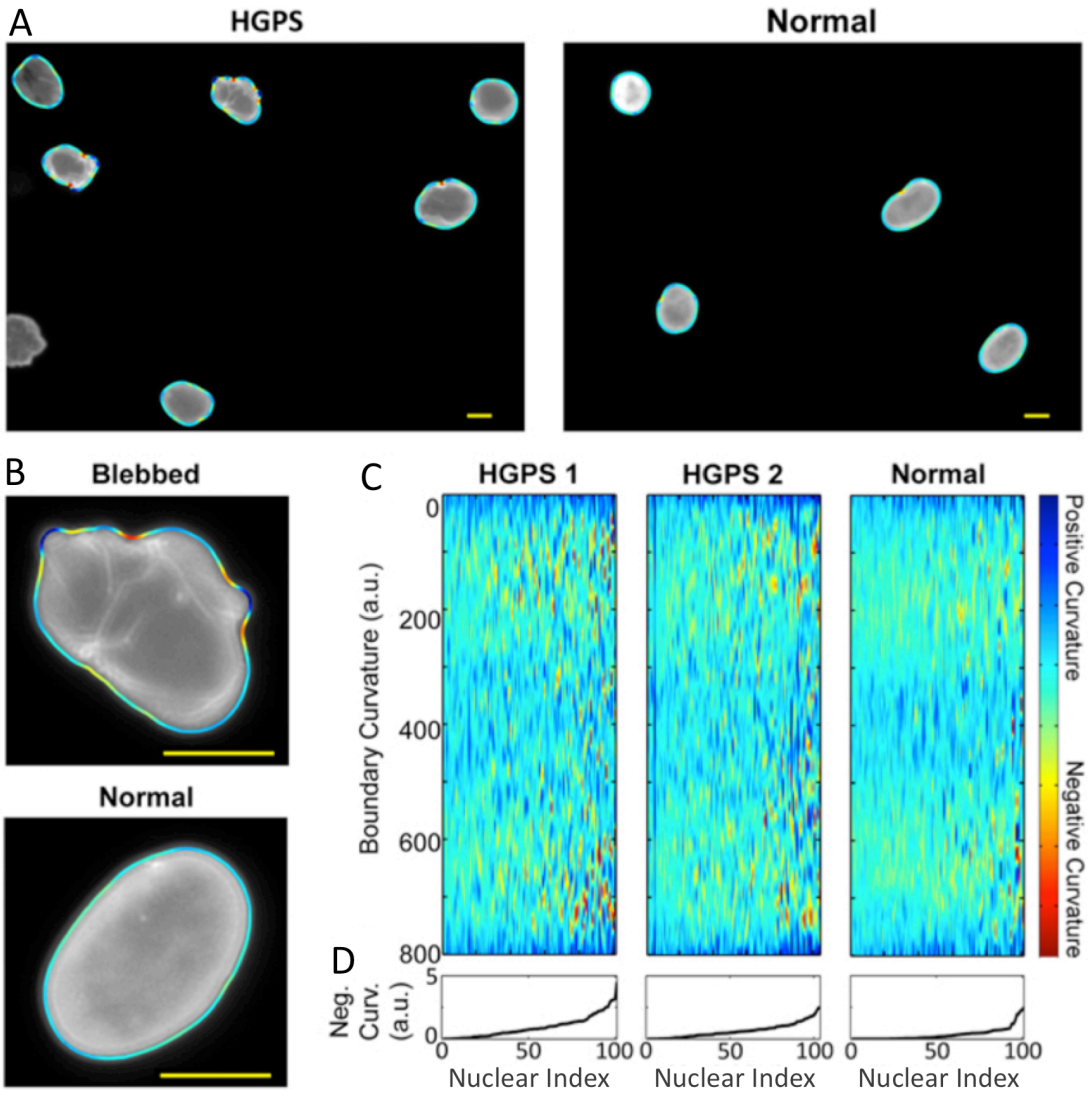
A
HGPS
Normal
B
Blebbed
Normal
C
HGPS 1
HGPS 2
Normal
Boundary Curvature (a.u.)
0
200
400
600
800
Positive Curvature
Negative Curvature
D
Neg. Curv. (a.u.)
5
0
0
50
100
Nuclear Index
E
Mean Negative Curvature
0.0025
0.0020
0.0015
0.0010
0.0005
0.0000
p < 0.0001
p = 0.0005
HGPS1
HGPS2
Normal

curvature. A blebbed cell, such as the cell shown in the top of Figure 4.1B, will have boundary regions that are dark red and dark blue, whereas a non-blebbed cell, such as the cell shown in the bottom of Figure 4.1B, will have boundary regions that are mostly blue and green with almost no red.

We next assembled plots that, for each cell line, display the boundary curvatures of all of the measured nuclei, as shown in Figure 4.1C. In these heat maps, each vertical line represents the boundary curvature of one nucleus. To construct such a plot, imagine cutting each colored boundary at the location farthest from the nucleus center (that location is labeled 0 on the heat map), pulling the boundary straight, and then lining it up next to the colored boundaries of the other nuclei. The heat maps of blebbed populations, such as the HGPS cell lines, have many red speckles, whereas the heat maps of unblebbed populations, such as the control cell line, have few red speckles.

Within each plot, the nuclei are ordered from left to right by increasing mean negative curvature (MNC), a measure of nuclear blebbing. We defined the MNC of each nucleus by averaging all negative curvatures, excluding the positive curvatures entirely, and taking the absolute value. As shown in Figures 4.1D and 4.1E, the HGPS1 and HGPS2 cell lines have larger MNCs, and hence are more blebbed, than the control cell line. HGPS1 also has a larger MNC than HGPS2, perhaps because HGPS1 is at a later cellular passage, and thus more senesced. We found that both HGPS MNC distributions are statistically different from the MNC distribution of the control (see Figure 4.1E for p values).

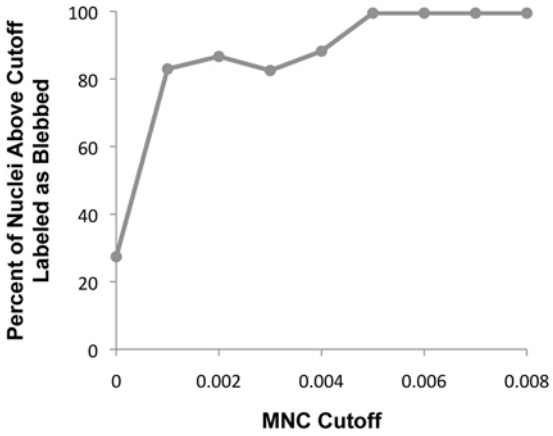

Figure 4.2. **Mean negative curvature (MNC) correlates with bleb counting. Images of 847 nuclei from HGPS and normal control cell lines were separately displayed to three members of the Cao lab. Each member selected the nuclei he or she considered to be blebbed. The selections were saved and analyzed through a custom-written Matlab program. The percentage of all nuclei with an MNC above a certain threshold that were labeled blebbed by the majority of counters (two or more) is displayed for various MNC thresholds.**

To validate the automated nuclear shape analysis, we also assessed nuclear morphology using the standard technique: manual blind counting. Nuclei with protrusions or invaginations were counted as blebbed, while other nuclei were counted as normal. We found that 73% of HGPS1 nuclei, 63% of HGPS2 nuclei, and 24% of normal nuclei were abnormal. These counts are in quantitative agreement with the MNC distributions of the respective cell lines (Figure 4.1E). For better evaluation of the correlation of manual counting with quantitative shape metrics, we had experienced human counters label individual nuclei as either normal or blebbed, and analyzed the MNC of the two populations. The analysis shows a positive

correlation between MNC and the percentage of nuclei that were labeled as blebbed (Figure 4.2).

Since the automated analysis extracts the boundary of each nucleus, we can assess nuclear morphology using various shape metrics besides boundary curvature. For each nucleus, we also calculated area, perimeter, number of invaginations, eccentricity and other metrics. In analogy to the analysis of microarray data to find relationships among genes, we used correlations to measure the interrelationships between 15 different measures of nuclear shape. We hierarchically clustered the 15 measures of nuclear shape and laminA/C fluorescence intensity (Figure 4.3). We found several families of nuclear measures that roughly correspond to size, extent of blebbing, eccentricity, laminA/C fluorescence intensity, and the standard deviation of fluorescence intensity. The clustering reassures us that the intensity, which is affected by immunostaining and imaging, does not notably affect the measured MNC. The clustering also indicates that the standard deviation of MNC and tortuosity are measures related to MNC. Also related to mean MNC is the solidity, which is the ratio of the measured area and the area of the convex hull. The convex hull is the minimal convex shape that bounds the measured shape of the nucleus.

As a control experiment, we tested whether the cell density would influence the MNC. Cells from the same HGPS cell line were seeded at densities of 3000, 9000, and 27000 cells per well in 4-well chamber slides (Figure 4.4). The three densities did not appear to have different MNC distributions, nor were the measured MNC distributions statistically distinct.

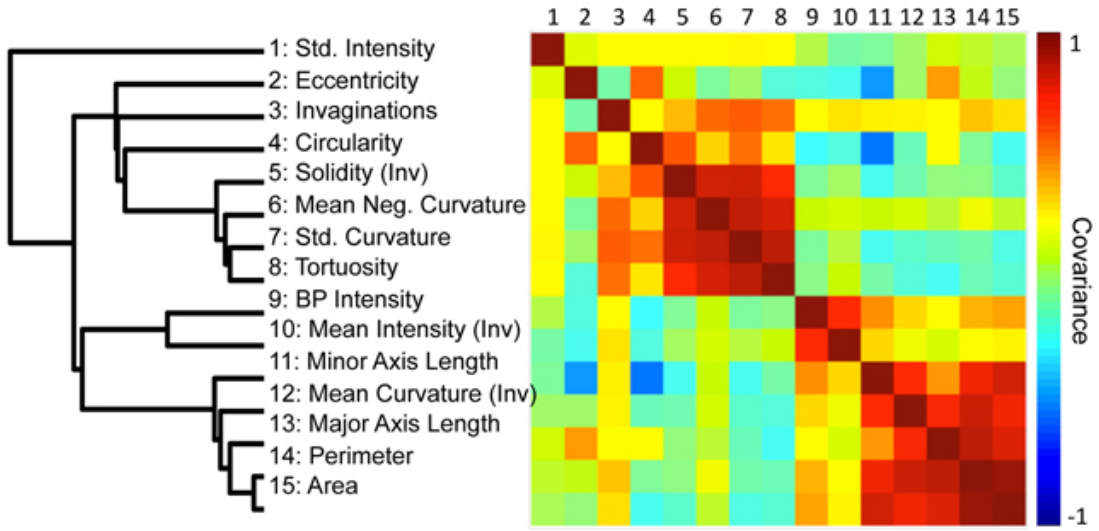

Figure 4.3. **Covariance matrix (right) and hierarchical clustering plot (left) of 15 measures of nuclear shape and lamin A/C fluorescence intensity. Each box in the covariance matrix indicates the amount of correlation between two measures. High covariance is indicated in red (see color bar).**

4.3.2. RAD001 and rapamycin similarly reduce blebbing

Recent work has revealed that rapamycin, an mTOR (mammalian target of rapamycin) inhibitor, significantly reduces the phenotypic hallmarks of progeria in HGPS cells by down-regulating progerin (122). Everolimus (RAD001), which is the 40-O-(2-hydroxyethyl) derivative of rapamycin, works similarly to sirolimus as an mTOR inhibitor but is better tolerated by patients. In order to compare the efficacy of RAD001 to rapamycin, we treated HGPS fibroblasts with rapamycin, RAD001, or mock, and then analyzed the nuclear morphology of each treatment group.

Cultured fibroblasts from an HGPS patient (HGADFN155-p15) and a normal individual (HGFDFN168-p15) were used in this experiment. The cells were fed

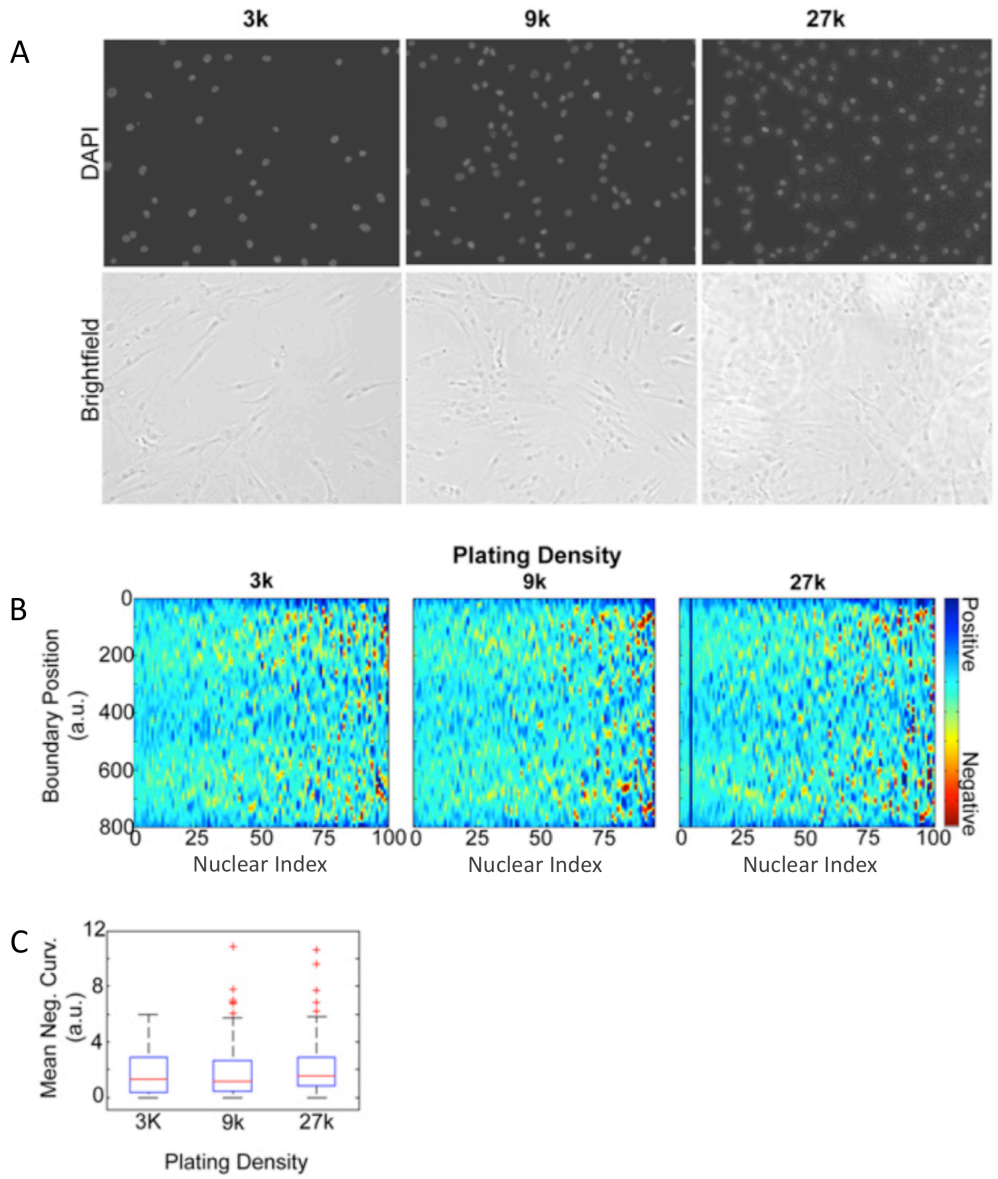

Figure 4.4. **The plating density of the cells does not affect the curvature analysis. (A) HGPS fibroblast cells were seeded at various cell densities (3000, 9000, and 27000 per well) in 4-well chamber slides and immuno-stained with anti-lamin A/C and DAPI. Images of the nuclear staining with DAPI and brightfield images are presented to help visualize the various cell densities. (B) Heat maps of curvature contours of 100 randomly selected nuclei for each density show a similar degree of blebbing at all cell densities. (C) Box plots of the MNC of nuclei imaged in the heat maps.**

every other day with fresh MEM medium containing 0.68 μM rapamycin, 0.1 μM RAD001, 0.5 μM RAD001, or the same volume of vehicle (DMSO, 0.025% v/v) for a duration of seven weeks. To examine the effects on nuclear morphology, the cells were labeled with an antibody for lamin A/C and an antibody specific for progerin (Figure 4.5A). To judge the impact of rapamycin and RAD001, the percentage of nuclei with abnormal morphology were first scored in the usual way by manual blind counting. At least 200 randomly selected cells were scored by fluorescence microscopy for each cell line under each condition. In comparison with the passage-matched, mock-treated HGPS cells, the rapamycin or RAD001 treated HGPS cells exhibited a clear reduction in nuclear blebbing (Figure 4.5B). Since increased genome instability was reported in HGPS cells (122, 129, 130), we also examined whether RAD001 treatment can improve this phenotype. Using immunofluorescence staining, we observed a reduction in 53BP1 foci in rapamycin or RAD001 treated cells, indicating that inhibition of mTOR prevents DNA damage induced in prematurely senescent cells by progerin (Figure 4.6). Quantification of progerin protein by western blotting analysis also revealed an over 50% reduction in progerin levels in rapamycin and RAD001 treated HGPS cells (Figure 4.5C). We also detected a weaker progerin-staining signal in almost all of the rapamycin or RAD001 treated HGPS cells, and their nuclear morphology appeared substantially improved compared to untreated cells (Figure 4.5A).

Consistent with the findings of Cao *et al.* (122), there was a reduction in overall cell proliferation at the beginning of the treatments (less than two weeks) with either rapamycin or RAD001 compared to the mock treated samples. A tetrazolium

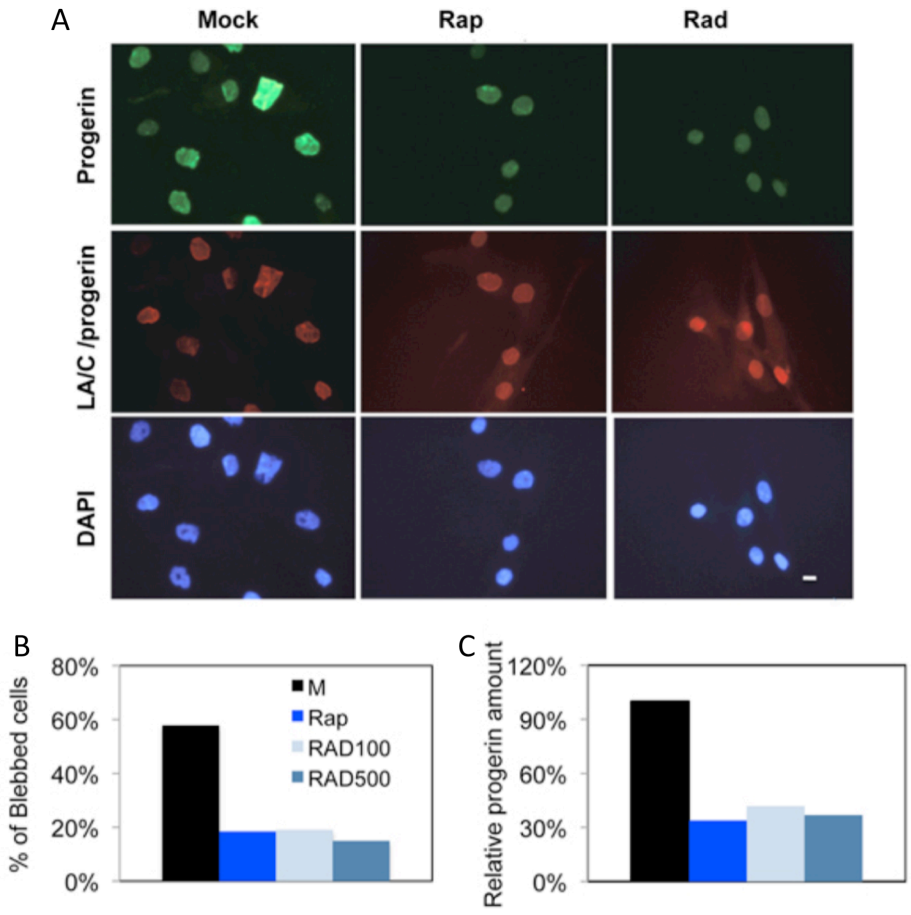

Figure 4.5. **The nuclear morphology and progerin levels of rapamycin and RAD001 treated HGPS cells. (A) The nuclear blebbing phenotype was improved in RAD001 and rapamycin treated HGPS fibroblast cells. Cells were stained with DAPI (blue), laminA/C antibody (red), and progerin antibody (green) to show nuclear location and morphology. The treatment duration was for seven weeks. Mock: vehicle (DMSO, 0.025% v/v); Rap: 0.68 µM rapamycin, Rad: 0.1 µM RAD001. (Scale bar: 10 µm) (B) Quantification of the percentage of blebbing in all treatments. At least 200 nuclei were counted blindly. M: vehicle (DMSO, 0.025% v/v); Rap: 0.68 µM rapamycin; RAD100: 0.1 µM RAD001 treatment; RAD500: 0.5 µM RAD001 treatment. (C) Progerin was decreased in rapamycin and RAD001 treated HGPS fibroblasts. The relative amount of progerin was quantified using quantitative western blotting analysis and compared to the mock-treated HGPS cells.**

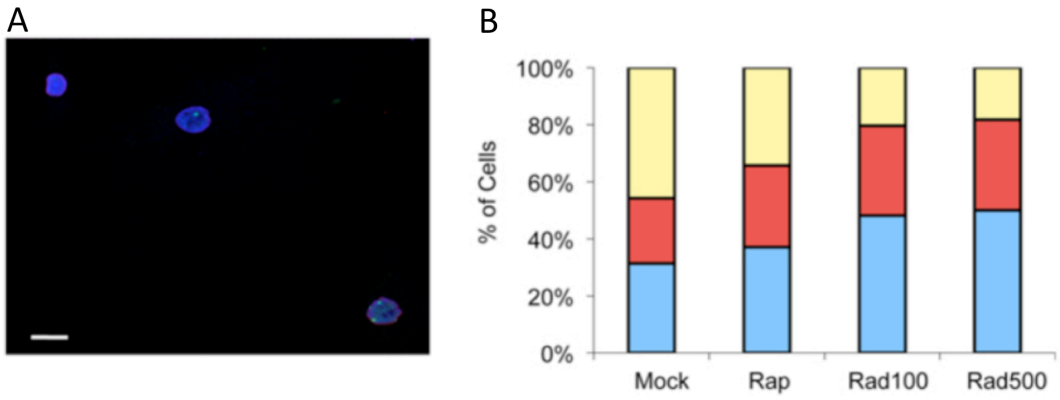

Figure 4.6. **Genome stability is improved in rapamycin or RAD001 treated cells. (A) Fibroblast cells were immuno-stained with DAPI (blue) and TP53BP1 antibody (green); scale bar: 20 µm. (B) Percentage of TP53BP1 foci-positive cells in Rad100, Rad500, rapamycin and mock treated HGPS cells. Mock: mock treatment; Rap: 0.68 µM rapamycin treatment; Rad100: 0.1 µM RAD001 treatment; Rad500: 0.5 µM RAD001 treatment. The percentage of cells with no TP53BP1 staining is shown in blue, the percentage of cells with one TP53BP1 is in red, and percentage of cells with more than one TP53BP1 focus is shown in yellow.**

salt-based cell proliferation assay (WST1 assay) was used to analyze this apparent cell growth inhibition for the concentrations of RAD001 used in the experiment: 0, 20, 60, 100, and 500 nM. Figure 4.7 shows that all treatments for both control and HGPS cell lines had a similar reduction in cell proliferation compared to the mock treatments (less than 40%), suggesting that any effective dose of RAD001 may have similar anti-hypertrophic effects (131).

In parallel to the blind counting, immunofluorescence images were taken of about 100 randomly selected nuclei per treatment group and their nuclear morphologies were automatically analyzed. Heat maps, which display the boundary

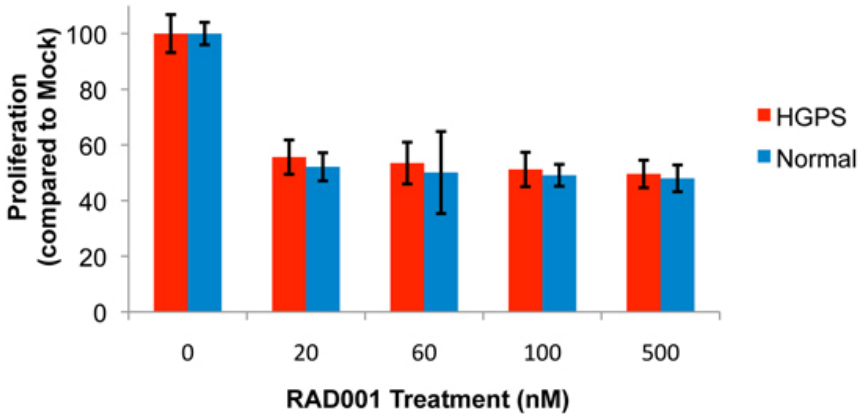

Figure 4.7. **A cell proliferation assay shows that all treatments of RAD001/DMSO at indicated dosages for both normal (blue) and HGPS (red) fibroblast cell lines had similarly reduced growth compared to the mock treatments. All treatments were controlled for DMSO at 0.1% and percent survival calculated relative to the cell numbers of the mock treatments.**

curvature of the treated HGPS cells, are shown in Figure 4.8A. From the heat maps we see that the mock treated cells are much more blebbed than the rapamycin or RAD001 treated cells, which is consistent with our blinded counting. Indeed, we found that the MNC distributions of the rapamycin- and RAD001-treated cells were statistically different from that of the control group (Figure 4.8B). Similarly, our analysis showed a reduction in the number of invaginations in treated HGPS cells (Figure 4.8D).

Interestingly, we also found that the RAD001- and rapamycin-treated nuclei had a smaller area than the mock treated nuclei (Figure 4.8C). Moreover, we noticed that the eccentricity, which is a measure of how elongated the nuclei are, did not change as a result of the rapamycin or RAD001 treatments (Figure 4.8E). Our

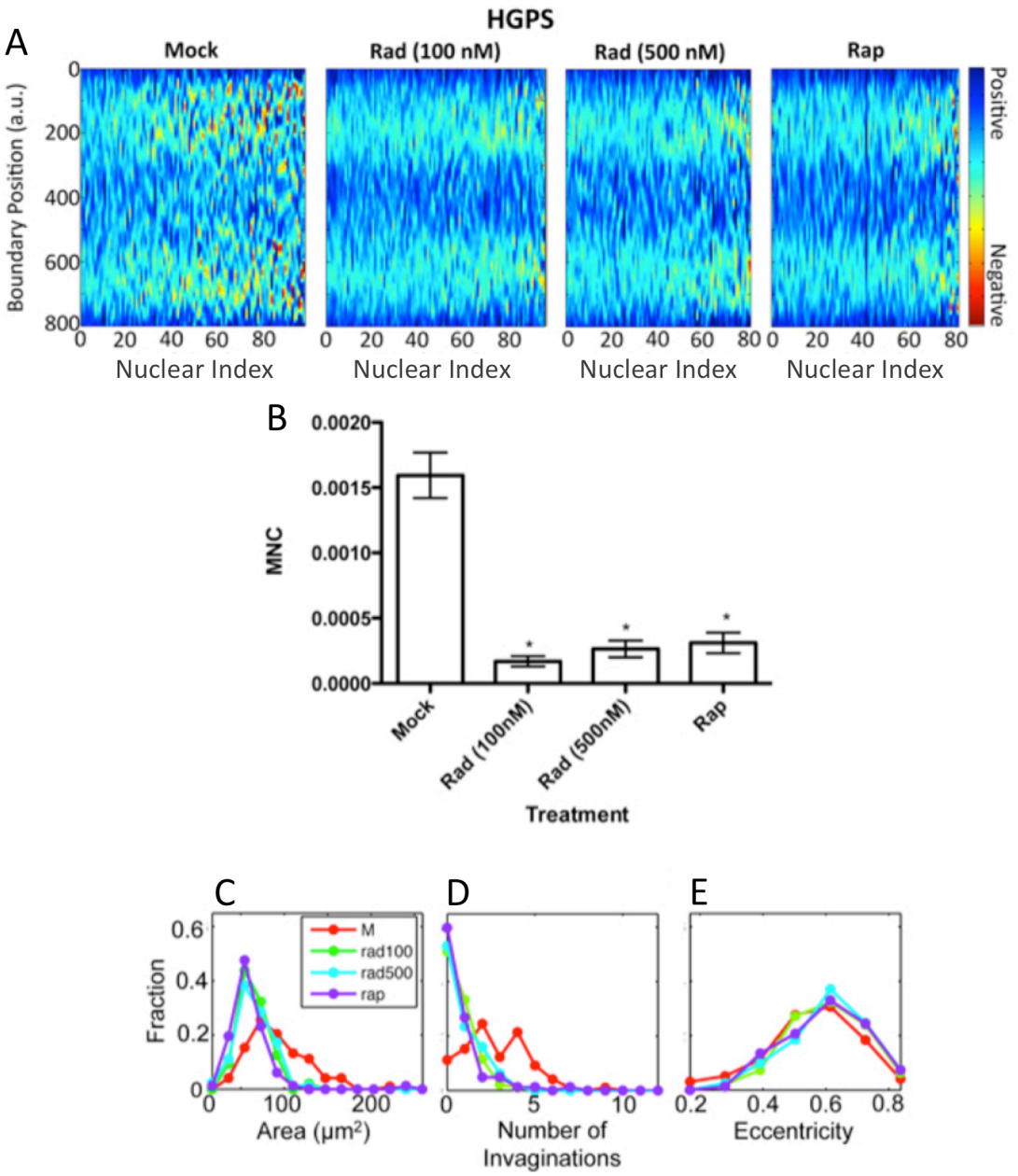

Figure 4.8. **Imaging analysis of RAD001 and rapamycin treated HGPS cells. (A) Heat maps that represent the boundary curvature of the HGPS cells treated with the vehicle (mock), 100 nM and 500 nM RAD001 (Rad), and rapamycin (Rap). (B) The MNC of populations from the mock-treated HGPS cell lines is statistically different from the MNC of populations of RAD001 or rapamycin treated cells ($p < 0.001$) (C-E) Compared to the mock treated nuclei, the RAD001 and rapamycin treated nuclei have (C) smaller areas (D) fewer invaginations, (E) but similar eccentricities.**

analysis suggested that rapamycin or RAD001 treatments appear to improve abnormal morphology locally without affecting the overall shape of the nuclei. These treatments do still alter nuclear size (see Section 4.4.). In summary, our data suggest that, similar to rapamycin, RAD001 can reverse diseased nuclear phenotypes in HGPS cells by promoting progerin clearance.

4.3.3. RAD001 induces a dosage dependant change in nuclear morphology

Based on the above analysis, we suggested that RAD001 could be used at 100 nM concentration to achieve similar beneficial effects in HGPS cell cultures as rapamycin at 0.68 μM as described in Cao *et al.* (122). Next, we explored the sensitivity of the curvature analysis program, since quantitative image analysis is most useful if it can reveal small changes that are difficult to observe. Thus, we lowered the dosage of RAD001 to 20 or 60 nM, and shortened the duration of treatment to two weeks. An HGPS fibroblast cell line (HGADFN167-p15) and a control fibroblast cell line (HGFDFN168-p15) were fed with fresh MEM medium containing 20 nM RAD001, 60nM RAD001 or the same volume of vehicle (0.3% DMSO) every other day. Nuclear curvature outline and heat map analyses of MNC were carried out at the end of the two-week treatment (Figure 4.9A). Box plot analysis indicated a significant reduction of MNC in the HGPS cell line, even in the cells receiving 20 nM RAD001 (Figure 4.9B), while those minor morphological improvements were not visible with the traditional blinded counting method, suggesting that the automated analysis is more sensitive. Importantly, we noticed a dosage dependent reduction in area of the nuclei of both treated HGPS and treated

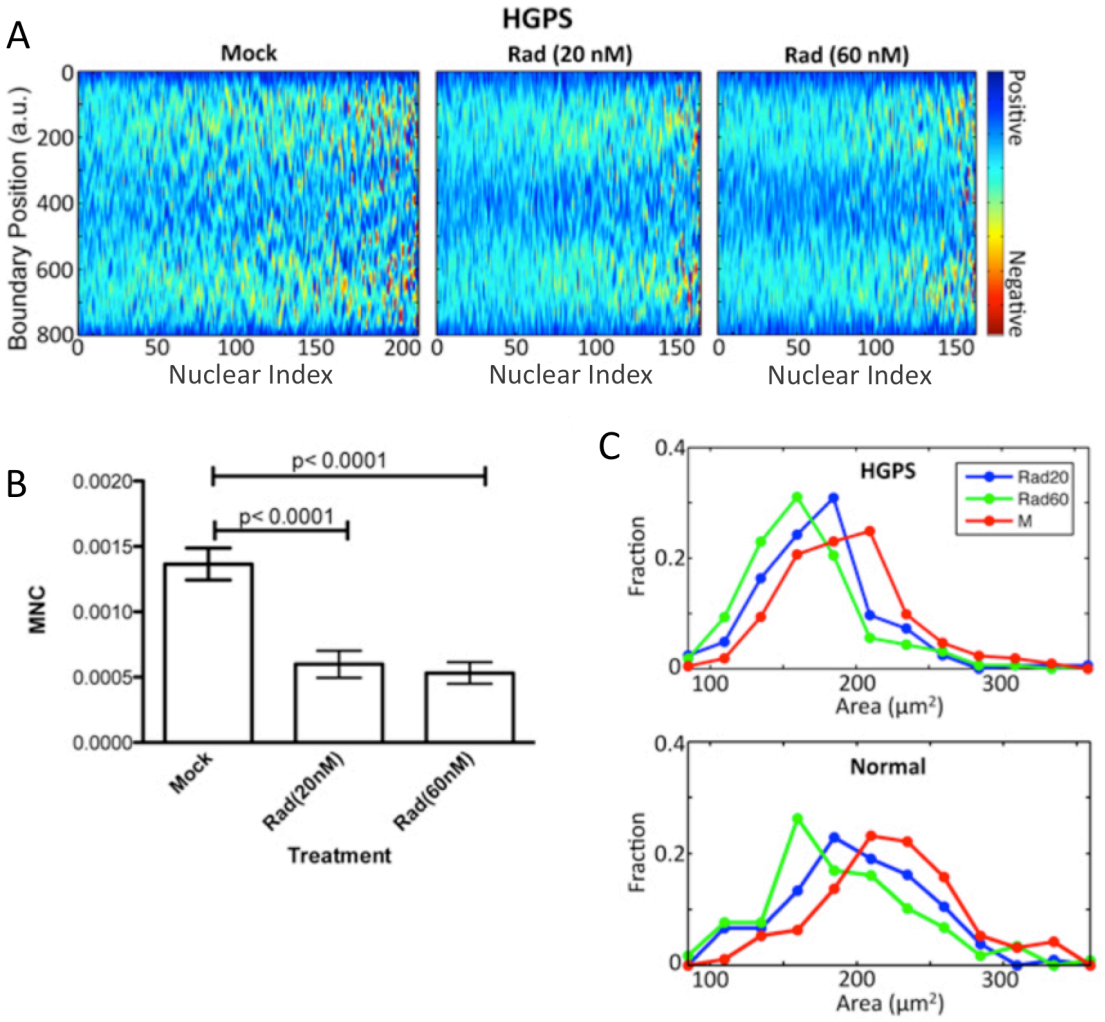

Figure 4.9. **RAD001 induces a gradual change in nuclear morphology in a dosage dependant manner. (A) Heat maps that represent the boundary curvature of HGPS cells treated with the vehicle (mock) or 20 or 60 nM RAD001. (B) Both doses significantly reduce the mean negative curvature as shown by the histogram. (C) The area of mock-treated nuclei is greater than both doses of RAD001-treated nuclei, but the nuclei that received the smaller dose of RAD001 have greater area than the nuclei that received the larger dose. The same trend in area change is apparent to the same extent in the treated control normal fibroblasts.**

control cells (Figure 4.9C): the area of mock-treated nuclei was greater than both doses of RAD001-treated nuclei, but the nuclei that received the smaller dose of RAD001 (20 nM) had greater area than the nuclei that received the larger dose (60 nM). This result suggests that the improvement in nuclear shape is a gradual process. The area reduction is primarily due to non-specific effects of the drug treatment, and incremental improvement during treatment can be captured and quantified by this boundary curvature analysis.

4.4. Discussion

One of the hallmarks of HGPS is an abnormal, blebbed nuclear shape, which has been the main identifying morphological feature of HGPS cell lines and has been used to determine the effectiveness of HGPS treatments. The traditional method of measuring blebbing is manual blind counting of blebbed nuclei. However, this method has no standard criteria and is extremely time consuming. Sorting the nuclei into two categories, normal and blebbed, also obscures the fact that blebbing is not an either/or phenomenon, but varies continuously. The subjectivity and variability of this method makes it impossible to compare values obtained by different counters. The need for an unbiased, quantitative method for measuring the extent of blebbing is clear.

We present an automated image analysis method that uses boundary curvature as a measure of blebbing. Using a custom-written program, we extracted the boundaries of immuno-stained nuclei and calculated measures of nuclear shape, such as boundary curvature. We found that several measures of the shape differentiated between HGPS and normal control cell lines. We focused on the most intuitive

measure, the mean negative curvature (MNC), which is the average of all of the concave curvatures on the nuclear boundary. MNC provides a continuous measure of blebbing that can be further analyzed using quantitative and statistical methods. We analyzed different seeding densities (Figure 4.4) and exposure times (data not shown) to demonstrate that MNC is also a consistent measure that does not vary significantly between experiments. The cluster analysis also showed that intensity does not affect the measured MNC (Figure 4.3). Thus, MNC values can be compared between samples and experiments, unlike values obtained from the traditional manual counting method. A caveat, however, is that MNC is affected by pixel size and smoothing, thus care should be taken when comparing results from different laboratories. Of the other measures that strongly correlate with MNC, according to our clustering analysis (Figure 4.3), solidity should not be significantly affected by pixel size or smoothing and thus may be a viable alternative.

As an additional demonstration of the usefulness of this novel analysis, we treated HGPS and control cell lines with rapamycin, an mTOR pathway inhibitor that has been shown to improve nuclear morphology of HGPS cells. Cells were also treated with a rapamycin analogue, RAD001, which is better tolerated by patients. The cells were treated for seven weeks, stained with an anti-lamin A/C antibody, and analyzed using the program. Results of the treatments are presented through heat maps and box plots of MNC in Figure 4.8. Blinded, manual counting of blebbed cells was also performed (Figure 4.5), and MNC values agreed with the established method. RAD001- and rapamycin-treated HGPS cells had similar, significantly improved nuclear morphology. Consistent with Cao *et al*. (122), we found that

RAD001 promoted progerin degradation (Figure 4.5). In addition, we reported that RAD001 and rapamycin treatments decreased the DNA-damage-induced 53BP1 formation of foci in HGPS cells (Figure 4.6), likely through down-regulation of progerin. Consistent with our observations, previous studies have shown that rapamycin can inhibit the DNA-damage-independent, pseudo DNA-damage response, which might be caused by general over activation in senescent cells (132, 133).

To demonstrate the sensitivity of this method, we distinguished between treatment doses that cannot be differentiated by the traditional manual, counting method (Figure 4.9). HGPS and control cell lines were treated with lower doses of RAD001 and Student's t-tests were used to show a statistically significant increase in MNC even at lower doses. A blinded bleb count was unable to demonstrate any difference between the treatments (data not shown). In these treatments, we again noticed a dose-dependent change in nuclear area (Figures 4.8C and 4.9C). However, the same area change was observed in the treated normal control cell line, suggesting that this area change is primarily due to the action of mTOR inhibition and not an improvement of nuclear morphology in HGPS cells. Anti-hypertrophic effects of RAD001 were also found in the early stages of treatment — within the first week at the indicated concentrations (Figure 4.7). The reduced cellular growth in the initial period of treatment and the area decrease of nuclei may be explained by the inhibition of the mTOR pathway. After the initial slowdown in growth during the first two weeks of treatment, rapamycin and RAD001 treated cells showed a greatly improved proliferation rate, better than their mock treated counterparts (122), which is consistent with the previously established role of rapamycin in preventing the loss of

proliferative potential in cultured cells (134). Notably, our multidimensional analysis of cell shapes provides unexpected hints into the mechanical aspects of mTOR inhibition: while RAD001 or rapamycin treatment decreases blebbing and nuclear size, they do not alter the eccentricity of the nuclear shape (Figure 4.8E). We expect that our high throughput, multi-dimensional measures will provide a solid foundation for developing mechanical models of the nucleus.

HGPS is a devastating and well-studied premature aging disease that currently has no effective treatment. HGPS is strongly linked to the general aging process. In both HGPS and aging, the broad distribution of nuclear shape abnormalities in a population of cells hampers manual analysis. Our automated nuclear shape analysis software provides a high-throughput and easy-to-use method of quantifying nuclear morphology. Heat maps of curvature (Figures 4.1, 4.8, and 4.9) allow us to visualize the broad distribution of nuclear blebbing directly in a large cell population. Comparing measures between samples allows us to assess treatment efficacy for HGPS and other age-related diseases. We used this method to demonstrate the potential of RAD001 as an alternative treatment for HGPS. Our nuclear shape analysis method provides an unbiased multidimensional fingerprint for a population of cells, which can be used to quantify treatment efficacy and analyze cellular aging.

4.5. Material and methods

4.5.1. Cells, cell culture, and treatments

Primary human dermal fibroblasts used in this study were obtained from the Progeria Research Foundation (PRF): two HGPS fibroblasts, HGADFN155 and

HGADFN167, and a control normal fibroblast line, HGFDFN168. Fibroblasts were cultured in MEM medium (Invitrogen) supplemented with 15% FBS and 2 mM L-glutamine under 5% CO2 at 37°C. Normal and HGPS fibroblasts were replenished with fresh MEM medium containing 0.68 μM rapamycin/DMSO, or indicated concentration of RAD001/DMSO, every other day for up to 50 days. Control cells were treated with vehicle (DMSO) in MEM medium. Rapamycin (Sirolimus) was purchased from Sigma, and RAD001 (Everolimus) was obtained from Selleck.

4.5.2. Immunofluorescence staining

For immunofluorescence, cells were seeded in 4-well chamber slides. After fixation in 4% paraformaldehyde/PBS at room temperature for 15 min, cells were permeabilized with 0.5% Triton X-100/PBS at room temperature for 5 min, followed by an overnight incubation in the blocking solution (4% BSA/TBS) at 4 °C. Cells were then stained with primary antibodies for 3 hours at room temperature. The primary antibodies used in this study were: a rabbit polyclonal antibody against progerin (custom peptide antibody, Yenzym); a goat anti-lamin A/C antibody (N-18, Santa Cruz); and a mouse anti-lamin A/C antibody (MAB3211, Chemicon). After primary antibody incubation, primary antibodies were detected with Alexa Fluor-labeled secondary antibodies (Invitrogen). Slides were mounted with Vectashield mounting medium containing DAPI and observed with a Zeiss fluorescence microscope. Images were taken using a 40x objective (about 100 nuclei per condition). Exposure times and acquisition settings were established at the beginning of each set of experiments and kept constant for all treatments.

4.5.3. Extraction of nuclear boundaries

A Matlab program was used to extract nuclei boundaries. In order to reduce image histogram variability both between and within images, we first used contrast-limited adaptive histogram equalization. An 8×8 grid of tiles, a clip limit of 0.02, and a Rayleigh distribution were employed. Next, we binarized the images using Matlab's built-in thresholding function, which uses Otsu's method. Holes within bright regions were then filled, and regions that either overlapped the image boundary or were smaller than 800 pixels were removed. In order to smooth and enlarge the regions, which correspond to nuclei, the images were morphologically eroded with a disk of radius 3 pixels and then morphologically dilated with a disk of radius 6 pixels. The convex hulls of these smoothed and enlarged regions were next calculated. These outer convex hulls were later used as an outer limit on the nuclei boundary positions. Next, the images were morphologically eroded with a disk of radius 2 pixels. The convex hulls of these smoothed and slightly enlarged regions were used to initialize an active-contour-based boundary extraction algorithm.

We next processed the original images for use by the active-contour-based boundary extraction algorithm. First, the brightness and contrast of the image was adjusted so that 1% of the pixels was saturated at the lowest intensity and 1% was saturated at the highest intensity. For each nucleus, any pixel outside of its outer convex hull, which was found as described above, was set to zero, and the brightness and contrast were again adjusted as before. We next calculated the binarization threshold using Matlab's built-in thresholding function, but did not binarize the image. Instead, we nearly binarized the image by setting any pixel whose value was

less than 70% of the threshold value to the lowest intensity and any pixel whose value was greater than 130% of the threshold value to the highest intensity. The remaining, non-saturated pixel intensities were then stretched to fill the entire intensity range. The holes in this gray-scale, nucleus image were next filled.

An active contour, or snake algorithm, was used to extract nuclei boundaries with sub-pixel resolution, as described in Xu and Prince (86). The gradient vector flow (GVF) field of the processed, nucleus image was calculated. The inner convex hull of the nucleus, found as described above, was next interpolated and used as the initial position of the active contour. The contour, which is a polygon, was then repeatedly deformed 75 times and interpolated until the change in area from one set of deformations to the next was no more than 10 square pixels. Contours were not allowed to deform more than 50,025 times. The GVF, snake interpolation and snake deformation functions are from Xu and Prince (86). (The following parameters were supplied to these three functions: number of GVF iterations, 80; d_{min}, 0.5; d_{max}, 2; tension or alpha, 0.02; rigidity or beta, 0.05; step size or gamma, 1; external force or kappa, 0.6.) The contour was interpolated a final time, resulting in an outputted polygon with sides of constant length (d_{min}).

Some contours do not correspond to single nuclei, but rather are multiple, overlapped nuclei or are auto-fluorescent regions of cells. The user is next given an opportunity to remove such unwanted contours. Each analyzed image is sequentially displayed and polygons clicked on by the user are removed from further analysis.

4.5.4. Analysis of boundary shape

We calculated the boundary curvature at each boundary point by fitting a circle to that boundary point and the two points 25 boundary points away from it. The curvature was then calculated as the reciprocal of the radius of that circle. Convex curvatures were kept positive, while concave curvatures were made negative. For each nucleus, the boundary point farthest from the centroid was labeled boundary point 0. When visualized with color, curvature values were cut off such that magnitudes above a cut-off value were set to that cut-off value. For each nucleus, the number of invaginations was calculated by counting the number of boundary regions, of any length, where negative curvature was uninterrupted by positive curvature, and eccentricity was defined as the eccentricity of an ellipse with the same second-moments as the nuclear shape. The eccentricity of an ellipse describes its elongation; a circle has an eccentricity of 0, and a line segment has an eccentricity of 1.

4.5.5. WST-1 cell proliferation assay

A WST-1 cell proliferation assay (Roche) was used to analyze the effects of RAD001 on cellular growth. An HGPS cell line HGADFN167 p12 and a control cell line HGADFN168 p14 were seeded in separate standard 24-well plates at 10,000 cells in 500 µl fibroblast medium per well. Wells were treated with 0, 20, 60, 100 and 500 nM RAD001/DMSO in triplicate and the solvent controlled at 0.1% for all wells. The cells were then incubated with treatment for 72 hours. The medium was removed from each well and 500 µl of 10% WST-1 reagent in fibroblast medium was applied to each well following the incubation. Three blanks, consisting of 500 µl of 10% WST-1 reagent in fibroblast medium, were also created. The absorbance (450nm) of

each well was read after 3 more hours of incubation using a SpectraMax M5^e plate reader (Molecular Devices), and the average absorbance of the blanks was subtracted from each measurement.

Cell numbers were calculated from the absorbance values using a standard curve established by repeating the experiment without treatment and seeding at 1000, 2000, 4000, 8000 and 16000 cells per well in duplicate. The percent survival was calculated for each sample by the equation: percent survival = (cell #)/(average cell # of 0 nM treatment), then averaged by treatment. The error was calculated using the standard deviation of the percent survivals of the 3 samples for each treatment.

Chapter 5. Cellular contact guidance via dynamic sensing of nanotopography

This chapter is adapted from Driscoll, Sun, Guven, Fourkas, and Losert (Submitted). Meghan Driscoll performed the experiments and analyzed that data. Xiaoyu Sun fabricated the ridges, and Can Guven modeled the interaction of the cells with the ridges.

5.1. Overview

We investigate the shape dynamics of the amoeba *Dictyostelium discoideum* on nano-topographical gratings. Multiple studies have previously implicated the patterning of focal adhesion complexes (FACs) in contact guidance. However, we observe significant contact guidance of *D. discoideum* along ridge-shaped and groove-shaped nano- and microtopographic surface features, even though *D. discoideum* lacks FACs. We find that cells that move parallel to ridges are faster, more protrusive at their fronts, and more elongated than cells that move perpendicular to ridges. Quantification of contact guidance efficiency shows that ridges with a spacing of about 1.5 μm lead to the greatest contact guidance efficiency. Because *D. discoideum* cells exhibit oscillatory shape dynamics, we model contact guidance on nanogratings in terms of stochastic cellular harmonic oscillators that couple to the periodicity of the ridges. The spatial and temporal scales of the oscillations that best

couple to the surface are consistent with those of protrusive dynamics. Our results suggest that the coupling of protrusive dynamics, which are governed by actin dynamics, to surface topography is one possible mechanism for contact guidance.

5.2. Background

In Chapter 2, we analyzed the shape dynamics of amoebae migrating on flat surfaces, while in Chapter 3, we analyzed the shape dynamics of suspended amoebae. In this chapter, we analyze the shape dynamics of amoebae migrating on nanogratings of short parallel ridges.

Cells can adjust their migration behavior based on the local shape of the surface on which they move (135). This process, termed contact guidance, is well established but poorly understood. One challenge in quantifying contact guidance is that the natural surface topography encountered by cells spans a wide range of distance scales. Features of the surface topography range from the microscopic (e.g., the diameter of collagen fibers) to the nanoscopic (e.g., individual collagen fibrils or molecules). In addition, cells couple to surfaces through both specific, integrin-mediated complexes and non-specific adhesion.

There are many reported examples of micro- and nano-scale surface patterns promoting contact guidance and triggering changes in cell morphology (39-47). 70-nm silica spheres attached to a substrate lead to striking changes in the actin scaffolding of osteoblasts (44). Above a critical density, nanoparticles coated on surfaces lead to the formation of filopodia and a loss of stress fibers (44). Grooves as shallow as 35 nm can lead to cell alignment in fibroblasts (39). Nanopatterned surfaces can affect focal adhesion complexes in fibroblasts (42, 46). Compared to

fibroblasts growing on flat surfaces, fibroblasts growing on nanocolumns have more filopodia and fewer actin stress fibers, which is consistent with being in a more motile state (41, 43).

Recent studies have shown that FACs (74, 75), which are structures that involve dozens (if not hundreds) of proteins (136), can organize with a preferred orientation in the presence of surface nanotopography. Actin stress fibers, which connect FACs, have also been observed to align with surface topography (72). However, many fast moving cells migrate without mature FACs, relying instead on the simpler dynamics of actin polymerization (i.e., protrusions and retractions) coupled with non-specific surface adhesion (137, 138). Furthermore, metastatic cancer cells can revert back to this more primitive amoeboid style of migration. Recently, T cells were observed to migrate parallel to nanogrooves even without integrin-mediated adhesion (48). While there is an anecdotal report that the amoeboid *D. discoideum* can sense and align with small grooves on agar (139), the contact guidance of amoeboid migration has yet to be quantified or even studied systematically.

Two proposed mechanisms for contact guidance have received significant attention (1, 49, 140): patterning of focal adhesions and preferential actin polymerization (mainly through filopodia). While focal adhesion patterning is often observed, it is not clear whether this patterning causes or is a consequence of contact guidance. Filopodia have been reported to assist cells in sensing their environment (141). Fibroblasts on nanocolumns have more filopodia per μm of perimeter than do

cells on flat surfaces (41), and it has been suggested that filopodia are more likely to form parallel to ridges than perpendicular to them (73).

Although both FAC patterning and filopodial sensing are plausible mechanisms for contact guidance, the evidence supporting either mechanism is limited. Fujita *et al*. (72) found no correlation between filopodial orientation and ridge orientation. Based on this observation, they suggested that protrusion dynamics are essential to contact guidance. In support of this hypothesis, they found evidence that suggested that mesenchymal stem cell protrusions that are not directed along ridges are retracted more quickly than other protrusions.

To gain deeper insights into nanotopographic contact guidance, here we present studies of this phenomenon in the social amoeba *Dictyostelium discoideum. D. discoideum* is commonly accepted as a model system for amoeboid motility. *Dicty* is genetically tractable and bears a strong similarity to neutrophils in its fast motion and in its ability to detect and follow shallow chemical gradients (chemotaxis) (50). Specifically, the key components of the gradient-sensing pathway, the actin polymerization machinery that generates leading edge protrusion and the acto-myosin machinery that generates cell contractions, are conserved between *D. discoideum* and neutrophils (50).

D. discoideum cells undergo chemotaxis in response to a cyclic adenosine monophosphate (cAMP) gradient. Wildtype *D. discoideum* cells self-aggregate by releasing cAMP as a directional cue. To avoid introduction of such chemical directional cues, we use mutant cell lines that lack ACA, the cyclase that produces cAMP. The statistics and dynamics of aca^- cell migration, including dynamic

changes in cell shape, have been extensively studied on flat surfaces (see Chapters 2, 3 and (91)).

Here, by analyzing nearly 2,000,000 cell shapes, we show that amoeboid cells can be directed effectively via surface contact guidance, even though they do not possess focal adhesion complexes. A detailed analysis of center-of-mass motion and shape dynamics allows us to estimate the characteristic length and time scales over which migrating cells respond to surface topography. The distance scale for this contact guidance response is comparable to that of protrusions. We outline a proposed mechanism for contact guidance by surface nanotopography that is based on protrusive dynamics.

5.3. Results

5.3.1. Amoeboid cells exhibit contact guidance even without FACs

One hypothesized mechanism for contact guidance is focal adhesion patterning. To test whether contact guidance is possible in the absence of FACs, we studied the migration of *D. discoideum* cells on ridged surfaces. Nanogratings composed of parallel ridges were fabricated using multiphoton absorption polymerization (142). The ridges had a width of ~250 nm, a height of a few hundred nm, and a constant spacing that ranged between 0.4 and 10 μm in different samples. Figure 5.1A shows a scanning electron micrograph (SEM) of one such nanograting with a spacing of 2 μm. To ensure the chemical uniformity of the surface, acrylic resin surfaces were replicated using polydimethylsiloxane (PDMS) molding (107). While *D. discoideum* are commonly studied migrating on glass, we have previously

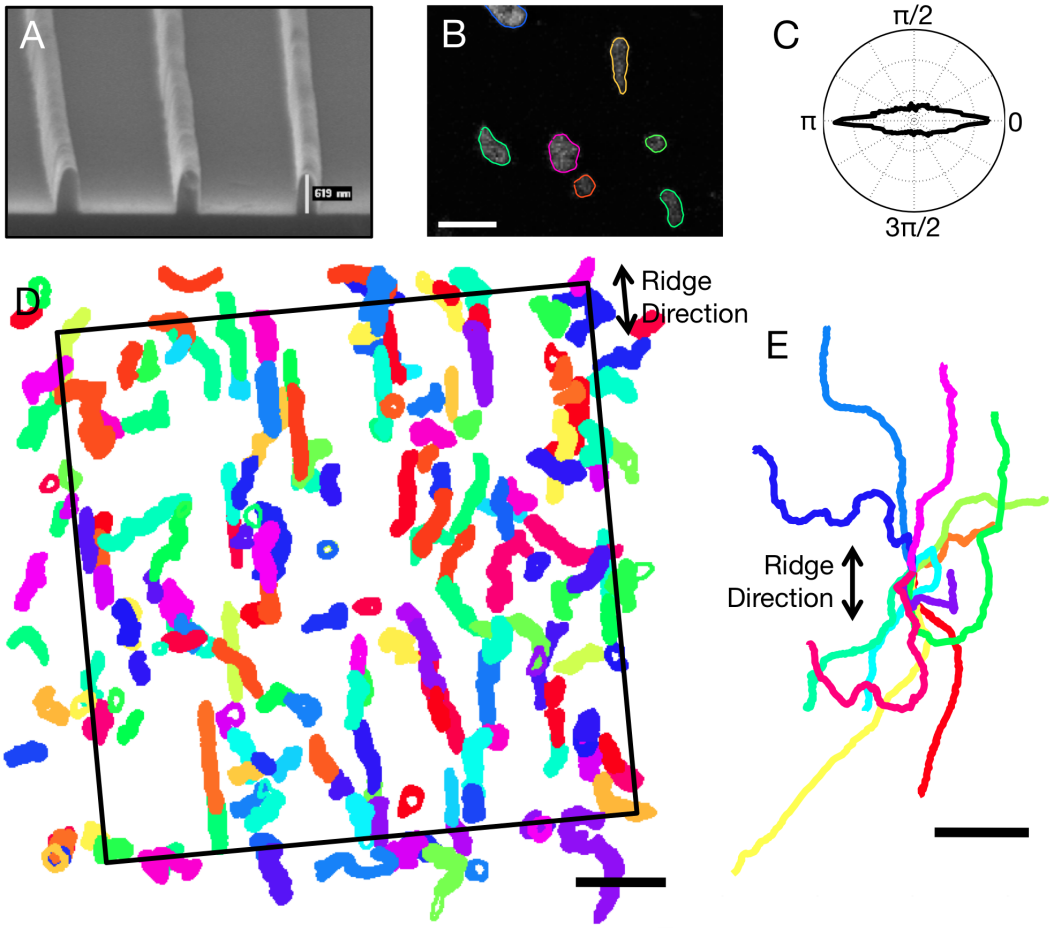

Figure 5.1. **The contact guidance of amoeboid cells on a nanograting of parallel ridges spaced 1.0 μm apart. (A) Nanogratings of parallel ridges. Shown is an SEM image of several ridges. Each ridge has a height of a few hundred μm and a width of ~250 μm. (B) Cytoplasmically dyed *D. discoideum* amoebae migrating on a nanograting. The extracted shape of each cell is overlaid. The scale bar is 20 μm. (C) Polar plot of velocity direction weighted by speed. From this plot it is apparent that cells migrate preferentially parallel to the ridges. 0 and π indicate motion parallel to ridges, while π/2 and 3π/2 indicate perpendicular motion. (D) The overlapped, extracted cell shapes over 22 minutes, or 335 frames. The scale bar is 50 μm. (E) The centroid motion of 12 cells over 10 minutes. All tracks were forced to begin at the graph's origin. The scale bar is 20 μm.**

shown that *D. discoideum* migrate with equal speed on acrylic surfaces (108). *Aca*- cells (in an AX3 background) were prepared, cytoplasmically dyed, and imaged as described in Section 5.5.2. Unlike wildtype *D. discoideum*, *aca*- cells do not communicate with each other by releasing cAMP. Thus, in the absence of an imposed external signal, the direction of motion of *aca*- cells is random. Cell centers and shapes were tracked using custom-written software. Figure 5.1B shows an example fluorescence image with overlaid cell shapes of cells migrating on 1.5 μm spaced ridges. Figure 5.1D shows all of the extracted cell shapes from a 10 minute, 150 frame image sequence from the same experiment. A spider plot of the tracks of 12 randomly chosen cells migrating over 10 minutes is shown in Figure 5.1E. It is clear from the spider and shape plots that cells prefer to orient and migrate parallel to the ridges. Focal adhesion complexes are thus not necessary for contact guidance in amoeboid cells.

To measure how contact guidance depends on ridge spacing, we used several different metrics. First, we examined both the cell velocity and the alignment of the cell shape as a function of angle with respect to the ridges. (We define the alignment of the cell shape as the orientation of the ellipse that best fits the cell shape.) We found that cells prefer to align and to migrate parallel to ridges. However, not all cells move at all times, and a nearly round, stationary cell contributes as much to histograms of the direction of alignment or the direction of migration as does a well-polarized (elongated), fast-moving cell. To compensate for this effect, we weighted the direction of the velocity by its magnitude and the cell alignment by the cell's eccentricity. Figure 5.1C shows a polar histogram of weighted velocity for the

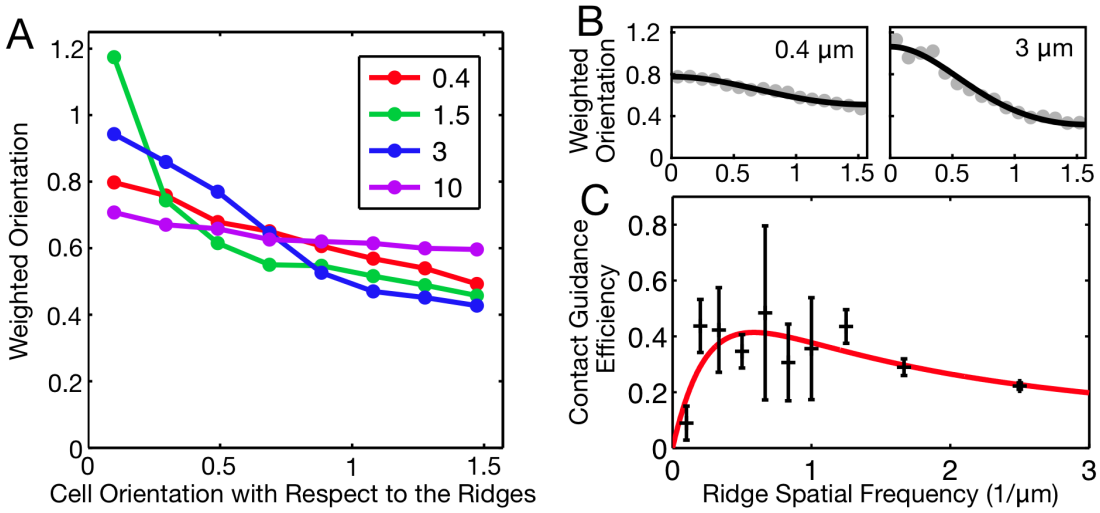

Figure 5.2. **Cells migrating on nanogratings with a ridge spacing of 1.5 μm exhibit greater contact guidance than do cells migrating on surfaces with smaller or larger ridge spacings. (A) The orientation, weighted by eccentricity, of cells migrating on nanogratings with ridge spacings of 0.4 μm, 1.5 μm, 3 μm, and 10 μm. The weighted orientation for each ridge spacing includes data from two or three experiments. (B) To measure the surface contact guidance efficiency, weighted orientations from individual experiments were fit to a stochastic model of cell guidance. Two such fits are shown here. (C) The surface contact guidance efficiencies of various nanogratings are shown in black, while the fit to the stochastic harmonic oscillator model is shown in red. Contact guidance is greatest on nanogratings with ridge spacings between 1.0 μm and 2.0 μm.**

experiment shown in Figure 5.1D. Here, 0 and π indicate motion parallel to the ridges, while π/2 and 3π/2 indicate motion perpendicular to the ridges. Figure 5.2A similarly shows orientation weighted by eccentricity for migration over nanogratings with various ridge spacings.

5.3.2. Contact guidance is affected by the ridge spacing

To assess how sensitively contact guidance depends on the underlying surface topography, we measured the contact guidance of cells migrating on nanogratings with a variety of ridge spacings. We fabricated 300 μm × 300 μm nanogratings with ridge spacings of 0.4, 0.6, 0.8, 1.0, 1.2, 1.5, 2, 3, 5, and 10 μm. Figure 5.2a shows the distributions of cell orientations (weighted by eccentricity) for several of these nanogratings. We found that the larger ridge spacings induced little contact guidance. Cells are, on average, 10 to 20 μm long and 5 μm wide. Thus, given the small number of ridges in contact with any cell, reduced contact guidance is expected on the nanogratings with the largest ridge spacings. We also found that the smaller ridge spacings induced little contact guidance.

We fit the weighted orientations to a stochastic model of the dynamics of cell orientation (143). Cells do not achieve perfect transduction of the signal from the ridges into a response that orients them parallel to the ridges. This imperfect relationship between the signal and the response was introduced into the model via a noise term, $\xi(t)$, with amplitude q. The dynamics of θ, the angle between the cell orientation and the ridge orientation, are described by the stochastic differential equation.

$$d\theta/dt + p \sin(2\theta) = \xi(t). \tag{5.1}$$

Here, p is the turning rate of the cell to the ridge direction. The Fokker-Planck equation corresponding to the Langevin equation shown in Equation 5.1 yields the evolution of the probability density function of θ. The steady-state solution, which depends only on p/q, matches our observations of the weighted orientations shown in

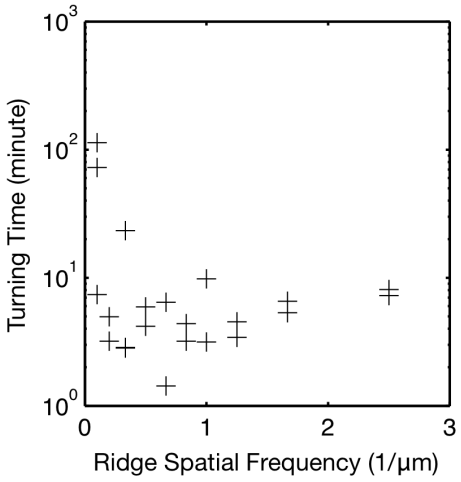

Figure 5.3. **The turning times of amoebae on variously spaced ridges. The turning times are of the same order of magnitude as the persistence time of *D. discoideum* on a flat surface.**

Figure 5.2A. Two fits to the steady-state solution are shown in Figure 5.2B. We find that p/q, the surface contact guidance efficiency, is greatest for ridge spacings of 1.0 μm to 2.0 μm (see Figure 5.2C). We estimated the noise amplitude, q, from observations of cells on flat surfaces. We found the turning times in the direction of the signal for different ridge spacings, under the assumption that this noise level does not depend on the signal (Figure 5.3). The turning times are of the same order of magnitude as the persistence time of *D. discoideum* on a flat surface (66). The persistence time is the time-scale over which the cell moves roughly straight.

The measured contact guidance efficiency of a given ridge spacing can vary greatly from experiment to experiment (see Figure 5.2C). We therefore measured the contact guidance of four different ridge spacings (0.4, 0.8, 1.5, and 5 μm) and a flat control in a single experiment. Comparing the four ridge spacings, we found that 1.5

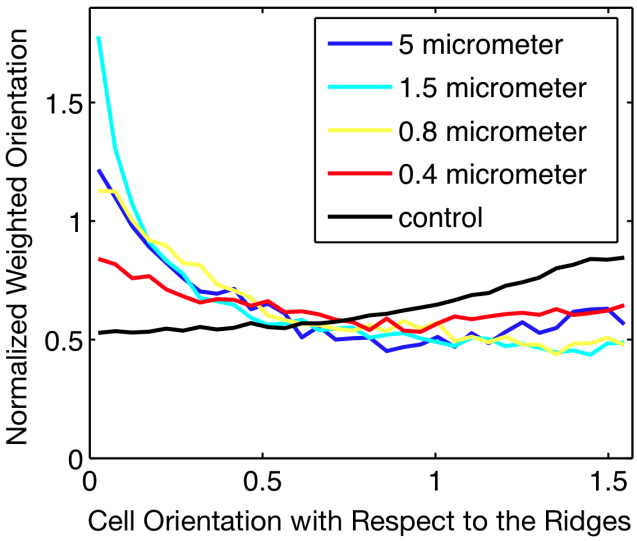

Figure 5.4. **The normalized weighted orientation of amoebae migrating on ridges with four different spacings: 0.4, 0.8, 1.5, and 5 μm. Cells on different ridge spacings were imaged at the same time and were on the same coverslip. Ridges spaced 1.5 μm apart guide cells better than do ridges spaced closer together or further apart.**

μm spaced ridges guided cells best, while 0.4 μm spaced ridges guided cells worst (see Figure 5.4). The peak in contact guidance efficiency around 1.5 μm is consistent with the experiments we performed with single nanogratings.

To explore the effect of ridge width on contact guidance, we fabricated grooves ("negative" ridges) by making a second PDMS mold of the original PDMS mold and using this second PDMS mold to fabricate grooves. We found that the surface contact guidance efficiencies of grooves with 2 μm and 10 μm spacings (~550 nm wide each) are similar to the efficiencies of ridges with the same spacings. Ridge width therefore does not seem to have a significant effect on contact guidance efficiency.

We also explored the effect of overall ridge size on contact guidance. We fabricated ridges with heights and widths of a few micrometers. We found that such large ridges can induce behavior other than simple contact-mediated guidance. For instance, cells sometimes swing off of large ridges, a behavior similar to that observed at the edges of tall cliffs (see Chapter 3).

5.3.3. Cells migrating on ridges have wave-like shape dynamics

We have previously observed wave-like shape dynamics in both adhered cells migrating on a flat surface and swimming cells (see Chapter 3). Protrusions (i.e., bumps of high curvature) travel from the fronts to the backs of these cells. We found that cells migrating on ridges have similar wave-like shape dynamics. Figure 5.5A shows the shape of a cell that is moving roughly parallel to the ridges, while Figure 5.5B shows the distance from the centroid of the cell shape to each boundary point as a function of arc length and time. From this figure and similar data for other cells, we found that cell length oscillates. Cell shape, however, oscillates not only globally, but also locally. Figure 5.5D shows the protrusive (red) and retractive (blue) motion of the cell, while Figure 5.5C shows the cell's boundary curvature. In the curvature plot, dark red corresponds to regions of high boundary curvature. The slanted red lines indicate that there are regions of high curvature that travel from the cell front to the cell back. The initiation of regions of high curvature corresponds to protrusions (see Chapter 3). Even though this cell is migrating on ridges, it still extends protrusions regularly. Since the curvature bumps travel along roughly alternate sides of the cell, the cell also still zig-zags by extending protrusions in a left-right-left-right manner.

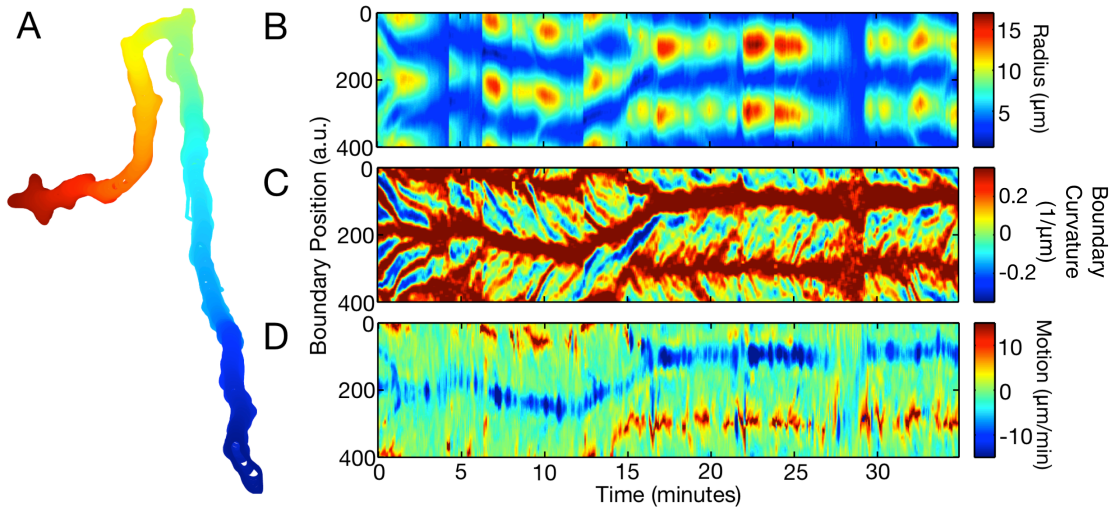

Figure 5.5. **Cells have oscillatory shape dynamics. (A) The shape of a cell migrating on ridges with a spacing of 0.4 μm. The long stretches of straight motion and the two right-angle turns perpendicular to the ridges are not typically observed when *D. discoideum* migrate on flat surfaces. The shape dynamics of this cell are represented in panels B and C. (B) Cell elongation is oscillatory. Here, the color represents the distance from each boundary point to the centroid. Elongated shapes are shown as red and blue, while more circular shapes are green. (C) Local shape dynamics are also oscillatory. In this plot of boundary curvature, red represents regions of large positive boundary curvature and blue represents regions of large negative curvature. Regions of high curvature travel from the front to the back of the cell. (D) The local boundary motion of the cell. Red represents protrusive motion and blue represents retractive motion.**

The shape dynamics of cells on ridges are therefore oscillatory and resemble the shape dynamics of cells migrating on a flat surface.

5.3.4. Could contact guidance result from wave-like protrusive motion?

Cell migration results from the interaction of protrusions and retractions with the surface. *D. discoideum* cells extend protrusions first outward and then downward, such that most protrusions do not initially interact with the surface (16). Protrusive waves are visible not only in the shape of the cell but also in the cell's adhesion area with the surface (see Chapter 3). Cells migrating on ridges have oscillatory shape and surface adhesion dynamics. To explore the hypothesis that the interaction between cellular oscillations and the nanograting plays a role in contact guidance, we developed a simple model of contact guidance. We modeled cellular oscillations as harmonic oscillators, which have previously been used to model cell migration (66). The cellular oscillations are described by characteristic properties that include the natural frequency ω_0 and the damping coefficient β. The interaction between the cells and the surface is noisy, as it involves stochastic chemical reactions and external fluctuations. Therefore, we let the signal from the nanograting, $F(t)$, be a stochastic cue that mimics a random square-wave signal. $F(t)$ has amplitude a and a correlation time L/v_0, where L is the ridge spacing and v_0 is a normalization constant with units of speed.

The dynamics of the stochastically driven oscillations, X, are described by the damped harmonic oscillator equation

$$d^2X/dt^2 + \beta\, dX/dt + \omega_0^2\, X = F(t). \qquad (5.2)$$

The average power, $<P>$, delivered to this system by the driving signal can be thought of as a measure of surface contact guidance efficiency. In the steady state, the normalized average power delivered to this system is (144)

$$<P>/(a'v_0) = a' L/ (1 + L \beta' + (L \omega_0')^2) \quad (5.3)$$

where $\beta' = \beta/v_0$, $\omega_0' = \omega_0/v_0$, $a' = a/v_0^2$. Fitting the normalized averaged power (Equation 5.3) to the contact guidance efficiencies derived from the data, we found length and time scales that characterize the cell's interaction with the nanograting. These three scales roughly correspond to the length scale of spatial resonance (the peak position in the plot), a damping length scale (the width of the peak), and the signal strength (the height of the peak). The contact guidance efficiencies and the fit are shown in Figure 5.2C. We found a resonance in the interaction of the cellular oscillations with the nanograting at $1/\omega_0' = 1.7$ μm, which is roughly the size of protrusions (see Chapter 3) and actin waves (19). To interpret the remaining parameters extracted via the model, we set $v_0 = 10$ μm/min. This speed is the average speed of the cells (91), the speed of protrusions relative to the cell (see Chapter 3), and the speed of actin waves (19). From the fit, we found a damping coefficient of $1/\beta' = 1.6$ μm, which leads to an oscillation decay time of $2v_0/\beta' = 18$ sec, roughly the duration of protrusions (16, 69). The amplitude of the signal received by the cell is $1/a' = 1.4$ μm. Using v_0, we can also interpret the spatial resonance scale, 1.7 μm, as a time-scale. The mean sensing time is the frequency at which the intrinsic cellular oscillations sense the up-down symmetry of the ridges via the stochastic signal. This time is calculated as $\lambda^{-1} = 2/\omega_s = 2/(\omega_0'v_0) = 20$ sec, which is the frequency of protrusions (see Chapter 2 and (68, 69)).

Protrusions result primarily from actin dynamics. To elucidate the role of actin in contact guidance, we treated cells with latrunculin, which depolymerizes actin, and then observed their shapes on ridges. On glass, latrunculin-treated cells are

round. If contact guidance were a passive mechanism independent of actin polymerization, we would expect latrunculin-treated cells on ridges to elongate in the ridge direction. We observed that latrunculin-treated cells on ridges are also round, suggesting that contact guidance requires actin polymerization. We next investigated whether myosin II contractility was required for contact guidance in *D. discoideum*. We found that *myoII-* and *aca-* cells have similar surface contact efficiencies, and so are guided similarly.

5.3.5. Shape dynamics of cells on ridges

We have shown that cells migrate and align parallel to the ridges in nanogratings. In what way are cells directed by nanogratings? One possibility is that more cells move parallel to ridges than perpendicular to them. Another possibility is that cells move faster parallel to ridges than perpendicular to ridges. To investigate these possibilities, we measured how cell speed and eccentricity are related to contact guidance. Figure 5.6A shows histograms of velocity direction, weighted by speed, as a function of both velocity direction with respect to ridge direction and speed. The cells with the lowest speed (shown in red) exhibit little preferential migration. As average cell speed increases, a smooth transition to contact guidance is seen. Similar behavior holds for cell orientation. Figure 5.6B shows histograms of cell orientation, weighted by eccentricity, as a function of both cell orientation with respect to ridge direction and eccentricity. We found that, in analogy to our observations of increased contact guidance with increasing speed, the most circular cells show no preferential contact guidance, while the most elongated cells show the greatest alignment with the

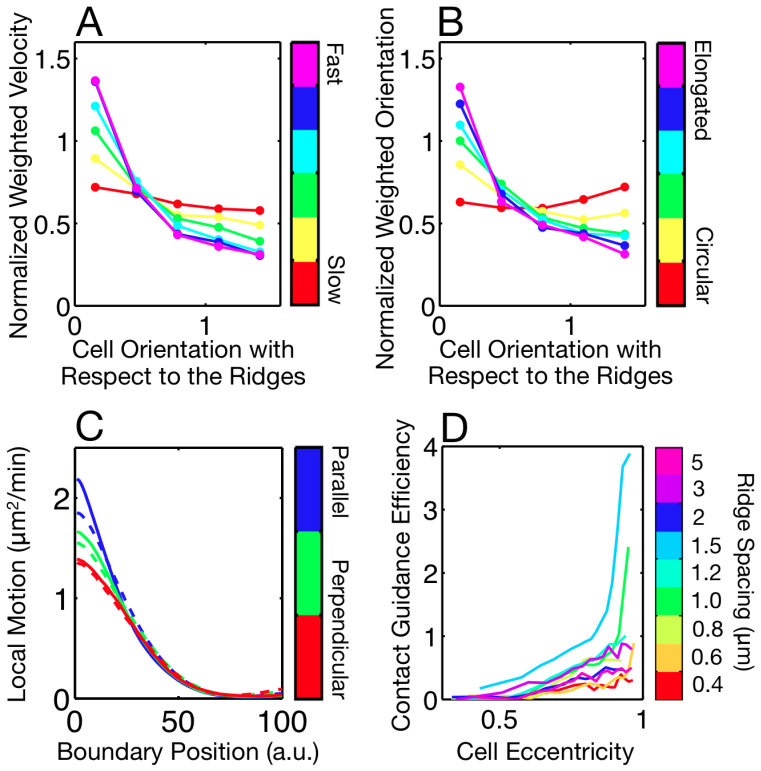

Figure 5.6. **Contact guidance is related to cell speed, eccentricity and the spatial patterning of protrusions and retractions along the cell boundary. (A) Distributions of velocity direction, weighted by speed, with respect to the ridge direction for cells moving on 1.2 μm spaced ridges. The red line represents the weighted velocity for the slowest sixth of cells and the purple line the weighted velocity for the fastest sixth of cells. Faster cells are more likely to move parallel to the ridges than are slower cells. (B) Distributions of orientation, weighted by eccentricity, with respect to the ridge direction. The cells were ranked by eccentricity and then binned. The more elongated cells are more likely to be oriented parallel to the ridges than the more circular cells. (C) The surface contact guidance efficiency as a function of cell eccentricity. One experiment is shown for each ridge spacing. (D) Protrusive and retractive motion as a function of arc length (x-axis) and orientation with respect to the ridges (color). For protrusions, shown as solid lines, the boundary position zero represents the cell front. For retractions, shown as dashed lines, the boundary position zero represents the back.**

ridges. We determined the contact guidance efficiencies of the weighted orientations as a function of eccentricity. Figure 5.6C shows the contact guidance as a function of eccentricity for experiments at various ridge spacings. While for all ridge spacings the contact guidance increases with increasing eccentricity, the contact guidance increases fastest at ridge spacings near 1.5 μm.

Cells migrate and change shape by protruding and retracting. Since ridges couple to the overall speed and eccentricity of cells, we expect the ridges to couple to the underlying dynamics of protrusions and retractions. We measured how the protrusive and retractive motion along the boundary was affected by cell orientation with respect to the ridges. Figure 5.6D shows protrusive and retractive motion along the cell boundary for various cellular orientations. For the protrusive motion plots in this figure, which are shown as solid lines, 0 (a.u.) is the cell front and 100 is the cell back. For retractive motion plots, which are shown as dashed lines, 0 is the cell back and 100 is the cell front. In general, we found that cells oriented parallel to ridges show greater protrusive and retractive motion than do cells oriented perpendicular to ridges. Cells aligned parallel to ridges also have protrusive and retractive areas with a more narrow shape. The cell orientation with respect to the ridge direction does not significantly affect retractive motion near the front of the cell.

Cells that are parallel to ridges migrate faster, are more elongated, and are more protrusive than cells that are perpendicular to ridges. Cell speed and protrusive motion are necessarily related, and we have previously shown that cell speed and eccentricity are correlated (6). We can also compare protrusive/retractive motion and eccentricity. Figure 5.7A shows the protrusive and retractive motion, binned by

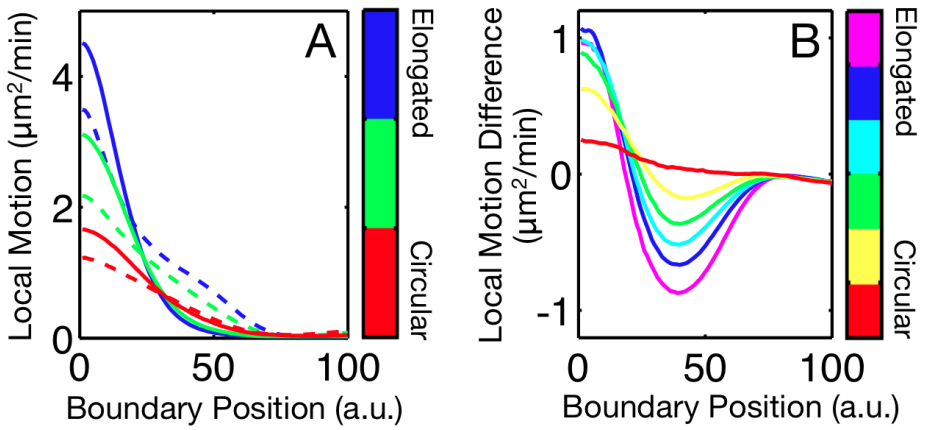

Figure 5.7. **Eccentricity and the balance of protrusions and retractions. (A) Protrusive and retractive motion as a function of arc length (x-axis) and eccentricity (color). (B) The spatial balance of protrusions and retractions. This plot is the difference between the solid lines, protrusive motion, and dashed lines, retractive motion, in A.**

eccentricity, of cells migrating on a flat acrylate film. Since Figures 5.6D and 5.7A are similar, eccentricity and cell orientation with respect to the ridges seem to be related to protrusive/retractive motion in a similar manner.

We also found that cell speed is related to the spatial patterning of protrusions and retractions. For each experiment, we determined the average location along the cell boundary (measured from the cell front) at which protrusive and retractive motion are equal. We found that this location is inversely correlated to the average cell speed. Faster-moving ensembles of cells then tend to have more narrow regions of protrusive motion than do slower moving cells. The relative widths of protrusive and retractive motion affect the overall balance of protrusions and retractions. Slower-moving cells are more retractive at the back than they are protrusive at the front and are more retractive at the front than they are protrusive at the back, but are more protrusive than retractive at their sides. Faster-moving cells are more protrusive

at the front than they are retractive at the back, but are more retractive at the sides than they are protrusive. The protrusive/retractive balance for fast-moving cells is shown in Figure 5.7B. (This plot was generated by subtracting the solid lines from the dashed lines in Figure 5.7A.) Contact guidance is thus related to cell speed, eccentricity, and protrusive/retractive motion.

5.4. Discussion

Focal adhesion patterning is one hypothesized mechanism for contact guidance. However, we have shown that the amoeba *Dictyostelium discoideum,* which does not have focal adhesions, exhibits contact guidance. What other mechanisms could play a role in amoeboid contact guidance? Based on our observations and model we propose that amoebae can sense surface topography dynamically at the length and time scales of internal actin dynamics. An interaction between actin dynamics and surface topography could allow cells to recognize and be guided by topographical features on the micrometer scale. This distance scale is much larger than both FACs and the macromolecular ensembles typically associated with focal–adhesion-based contact guidance. Thus, dynamic contact guidance is potentially important even for cells that have focal adhesions, since multiple mechanisms might play a role in contact guidance on multiple length scales.

We suggest that two dynamic actin processes could be responsible for contact guidance: filopodial dynamics and actin wave dynamics. Our data are consistent with a model in which contact guidance arises from wave interference between cellular oscillations and surface features. Nanogratings with ridges spaced between 1 μm and 2.0 μm apart show the greatest contact guidance, while gratings with ridges spaced

farther apart or closer together show reduced guidance. This preferred length scale is much larger than the scale of proteins or protein clusters, but is comparable to the characteristic size of certain oscillatory actin features, such as actin waves and filopodia. In *D. discoideum*, the full-width at half-maximum size of actin waves is ~1 μm (19), and protrusions are ~1.5 μm wide as measured from both the cell shape and the cell footprint. Filopodia extend dynamically to lengths of 1-3 μm (145). From our contact guidance model, we also extract an oscillation wavelength of 1.7 μm and a time scale of 20 sec. A similar time scale can be seen in dynamic, actin-based protrusions, since cells generate new protrusions roughly every 20 seconds (see Chapter 3). The correspondence between our model and the spatial and temporal scales of actin dynamics provides support for the hypothesis that actin dynamics are involved in sensing and responding to surface topography. Interaction with surfaces is known to affect actin waves, which is an important prerequisite for contact guidance by surface topography. For example, actin waves that interact with an obstacle have been shown to dissipate (20).

Finally, we note that the proposed mechanism is similar to newly emerging models of chemically guided motion, or chemotaxis. Recent studies have found that chemical signals of physiological strength do not usually generate protrusions in *Dictyostelium discoideum,* but instead bias the location of regularly occurring protrusions (68). Indeed, our measurements of shape dynamics indicate that the protrusive machinery operates similarly under multiple conditions: the dynamic shapes of cells directed by topography are similar to the dynamic shapes of cells migrating on a flat surface with or without a guiding chemical signal. Thus, we

anticipate that there exists an interesting competition between contact guidance and chemotactic guidance.

5.5. Materials and methods

5.5.1. Ridge fabrication

Sets of parallel ridges, each 300 μm long, were fabricated via MAP using a commercial Ti:sapphire laser (Coherent Mira 900 F). Each set of ridges covered an area of 300 by 300 μm^2 and had evenly spaced ridges 0.4, 0.6, 0.8, 1, 1.2, 1.5, 2, 3, 5 or 10 μm apart. The ridges were composed of an acrylic resin of 49 wt% tris(2-hydroxyethyl) isocyanurate triacrylate (SR368, Sartomer), 49 wt% ethoxylated(6) trimethylolpropane triacrylate (SR499, Sartomer) and 2 wt% Lucirin TPO-L (Ciba). The typical fabrication laser power was 13 mW as measured at the sample. The sample preparation and fabrication procedures have been described previously (146). To replicate ridges accurately, a composite PDMS mold consisting of a thin layer of hard PDMS with relief features and a thick slab of soft PDMS was prepared. First, 1.7 g of vinyl PDMS prepolymer (VDT-731, Gelest), 9 μl of Pt catalyst (SIP6831.2, Gelest), 0.05 g of modulator (87927, Sigma-Aldrich), 0.5 g of hydrosilane (HMS-301, Gelest) and 1 g of hexane were mixed. The mixture was then spin-coated (1000 rpm, 40 s) on the master substrate, allowed to sit for 2 h and baked at 60 °C for 1 h. The soft PDMS was prepared by mixing the prepolymer and curing agent (Sylgard 184, Dow Corning) in a 10:1 mass ratio. After degassing, the soft PDMS was poured onto the precured hard PDMS and baked at 60 °C for 1 h. When cured, the composite PDMS was peeled off the master substrate. Replicas of ridges were created by

placing a drop of acrylate resin between the mold and an acrylate-functionalized coverslip (see (146) for more details) and UV curing at 365 nm for 5 minutes. The PDMS mold for grooves was prepared using a double-molding process in which a ridge mold was treated as a master structure and a composite PDMS mold was made from it.

5.5.2. Cell preparation and imaging

D. discoideum cells, adenylyl cyclase A null and myosin II null cells (both in an AX3 background), were prepared as described previously in Chapter 2. All cells were cytoplasmically dyed with CellTracker Green CDMFA (Invitrogen), also as described in Chapter 2. Fluorescence images were obtained on a Leica TCS SP2 confocal microscope with a 40× objective every 4 seconds. To determine the location and angle of the ridges, we took reflection micrographs on the same microscope immediately after fluorescence imaging of the cells.

5.5.3. Boundary tracking

Cell shapes were extracted, tracked and analyzed using Matlab. The process of measuring the boundary is similar, though not identical to, that described in Section 4.5.3. First, a small amount (maximum of 1% of 255 for 8 byte images) of uniform noise was added to the images to facilitate subsequent thresholding; images with low background variance would otherwise threshold badly. Since the brightness of images varies across experiments, the images were next gamma corrected with a gamma of 0.6 to deemphasize brightness differences at high intensities. The images were then preprocessed to find the approximate boundaries of the cells. The

brightness and contrast of each image was adjusted until 1% of the pixels were saturated at low and high intensities. The images were again gamma corrected with a gamma of 0.4, since the intensities of dyed cells vary. Each image was next binarized using Matlab's built-in thresholder, which uses Otsu's method (147). Objects that were too small to be cells were removed, and any holes in objects were filled in. To smooth the objects, the images were next eroded by 2 pixels and then dilated by 2 pixels. Objects that touched the border were then removed, and objects that were too small to be cells were again removed. The convex hull, area, centroid position, and solidity of each object were calculated for later use. The convex hull of a shape is the smallest convex polygon that encloses that shape, while the solidity of a shape is the area of the shape divided by the area of its convex hull.

We next tracked the cells by using the processed, binarized images to find cells that overlapped from frame to frame. Since the cells move little from frame to frame, we expect a cell in a given frame to overlap with itself in the next frame. An object A in the current frame was tracked to an object B in the next frame if B was the only object in the next frame to overlap with A and if A was the only object in the current frame to overlap with B. If multiple objects in the current frame overlapped with the same object in the next frame, a new track was initiated for the object in the next frame and that track was marked as a clump of cells for later removal. Likewise, if multiple objects in the next frame overlapped with the same object in the current frame, then new tracks were initiated for the objects in the next frame and the track associated with the object in the current frame was marked as a clump. New tracks were initiated for objects that did not overlap with objects in the previous frame.

Tracked objects whose area changed by more than 70% or whose centroid moved by more than 11 pixels from frame to frame were split into two tracks. Finally, tracks that were marked as clumps or that had a duration of less than 20 frames were removed. Tracks that had a mean solidity of less than 0.5 or that had a mean area larger than a cell were also removed, since these tracks might be clumps of multiple cells.

The cell boundaries were next found to subpixel resolution using an active contour (snake) algorithm (86). First, the objects found via preprocessing were dilated by 3 pixels, and the convex hulls of the resultant objects were calculated. These large convex hulls were used as masks to select images of individual cells. Since the brightness of dyed cells varies, the brightness and contrast of the masked image of each cell was next adjusted until 1% of the pixels were saturated at low and high intensities. The binarization threshold was calculated using Otsu's method, but the image was not binarized. Instead, the image was nearly binarized by setting all pixel intensities below 0.7 times the binarization threshold to 0 and all pixel intensities above 1.1 times the threshold to 1. A gamma correction of 0.4 was also applied. After filling the holes in the grayscale image, we next calculated the image gradient. Then, using code described in (86), the gradient vector field was calculated. Again using code described in (86), we initialized an active contour with the convex hull of the approximate boundary, and then deformed the snake 40 times. We used the following snaking parameters: alpha (tension) 0.00002, beta (rigidity) 0.00005, gamma (step size) 1, kappa (external force weight) 0.6, dmin (minimum distance between boundary points) 0.5 pixels, and dmax (maximum distance between

boundary points) 1.5 pixels. We continued to deform the snake by 25 iterations at a time until it converged. Convergence was defined as an area change of 3 pixels or less over 25 snake iterations. Since objects that will later be removed, such as clumps of cells or cells that are too dim to snake effectively, take a disproportionate amount of time to snake, no more than 750 iterations were allowed beyond the initial 40 iterations. To achieve better boundary resolution, the snake was again deformed 25 times with dmin set to 0.25 pixels and dmax set to 0.75 pixels. The snaking parameters and the number of iterations allowed before checking were chosen so that the snakes would converge to the correct boundaries as quickly as possible. Each boundary, regardless of length, was finally interpolated to have 200 boundary points.

Tracked shapes were next automatically culled. Snaked shapes can become pinched if they snag on objects outside of the cell or if a region of a cell edge is dim. We therefore removed shapes in which boundary points that were 14 or more boundary points apart were less than 0.5 pixels away from one another. We also removed shapes that were smaller than a cell. When removing shapes, we split the shape's track into two tracks, the first of which ended in the frame before the removed shape and the second of which started in the frame after the removed shape. As before, we also removed tracks with durations less than 20 frames, with a mean solidity less than 0.5, or with a mean area larger than that of a cell.

Tracked shapes were next manually culled. The tracked shapes were checked in every 10^{th} frame, and selected tracks were removed 10 frames before and after the frame in which they were selected. The tracked shapes were then plotted on the

original fluorescence image, with each track a different color, to verify the boundary tracking (see Figure 5.1D).

The ridges cover only part of each image, so we filtered the tracks to analyze only cells on ridges. Using reflection micrographs of the ridges, a polygonal region of interest (ROI) was selected manually. Each shape in each frame was then annotated as entirely inside of the ROI, partially inside of the ROI, or entirely outside of the ROI. Only shapes that were entirely within the ROI were used for analysis.

5.5.4. Measuring contact guidance

A variety of measures were used to assess the extent of contact guidance. Cellular motion was first tracked and velocity calculated as described in (91). Cellular eccentricity and orientation were measured as the eccentricity and orientation of the ellipse that has the same second moments as the pixel positions of the binarized image of the tracked cells. Other measures of cell shape were calculated using boundaries extracted as described above. The curvature and shape measures shown in Figures 5.5B and C were calculated from these boundaries as described in Sections 2.3.1. and 2.5.5. respectively.

To fit the weighted orientations (see Figure 5.2A), we used a stochastic model for the dynamics of cell orientation (143). As shown in Equation 5.1, this model has a feedback mechanism that turns the cell towards the ridge alignment. The cell turning rate is described by p, which is a function of the topographical signal. The stochastic term, $\xi(t)$, models fluctuations in the cells' determination of the surface topography. The introduced noise, $\xi(t)$, is white (*i.e.*, $\langle\xi(t)\rangle = 0$). Its amplitude q, is given by the relation

$$<\xi(t)\xi(t')> = q\,\delta(t-t'), \tag{5.4}$$

where the brackets indicate an average over all cells and δ is the Dirac delta function. In our experiments we measure the probability density of the orientation angle $P(\theta)$, which is less noisy than the dynamics of the orientation angle. Therefore, instead of using Equation 5.1 directly, we consider the corresponding Fokker-Planck equation, which determines the time evolution of the probability density of the orientation angle $P(\theta,t)$,

$$\partial P(\theta,t)/\partial t = \partial/\partial\theta\,(p\,\sin 2\theta + (q/2)\,\partial/\partial\theta)\,P(\theta,t). \tag{5.5}$$

The steady state solution of this equation yields the observed probability density of the orientation angle,

$$P(\theta) = e^{p/q\,\cos 2\theta} / (2\pi\, I_0(p/q)), \tag{5.6}$$

where I_0 is the modified Bessel function of the first kind of order zero. We used the probability densities of the weighted orientations to find the fit parameter $\sigma = p/q$. For flat surfaces, which have topographical signals of zero, Equation 5.4 becomes an eigenvalue equation with solutions $(\lambda_k - k^2 q/2)\,A_k = 0$ (143). We approximate the characteristic time obtained from the angular correlations of cells moving on a flat surface to obtain a noise level via $<\cos\theta(t)\cos\theta(t')> = (e^{-|t-t'|\lambda_1})/2 = (e^{-|t-t'|q/2})/2$ (148). We assume that this noise level is roughly the same for cells migrating on ridges. From this noise level we approximate the turning times, shown in Figure 5.3, by $1/p = 1/(\sigma q)$.

5.5.5. Modeling contact guidance

As cells move, they interact with the underlying surface topography. Due to external and internal fluctuations, such as those in actin polymerization, cells sense the ridges as a stochastic signal. Since the ridges have vertical symmetry, we employ a dichotomous (two peaked) process to represent the signal that interacts with the cell. We used the ridge spacing L as the correlation length of the dichotomous process. We represent the signal perceived by the cell as a random variable F that can take values $\pm a$ with equal probability. In other words, the mean time between the up ($+a$) and down ($-a$) cues (i.e., the sensing time) is imposed by the periodicity of the structure. The vertical symmetry and the correlation between the cues imposed by the ridge structure correspond to the properties of the random variable, which are $\langle F \rangle = 0$ and $\langle F(t)F(t') \rangle = a^2 \exp(-v_0 |t-t'|/L)$, where the fit parameter v_0 is a normalization constant with the units of speed, and a is the amplitude of the signal. Furthermore, the time scale $L/v_0 = 1/\omega_s$ is associated with the mean time between sensing the ridge symmetry. In detail, the dichotomous process is the result of a Poisson process with the switch rate $\lambda = \omega_s/2$. The corresponding average sensing time between the oppositely oriented signals ($+a$ and $-a$) is $1/\lambda$.

Equation 5.2 can be rewritten by rescaling of the time variable via $y = v_0 t$.

$$d^2X/dy^2 + \beta' \, dX/dy + (\omega_0')^2 \, X = F'(y), \qquad (5.7)$$

where $\beta' = \beta/v_0$, $\omega_0' = \omega_0/v_0$, $F' = F/v_0^2$, $a' = a/v_0^2$ and $\omega_s' = \omega_s/v_0 = 1/L$. We fit the absorbed power (Equation 5.3) to the surface guidance efficiencies derived from the data and extract the rescaled quantities (i.e., damping, resonant frequency and amplitude) (see Figure 5.2C).

5.5.6. Measuring protrusive and retractive motion

Protrusive and retractive motion were measured by first finding the front and back of each cell. In each frame, the cell orientation was calculated as the orientation of the ellipse that has the same second moments as the pixel positions of the pixels within the cell boundary. Next, the angle of each boundary point relative to the center of the cell was calculated. The two boundary points closest to the cell orientation and the cell orientation plus π were then defined as the front and the back. The local motion measure, which was described in Section 2.5.4., is a measure of protrusive/retractive motion. The cell front was then distinguished from the back by finding the mean value of the local motion measure in the quarter of the cell boundary surrounding each of the two points. The boundary point in the more protrusive region was defined as the front of the cell, while the other boundary point was defined as the back.

The local motion measure connects each boundary point in a frame to a boundary point in the frame 12 seconds later. While the connection vectors do not cross, the mapping is not 1:1. We measured the differential protrusive and retractive area change along the boundary by tiling the regions between the boundary in each frame and the boundary in the frame 12 seconds later (see Figure 5.8). Each connection vector was associated with the area closest to it. Next, the boundary points were aligned such that the front was at boundary point 0 in every frame. The average protrusive and retractive areas were found as a function of arc length from the cell front.

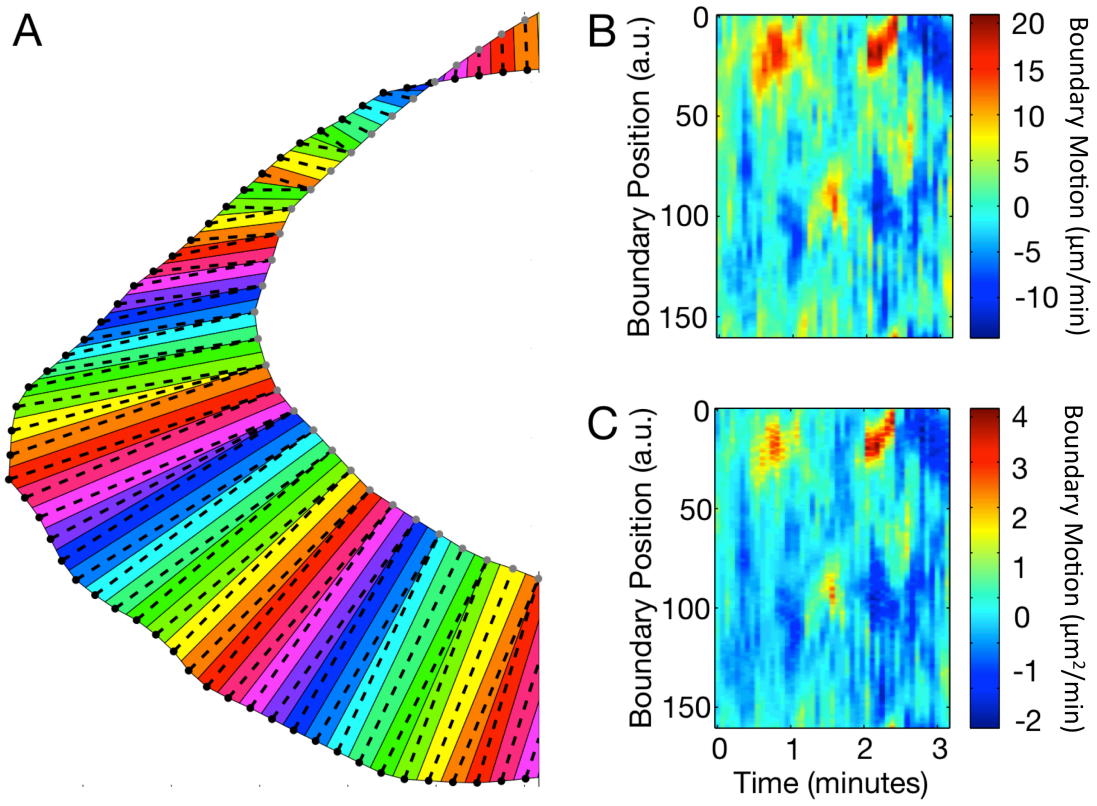

Figure 5.8. **Measuring protrusive and retractive motion. (A) The local motion mapping vectors (dashed lines) connect boundary points in frame *t* (gray dots) to boundary points in frame *t+1* (black dots). The length of the local motion mapping vectors is defined as the local motion measure (see B), while the area corresponding to each vector (shown as differently colored regions) is defined as the local protrusive/retractive area (see C). (B) The local motion measure. Red indicates regions of protrusive motion, while blue indicates retractive motion. (C) The local protrusive/retractive area.**

Chapter 6. A simplified description of shape dynamics

This chapter is preliminary work. Meghan Driscoll performed the experiments and analyzed the data.

6.1. Background

The shape dynamics of *Dictyostelium discoideum* explore a high-dimensional mathematical space. (The changing shape of a single cell is shown in Figure 6.1.) In the course of performing the experiments described in Chapter 5, we accumulated nearly 2,000,000 individual cell shapes, each of which is composed of 200 boundary points. The high dimensionality of cell shape dynamics presents a barrier to both our qualitative and quantitative understanding of cell migration. Patterns, even simple ones, can be difficult to observe and model in a high dimensional space. Also, statistical analyses or model fitting can require prohibitively large amounts of data (which is sometimes referred to as the *curse of dimensionality*). However, a wide variety of dimensionality reduction algorithms have been developed (149, 150). Can we use one of these algorithms to develop a reduced dimensional model of *D. discoideum* shape dynamics? A reduced-dimensional model might allow us to discover new patterns, to compare the shape dynamics of ensembles of cells, such as myoII- and aca- cells, and to dissect how signals, such as chemotactic and

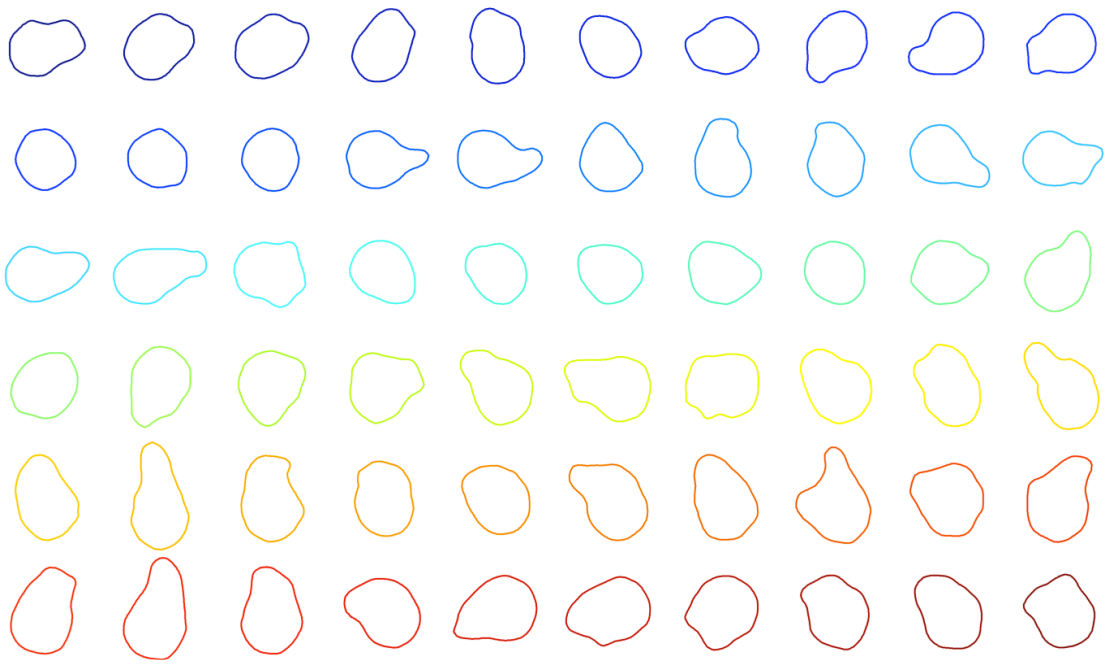

Figure 6.1. **The dynamic shape of a levitating, myoII-, *D. discoideum* cell (see Chapter 3). The initial shape is dark blue and the final shape is dark red, so the shapes are read left to right, top to bottom. Shown is the shape of the cell every 4 seconds.**

topographical cues, couple to shape dynamics. (MyoII- cells lack the ability to contact properly, while aca- cells lack the ability to relay chemotactic signals.)

Dimensionality reduction techniques usually fall within the province of the machine learning field. Machine learning, which is essentially statistical engineering, provides us with many tools for exploring large data sets. However, the goal of most machine learning algorithms is prediction, not insight. Some machine learning algorithms are essentially trained black boxes that predict outcomes extremely well but whose inner workings are completely opaque. Can we use machine learning tools, such as dimensionality reduction, not simply to predict shape dynamics but to gain insight into the underlying mechanisms driving shape dynamics?

The problem of how to gain insight into a high-dimensional system by reducing its dimensionality is one focus of the newly emerged field of the physics of behavior. Describing the physics of behavior, Stephens *et al.* argue that the key to understanding complicated behavior is not to mandate a specific simplification, but instead to start with large amounts of data and then to extract a simplification automatically (151). To analyze the shape dynamics of *Caenorhabditis elegens*, Stephens *et al.* used a dimensionality reduction technique, principal component analysis, to decompose worm shape into its underlying modes (79, 152). They found that 95% of the variation in worm shape could be accounted for with just a few "eigenworm" modes.

6.2. Results

6.2.1. Feature extraction – Principal component analysis

Dimensionality reduction techniques can be organized into two categories: feature selection and feature extraction. Feature selection algorithms reduce the dimensionality of the feature space by choosing a subset of the original features. Feature extraction algorithms reduce the dimensionality by creating new features from the old features. Principal component analysis (PCA), which is a feature extraction method, is probably the most common method of dimensionality reduction. PCA has previously been used to analyze cell shape (79, 153), and the effects of cell shape representation on PCA have been explored (154). In PCA, an orthogonal basis of principal components is constructed in feature space. The first principal component is the linear combination of features that represents the direction of

greatest variance in the data, the second principal component, which is orthogonal to the first, is the linear combination of features that represents the direction of next greatest variance, *etc*.

To find the PCA modes of *D. discoideum* shape, we first aligned the shapes by forcing them to have the same centroid position, orientation, and front-back directionality (where front and back are defined by migration direction, not the instantaneous shape). We defined the cell front to be boundary point 0 and rotated each shape so that boundary point 0 was at 0°. Figure 6.2 shows cell shapes in shape space. Shapes in shape space are aligned similarly to shapes aligned for PCA. (Shapes in shape space were forced to have the same centroid position, orientation, and radius. Boundary point 0 was defined to be either the front or the back of the cell, and each shape was rotated so that boundary point 0 was at 0°.) Waves of high boundary curvature are visible when shapes in consecutive frames are overlaid (see Figure 6.2B), which suggests that they are also visible in the shapes aligned for PCA. (Figures 6.2C and 6.2D show the global and local shape measures in shape space. The global and local motion measures become distance measures in shape space. The global motion measure becomes the Procrustes distance, which is a standard measure of the distance between shapes, while the local motion measure becomes a protrusive/retractive measure of shape distance.)

The mathematical representation of shape affects the modes found by PCA. One of the simplest representations of a shape is the positions of its boundary points. The principal components of boundary point position are shown in Figure 6.3A. Figures 6.3B and C show the principal components when the shape is parameterized

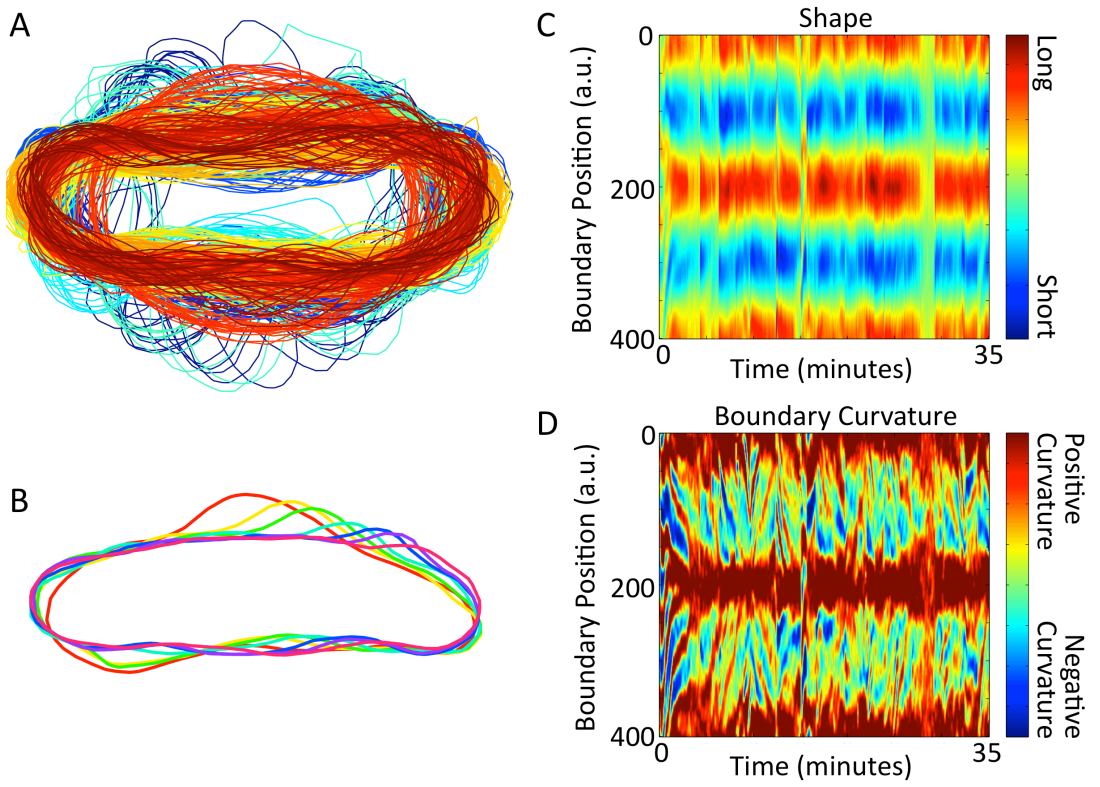

Figure 6.2. **A cell in shape space. (A) The overlaid shapes of a cell in shape space. (B) Looking at just a few shapes from consecutive frames, we see that curvature waves are visible in shape space. (C) The distance from the centroid to each boundary point as a function of time and boundary point position. Red indicates that the boundary point is far from the centroid, while blue indicates that it is close to the centroid. (D) The boundary curvature. Red indicates regions of large positive boundary curvature, green indicates flat regions, while blue indicates regions of large negative boundary curvature. (Since the shapes in this figure are in shape space, the scales in A and B are unitless, as are the colorbars in C and D.)**

by our global shape measure (the distance from the centroid to each boundary point), and our local shape measure (boundary curvature), respectively. In these figures, the principal components are ordered left to right from most to least dominant. While just

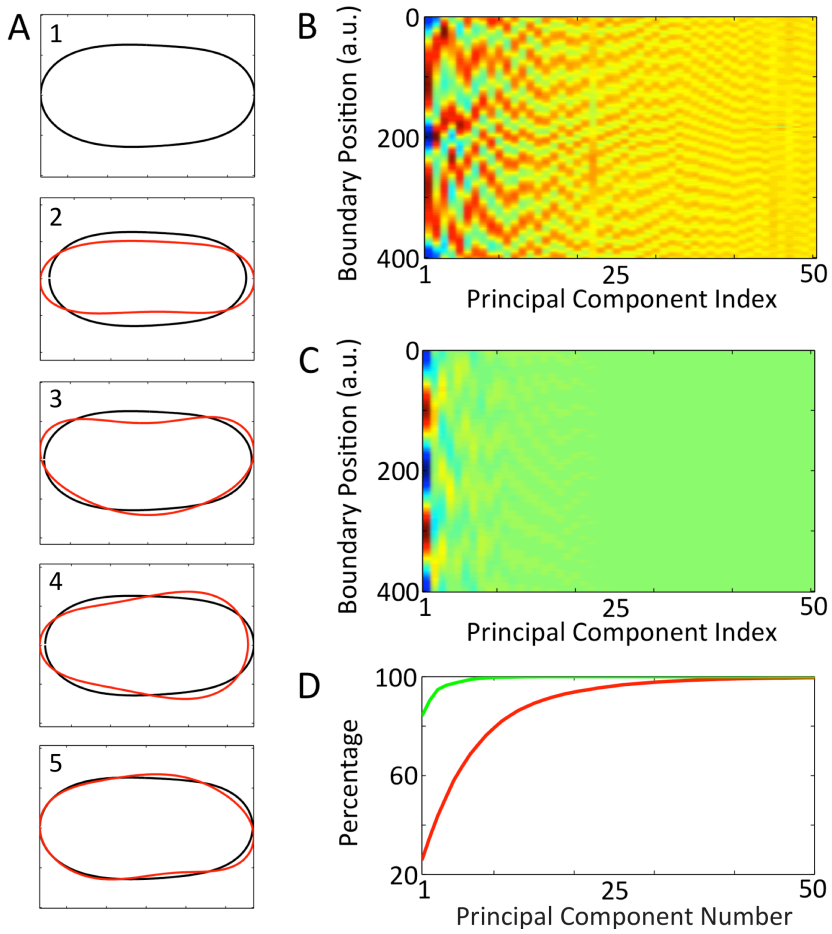

Figure 6.3. **PCA of shapes and shape measures. (A) The PCA of boundary point positions. The black outlines are the first principal component, and the red outlines are the first principal component plus the *i*th principal component. The principal component index, *i*, is indicated by the label. (B) The PCA of boundary curvature. (C) The PCA of global shape. The global shape is the distance from each boundary point to the shape's centroid. The principal components are ordered left to right from most dominant to least dominant. (The colorbar for B and C is shown in Figure 6.4A. It has arbitrary units.) (D) The percentage of the variance of a measure represented by the principal components as a function of the number of principal components. The percentage for the global shape measure is green and for boundary curvature is red. More principal components are required to reproduce boundary curvature than global shape. (~20 wildtype cells; ~10,000 shapes; from the Chapter 2 dataset.)**

a few principal components describe more than 95% of the variance in the global shape measure, more than 20 principal components are required to describe 95% of the variance in the boundary curvature (see Figure 6.3D).

Since shapes are represented as linear combinations of the principal components, only the first principal component resembles a cell shape. The remaining components show specific ways in which cell shapes tends to vary. The magnitude and sign of the extracted principal components can be fixed arbitrarily. In Figure 6.3A, the black outlines are the first principal component and the red outlines are the first principal component plus the *i*th principal component. The principal component index, *i*, is indicated by the panel label. (While I added the *i*th principal components to the first principal component, subtracting the *i*th principal would have been equally legitimate.) Roughly speaking, the first principal component is cell size, the second is cell elongation/rounding, the third is a type of cell turning, the fourth is widening/narrowing of the cell front compared to the back, and the fifth is another type of cell turning.

The PCA of boundary curvature is explored in Figure 6.4. (The boundary-curvature principal components shown in Figures 6.3B and 6.4A were calculated from different data sets.) The principal components of boundary curvature are sinuous (approximately sinusoidal) and occur as mode pairs that are phase separated from one another by a quarter of the mode's wavelength. (The mode pairs are labeled by mode number in Figure 6.4A.) Like sine and cosine functions, each mode pair can be used to reconstruct a sinuous pattern of any phase with the same wavelength. Together, the principal components then act as an approximate Fourier representation.

Figure 6.4. **PCA of boundary curvature. (A) The first 26 principal components, which are ordered left to right from most significant to least significant. The principal components are arranged in mode pairs, in which the phases differ by about one quarter of the mode's wavelength. (The colorbar has arbitrary units.) (B) The relative dominance of each principal component. The dominance falls off roughly exponentially with increasing principal component index. The two modes in each pair have similar dominances, especially at higher indices. Since the orientations of all of the shapes were forced to be the same, the dominance of the first principal component is doubled, while the dominance of its mode pair, index 20, is suppressed. (C) The first three principal components. The first principal component is shown as a red line, the second as a solid blue line, and the third as a dashed blue line. (D) The 8^{th} through 11^{th} principal components. The 8^{th} principal component is shown as a solid purple line, the 9^{th} as a dashed purple line, the 10^{th} as a solid green line, and the 11^{th} as a dashed green line. (Data from an 80-minute movie of aca- cells migrating on a flat surface; ~48,000 shapes; from the Chapter 5 dataset.)**

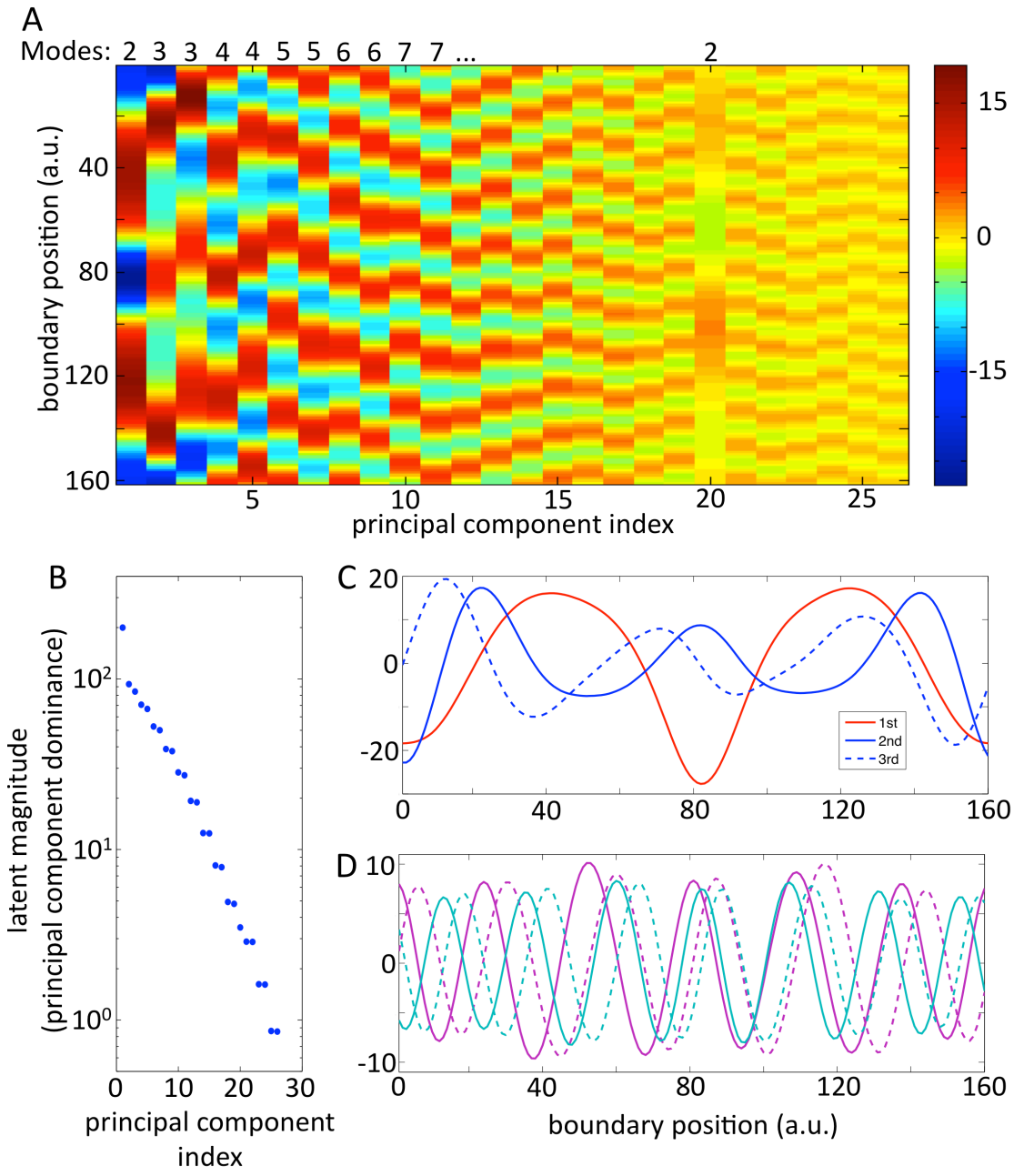
A
Modes: 2 3 3 4 4 5 5 6 6 7 7 ... 2
boundary position (a.u.)
principal component index
B
latent magnitude
(principal component dominance)
principal component
index
C
1st
2nd
3rd
D
boundary position (a.u.)

The dominance of the mode pairs falls off roughly exponentially with mode number (see Figure 6.4B). (Here, the dominance is defined as the extent to which a principal component is used to represent an ensemble of shapes.) Because we forced the shapes to have the same orientation, the strength of the first principal component is doubled while the strength of its mode pair (the 20^{th} principal component) is suppressed.

The principal components of boundary curvature are ordered. Could this ordering result from some sort of artifact? Our pixel resolution is likely near a principal component index of 50, while curvature smoothing should start to limit our resolution around index 40. Unlike boundary curvature, though, the global shape measure is not smoothed. However, the principal components of global shape show similar Fourier-like mode pairs. The dominance spectrum of the global shape principal components also falls off roughly exponentially, though, much more quickly than the spectrum of boundary curvature principal components.

6.2.2. Feature extraction – Frieze pattern analysis

Another, albeit non-standard, feature extraction technique is the analysis of boundary curvature kymographs as frieze patterns. Frieze groups are 1-D periodic symmetries in 2-D space (155). Liu *et al.* developed an algorithm to reconstruct the fundamental frieze symmetries in a noisy image (155). The frieze symmetries include the horizontal and vertical translation symmetry, as well as the horizontal glide-reflection symmetry, which corresponds to the left-right-left-right pattern of curvature waves. This correspondence may allow for the extraction of easily interpretable features of shape dynamics. Unlike PCA, which we used to reduce the

dimensionality of shapes, we could use frieze patterns to reduce the dimensionality of shape dynamics.

6.2.3. Feature selection – Measure clustering

In Chapter 4, we found that measures of nuclear shape hierarchically cluster into roughly three families: size, boundary contortion, and elongation (see Figure 5.3.). While measure clustering is not a dimensionality reduction technique, it serves a function similar to a feature selection technique by allowing us to explore the redundancies and dependencies between measures. Figure 6.5 shows a hierarchical clustering of the *D. discoideum* shape and motion measures. We analyzed the migration of aca- cells migrating on glass coverslips. Independently analyzing the data from two movies that were taken more than a year apart, we found consistent clustering of the measures. Shape measures and motion measures cluster into two separate groups, though measures of shape are better correlated with one another than measures of motion. Within the group of shape measures, the size measures form a tightly knit family, while the eccentricity and boundary contortion measures are associated with one another but may or may not form separate families.

6.3. Future work

Can we construct a meaningful, reduced dimensional model of *D. discoideum* shape dynamics? Reducing the dimensionality of cell shape dynamics is useful only if we can make sense of the reduced data. Using the dynamics of the boundary point position modes, can we automatically deduce the cell migration cycle for *D. discoideum?* (Figure 1.1.B. shows a carton model of the amoeboid cell

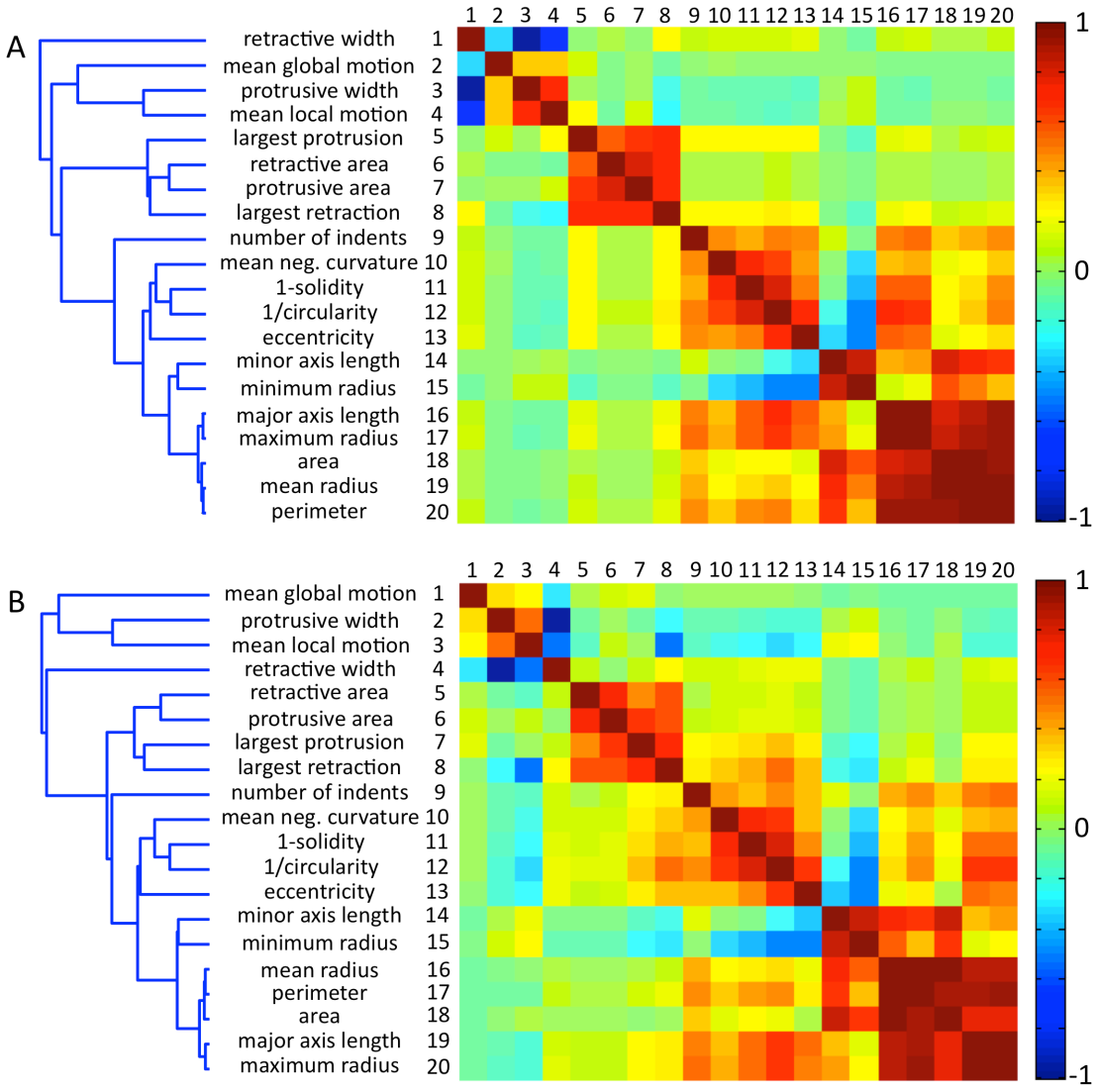

Figure 6.5. **Hierarchical clustering of shape measures. (A) Data from a movie of aca- cells migrating on a flat, glass coverslip. The hierarchical clustering, displayed in a dendrogram, is shown on the left, and the covariances between all pairs of measures are shown on the right. The covariance is represented by color. (B) Data from another movie, taken more than a year later, of aca- cells migrating on a flat, glass coverslip. The measures from both datasets cluster similarly.**

migration cycle.) To what extent does a cell migration cycle capture typical *D. discoideum* behavior? If the principal components are temporally correlated, we may

be able to use those correlations to derive a cell migration cycle. We also expect some of the boundary point position modes, such as the turning or elongation modes, to be periodic. Cell protrusions, for example, are extended roughly every 20 seconds in a zig-zagging manner, so some of the turning modes might have a periodicity of 40 seconds.

The principal components of boundary curvature are sinuous mode pairs with a quarter-wavelength phase offset (see Figure 6.4). In Stephens *et al.*, the first two principal components of *C. elegens* shape were similarly found to be a pair of sinuous forms with a quarter-wavelength phase offset (79). The authors found that the first two principal components described a traveling wave, which appeared as a circle in the joint probability distribution of the two modes. Could we similarly quantify traveling waves in *D. discoideum* shape? If so, can we find regular patterns in the wave dynamics? Also, since each Fourier mode represents shape information at a different length scale, we could examine how shape information flows across length scales. One hypothesis is that features become smaller as they move from the front to the back of the cell, and so shape information would flow from larger to smaller length scales.

How do the shape dynamics of ensembles of cells compare? Examining boundary curvature kymographs, the shape dynamics of swimming and crawling cells appear similar. (The dynamics of swimming cells seem to be sped up by a factor of 3.5 compared to crawling cells, though the dynamics appear otherwise similar.) On the other hand, the shape dynamics of some mutant cells, such as myoII- cells, appear distinct from wildtype cells. How do the shape dynamics of ensembles of cells

compare? We could compare ensembles using simple measures such as speed and area, but shape dynamics are likely not well represented by these measures. Instead, we could use a reduced dimensional model of shape dynamics to compare ensembles. Differences in shape dynamics could be characterized by analyzing differences in principal component dynamics.

How do signals couple to shape dynamics? Chemotactic and topographical signals direct the migration of *D. discoideum*. How do these signals couple to the underlying modes of shape dynamics? The intricacies of the coupling might yield insights into the mechanisms behind topographical guidance. Stephens *et al.* found that the response of *C. elegens* to a thermal signal depended on the phase of the traveling wave described by the first two principal components (79). Using a controlled series of thermal impulses, they were able to steer the direction of worm movement. Could *D. discoideum* shape similarly modulate cellular response to chemotactic signals? Chemotactic signals, such as signaling waves of cAMP, are known to induce changes in cell shape (56, 57). If chemotactic signals altered cell shape and cell shape altered responsiveness to chemotactic signals, then cell shape would function as a physical component of the chemotactic signaling pathway. Measuring how mode dynamics couple to a chemotactic signal might aid in elucidating the role of cell shape in cell signaling.

Chapter 7. Discussion

7.1. Thesis summary

Much of the work in this thesis has been guided by the question of how cells migrate in 3-D environments. In particular, by the question of how *D. discoideum* move in response to the physical shape of their environment. Since *D. discoideum* are often studied moving on flat surfaces, we began by studying cells migrating on such surfaces (see Chapter 2). Cell shape provides a window into how the internal machinery of a cell is coupled to its external environment. We thus developed a set of tools for analyzing cell shape dynamics. We used a snake algorithm to extract cell shapes and a least squares mapping to track boundary points from frame to frame. To visualize shape dynamics, we developed four boundary-point-associated measures: a global and local measure of cell shape, and a global and local measure of cell motion. (In Chapter 5, we developed another measure of local boundary motion.) Examining boundary curvature, which is the local shape measure, we found that cells migrating on flat surfaces exhibit waves of high boundary curvature that travel from the fronts to the backs of cells. These regions of high boundary curvature are stationary relative to the coverslip, but appear as curvature waves relative to the cell. The waves travel at 10 μm/min relative to the cell, which is the average speed of *D. discoideum*.

In Chapter 3, we continued to investigate how surface shape affects *D. discoideum* migration. Since even a flat surface affects the behavior of the cell if the

cell can stick to the surface, as a control we measured the shape dynamics of cells that are not adhered to a surface. *D. discoideum*, though, readily adhere to many surfaces. We forced them off of surfaces by using chemoattractants to induce them to extend over cliff edges and by levitating them using a buffer with a reduced salt concentration. We found that non-adhered cells exhibit waves of high boundary curvature that travel from the cell fronts to the backs at 35 μm/min. The boundary curvature dynamics of non-adhered and adhered cells appear similar, except that the dynamics of non-adhered cells are sped up by a factor of about 3.5.

Do curvature waves in non-adhered cells relate to the cell migration of adhered cells? Comparing the boundary curvature and local motion of cells migrating on a flat surface, we found that bursts of protrusive motion are associated with the initiation of curvature waves. Examining *D. discoideum*'s "footprint," the region over which a cell is in contact with the surface, we found that when a region of high curvature contacts the surface, it sticks to the surface. (Regions of high curvature are more easily seen in the "footprint" shape than in the cell shape.) *D. discoideum* protrusions, though, do not immediately adhere to the surface and only exert a force ~20 seconds after they are extended (16). Before they contact the surface, do protrusions travel laterally along the membrane like curvature waves? Measuring the mean squared displacement of protrusive motion, we found that at short time scales of less than ~20 seconds protrusive motion along the boundary is super-diffusive. Based on these observations, we hypothesized that protrusive motion in *D. discoideum* is wave-like. In our model, a newly extended protrusion travels laterally along the side of the cell. If the protrusion interacts with a surface, it sticks to the surface, which

anchors the cell locally and allows the cell to migrate forward. Otherwise, the protrusion flows backwards to produce a swimming-like motion. Swimming and crawling would then result from the same protrusive process.

In Chapter 4, we applied some of the shape measures described in Chapters 2 and 3 to nuclear shape. The phenotypic hallmark of Hutchinson-Gilford progeria syndrome is nuclear blebbing, which is typically measured via manual, blind counting. We characterized blebbing automatically by visualizing the boundary curvatures of ensembles of nuclei and by using various measures of boundary contortion, including mean negative curvature, tortuousity, and solidity.

In Chapter 5, we analyzed the response of *D. discoideum* to a type of simple 3-D surface: topographical nanogratings composed of parallel ridges. The patterning of focal adhesion complexes is a commonly hypothesized mechanism for contact guidance (74, 75). However, we found that *D. discoideum* exhibit contact guidance even though they lack mature focal adhesion complexes. The boundary motion of *D. discoideum* is primarily governed by actin, which has been shown to have wave-like dynamics (19). In Chapters 2 and 3, we found that *D. discoideum* shape also has wave-like dynamics. Could the wave-like dynamics of the migration machinery be affected by the boundary conditions of surface shape? We hypothesized that contact guidance could result from a resonance between cellular waves and the nanogratings. We measured the contact guidance efficiencies of nanogratings with ridges spaced various distances apart and found that ridges spaced 1.5 μm apart best guided cells. Modeling contact guidance on nanogratings in terms of stochastic cellular harmonic oscillators that couple to the nanograting periodicity, we found that the spatial and

temporal scales of the oscillations that best couple to the surface are consistent with those of protrusive dynamics. Our results suggest that one possible mechanism for contact guidance is the coupling of surface topography to protrusive dynamics, which are governed by actin dynamics.

The high dimensionality of shape dynamics presents a barrier to quantitative analysis. Can we construct a reduced dimensional model of shape dynamics? In Chapter 6, we presented some preliminary dimensionality reductions. We used principal component analysis to find the modes of boundary point position, global shape (the distance from the centroid to each boundary point), and boundary curvature. The principal components of boundary point position describe modes such as size, elongation/contraction, and turning. The principal components of boundary curvature form a Fourier-like representation. In the future, we plan to analyze the principal component dynamics, compare ensembles of cells, and examine how signals couple to cell shape.

7.2. Future directions

Many cells migrate in crowded environments. However, the typical model of cell migration, front protrusion followed by adhesion and back retraction (shown in Figure 1.1), does not describe how cells navigate around obstacles: If a cell with a uniform protrusive front were to run into a wall, there is no obvious mechanism for the cell to stop trying to go forward and instead go either left or right. Weiner *et al.* suggested that wave-based protrusions would naturally result in obstacle avoidance (20). If a cell with a wave-like protrusive front were to run into a wall, the waves might be able to break the symmetry and allow the cell to go either left or right (14).

(This symmetry breaking is perhaps similar to how a cell extended over a cliff leaves the cliff edge by swinging its front to the cliff edge.) Analyzing cells on nanogratings, we found evidence that protrusive waves might play a role in contact guidance. Protrusive dynamics are principally governed by actin dynamics, so are actin waves a possible mechanism for contact guidance and obstacle avoidance?

How are actin polymerization waves affected by ridges and obstacles? Contact guidance and obstacle avoidance can both be considered sub-problems of the general problem of how cells interact with interfaces. In *D. Discoideum* waves of polymerizing actin can be imaged with LimEΔcoil-GFP cells. Using a combination of multiphoton absorption polymerization (MAP) (106) and micro-contact printing, we could fabricate a variety of physical and chemical interfaces (36). We could begin by observing how actin waves interact with simple interfaces, such as straight, high walls. Do actin waves interact with walls in a manner consistent with an obstacle avoidance system? Weiner *et al*. observed that Hem-1 waves that collide with the boundary of another cell are extinguished (20). Do actin waves that collide with a wall extinguish similarly? Also, do the actin waves appear to lead to cell turning?

We could study the effects of various types of walls. Do cells avoid adherent obstacles differently from non-adherent obstacles (very slippery obstacles)? *D. discoideum* do not adhere to surfaces coated with polyethylene glycol (PEG). We could observe actin waves as cells collide with PEG-coated walls. What if the obstacle is not even a physical object, but instead a void to which cells cannot adhere? We could observe actin waves as cells interact with PEG-coated regions of the coverslip, or PEG ponds. (While *D. discoideum* can swim over PEG surfaces, since

we have never seen a cell jump off of a cliff, we hypothesize that adhered cells will not attempt to swim across PEG ponds. On the other hand, swimming cells would probably prefer to leave the pond and adhere to a surface.) What if a cell runs into another cell, do the actin waves behave still differently?

To understand better how actin waves interact with adherent and non-adherent obstacles, we could image the actin wave dynamics in non-adhered cells? Cells could be made to not adhere by levitating them or by confining them inside PEG-coated micro-channels. Actin waves travel at 10 μm/min in adhered cells (19). Do actin waves also travel at that the same speed in levitating cells? In suspended cells, are actin waves related to curvature waves? In particular, can we understand why waves of high boundary curvature travel at 35 μm/min in suspended cells? How would changing the actin wave speed, perhaps with a latrunculin titration, affect the curvature wave speed?

We could also explore the effects of interface shape. Do cells avoid square pillars and circular pillars differently? In general, waves are affected by interface roughness. Does a rough wall or glass-PEG interface result in different wave dynamics than a smooth interface? Also, does the shape of the cell footprint affect actin wave propagation? Various groups have studied cells on ECM islands (37, 38). *D. discoideum* could be studied on small islands of glass surrounded by PEG-coated regions. Since the footprint size of *D. discoideum* is considerably smaller than the cell size, cells might wiggle off of the surface. Nevertheless, would cells confined to a circular footprint exhibit different actin wave behaviors than cells confined to

elliptical islands? Do corners in the footprint, caused by square or star-like islands, alter wave behavior?

We took reflection microscopy images of cells on ridges spaced 3 μm apart. We found that in the middle of the grooves cells adhere to the surface, while at the sides of the grooves they do not. Ridges then induce alternating bands of adhesivity and non-adhesivity. Could contact guidance by ridges be understood in terms of these adhesion bands, or is a 3-D surface required? Would cells on alternating 1.5 μm wide bands of glass and PEG exhibit contact guidance?

How does topographical sensing relate to the chemotactic signaling pathway? Are the topographical sensing and chemotactic signaling pathways entirely unrelated, or, perhaps more likely, does the topographical signaling pathway feed into the chemotactic signaling pathway? In response to a chemoattractant gradient, PH-Crac-GFP localizes to the front of cells (93). In response to a uniform chemoattractant, PH-Crac-GFP localizes to membrane patches from which pseudopodia tend to extend (156). In ridge experiments cells are exposed to a uniform chemoattractant. In response to a topographical signal does PH-Crac-GFP localize to the front of cells that are aligned parallel to the ridges? If there are PH-Crac-GFP patches are they correlated with future pseudopods or, perhaps, with ridge location?

The two most commonly hypothesized mechanisms for contact guidance are focal adhesion patterning and filopodial sensing (49). *D. discoideum* exhibit contact guidance even though they lack mature focal adhesions. However, *D. discoideum* do have filopodia. Cells lacking dDia2, to which we have access, have reduced numbers

of filopodia (145). We could therefore explore the role of filopodia in contact guidance by comparing the surface contact guidance efficiencies of these cells and aca- cells.

Appendix A. A movie: The adventures of Dicty the *Dictyostelium* cell.

This appendix is adapted from Driscoll, Kopace, Li, McCann, Watts, Fourkas, and Losert (157). The text and figures are used here with permission.

Movie: http://link.aip.org/mm/CHAOEH/1.3212926/009994chav1.mov.

We present a movie that shows *Dictyostelium discoideum* traversing various topographical obstacles, particularly those that affect the direction of cellular migration. Topographical features, such as ridges (speed bumps) and cliffs, were fabricated using multiphoton absorption polymerization (142). As the cells encountered these topographical features, we tracked their motion.

When cells undergoing chemotaxis, directed migration in response to a chemical signal, are directed off of a cliff, they do not fall off the cliff. Instead, they search for new attachment points, eventually change direction, and continue moving along the edge of the cliff (Figures A.1B, C). When a tightrope is suspended between cliffs, some cells find the tightrope and migrate along it, as shown in Figure A.1D.

To disentangle motion directed by chemical signals from that directed by surface topography, we used mutant *aca- D. discoideum* that do not emit cyclic adenosine monophosphate and thus do not provide each other with directional chemical signals. Figure A.2 shows the tracks of *aca-* cells undergoing

chemokinesis, migration in response to a uniform chemical stimulus, on a flat surface. This image provides a visually striking indication that such cells migrate randomly. When these randomly migrating cells encounter a ridge, they tend to move along that ridge, even if it is not as high as the cell (Figure A.1A).

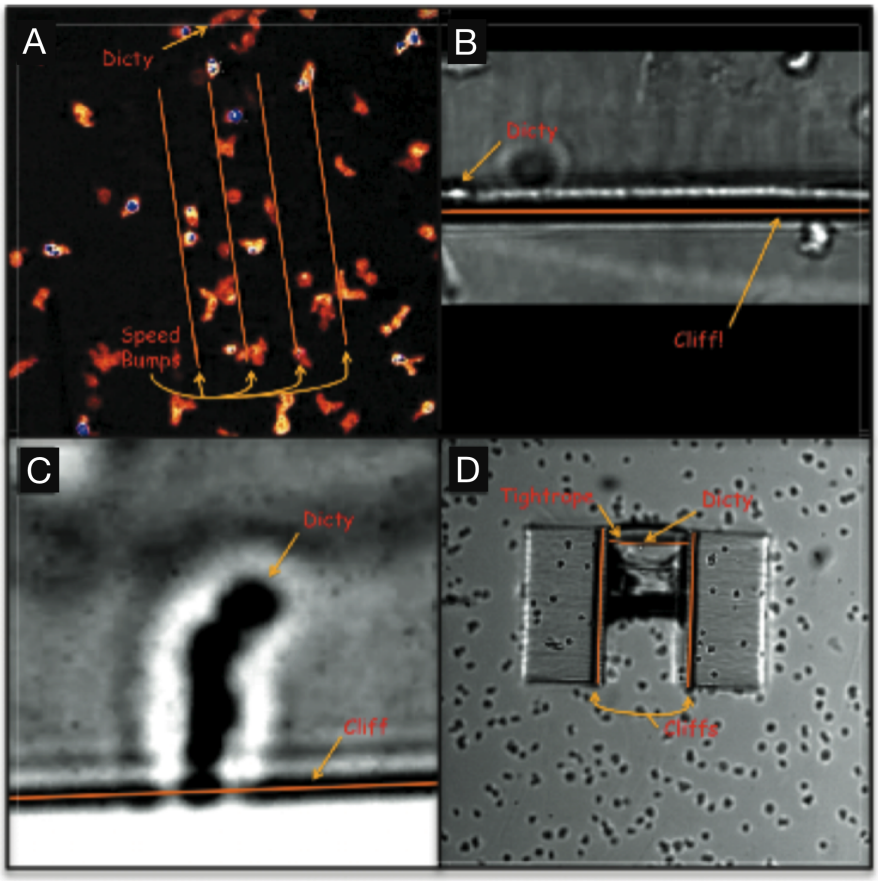

Figure A.1. **The migration of *D. discoideum* on three-dimensional features. The cell labeled Dicty is (A) moving along and swinging from speed bumps, (B) moving along the edge of a relatively high cliff, (C) wiggling off of a cliff, and (D) crawling along a tightrope that is suspended between cliffs.**

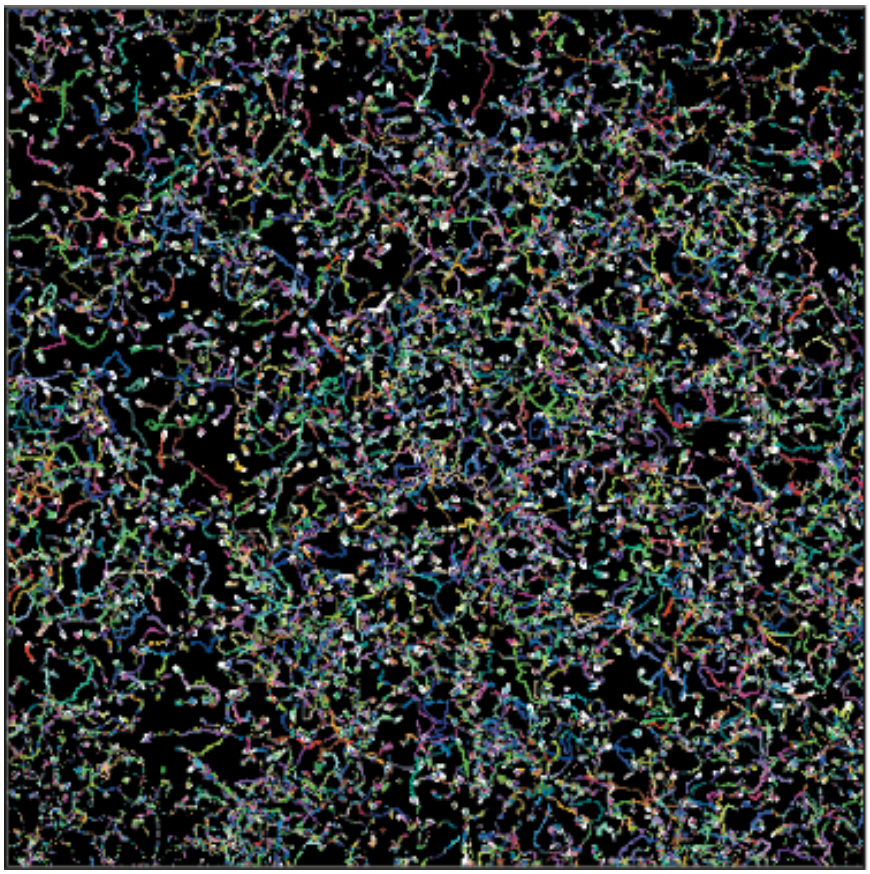

Figure A.2. **The random migration of *D. discoideum* on a flat surface. Each white shape is a cell, while the colored line associated with each cell is the path that cell took as it crawled about randomly on the flat glass surface.**

Appendix B. A guide to the software

This appendix describes the code suite 'Dicty Analysis', which was used in Chapter 5 to analyze the dynamic shapes of multiple cells. 'Dicty Analysis' uses a snake algorithm to automatically extract the shapes of fluorescently imaged amoebae, tracks the shapes from frame to frame, and provides tools to analyze the dynamic cell shapes.

Some of Section B.4 also appears in the Materials and Methods sections of Chapters 2 to 5 but is included here for convenience.

B.1. The various code suites

Four different suites of code were used in this thesis. 'Cell Shape Analysis' was used in Chapters 2 and 3, to analyze the dynamic shape of individual cells. ('Cell Shape Analysis' is run via **sdemo.m**, **cell_shape_analysis.m** or one of the **accumulate** functions, and, optionally, **accumulating_automator.m**.) 'Run Lines', which is an adaptation of a code suite written by Colin McCann (91), was used in Chapter 5 to analyze the velocity, eccentricity, and orientation of cells on ridges. ('Run Lines' is run via **runLinesROI.m**.) 'Nucleus Analysis' was used in Chapter 4, to analyze the shape of nuclei. ('Nucleus Analysis' is run via **nucleus.m**.) Finally, 'Dicty Analysis' was used in Chapter 5 to analyze the dynamic shape of multiple

cells. ('Dicty Analysis' is run via either **shapes.m** or **accumulateShapes.m**.) 'Dicty Analysis' was designed as a replacement and improvement to the other suites of code. However, while 'Dicty Analysis' provides a framework that can accommodate the functionality of the other code suites, not all of that functionality is present in 'Dicty Analysis'.

B.2. *Running* Dicty Analysis

To analyze a single movie:

1: Save images in a directory. The code assumes that images are tif files and that image names end in a number. All files in the directory that end in a unique number will be analyzed. (You could open your movie in ImageJ, and save it, in an otherwise empty directory, as a gray-scale image sequence.)

2: Open **shapes.m**. (There are additional helpful comments in **shapes.m**.)

3: Set directories. In particular, in SET DIRECTORIES set *inDirectory* and *savePath.*

4: Set parameters. In SET PARAMETERS, set at least *frameTime*, *pixelsmm*, *minRegionSize*, *centerTravelThresh*, *maxRegionSize*, *boundaryPoint*, and *frameDelta.*

5: In TURN PROGRAMS ON AND OFF set the *run, verify,* and *plots* variables. Each section enabled by *run* saves and loads data independently, so once you have run a section you do not need to run it again to run sections dependent on it.

To analyze multiple movies:

1: Save each movie's images in its own directory. (see 1 above)

2: Open **accumulateShapes.m**.

3: Set directories for each movie. In particular, under each movie heading, set *inDirectory* and *savePath.*

4: Set parameters for all movies in **shapes.m** or for individual movies in **accumulateShapes.m**. Parameters defined in **accumulateShapes.m**, or more precisely those passed to each call of **shapes.m**, overwrite those set in **shapes.m**. In some combination of the two m-files, set at least *frameTime*, *pixelsmm*, *minRegionSize*, *centerTravelThresh*, *maxRegionSize*, *boundaryPoint*, and *frameDelta*.

5: Set the *run, verify* and *plots* variables in **accumulateShapes.m**. Each section enabled by *run* saves and loads data independently, so once you have run a section you do not need to run it again to run sections dependent on it.

B.3. Modifying Dicty Analysis

B.3.1. Adding features

The *run*, *verify*, and *plots* variables are binary arrays that are used to turn on and off different features of the code. Code features controlled by *run* analyze images or data, those controlled by *verify* output image sequences, while those controlled by *plots* output individual plots.

To add analysis or major plotting functionality to 'Dicty Analysis':

1: Open **shapes.m**.

2: In TURN PROGRAMS ON AND OFF, lengthen *run*, *verify*, or *plots*, and describe the feature you are adding.

3: After RUN PROGRAMS, add an if loop that runs your new feature if the corresponding *run*, *verify*, or *plots* variable has been set to 1.

4: Add any hard coded parameters to both SET PARAMETERS and the list of variables to be saved in ASSIGN PARAMETERS.

5: Update the *run, verify* and *plots* variables in **accumulateShapes.m**.

The *verify* and *plots* functions accommodate multiple options. For instance, the plot that is generated as a result of enabling *plots(*1*)* is dependent on the value of the option variable associated with *plots(*1*),* which in this case is *plotPlots*. If you are adding a new type of plot, consider adding it as an additional option to one of the existing *verify* or *plots* functions.

To add minor plotting functionality to 'Dicty Analysis':

1: Open **shapes.m**.

2: In TURN PROGRAMS ON AND OFF, add the name of your feature to one of the *verify* or *plots* options lists.

3: Determine which function the *verify* or *plots* variable you are modifying calls. (Functions are called in if loops after VERIFY or CONSTRUCT PLOTS.)

4: Open that function, and add your feature to the if-elseif loop that iterates through the allowed values of the option variable.

B.3.2. Major variables

Sections of the code enabled by *run* save data that are accessible to other parts of the code. Sections enabled by *verify* or *plots* can save image sequences or plots, but do not save data that are accessed by the rest of the program. The following are useful variables generated by sections of *run*. The section of *run* that generates the variable is shown in parenthesis. (See the code and *B.3* for more details.)

N: The total number of frames. *N* is always indexed by *i*. (*run(*1*)*)

picture: Stores information about each frame. For example, it stores the file name, file number, and the approximate boundaries of cells within the frame. (*run(*1*)* and *run(*2*)*)

labeledImages: Not a variable, but a directory of binarized versions of each frame. (The outline of each binary object is used to initialize a snake algorithm.) Within each binarized image, each shape is labeled with a unique index. This shape index can be associated with the ID of a tracked object via the variable *blob*, each element of which stores a list of these indices in the field *labels*. (*run(*2*)*)

blob: Stores information about tracked shapes. Each tracked object in *blob* is assigned an ID, which is always indexed by *b*. The sections of code enabled by *run* load the last saved version of *blob*, though each section also saves a backup copy of *blob*. Check the end of each function for the name of the backup. In *run(*7*)* and higher, *shape* replaces *blob*. *(run(*3*)* to *run(*6*)*)

frame2blob: A list of the blob ID's in each frame. If you want to perform operations over frames instead of over blobs, *frame2blob* can be very useful. *(run(*3*)* to *run(*6*)*)

M: The number of boundary points in each snake per frame. *M* is always indexed by *j*. (*run(3)*)

shape: Stores information about tracked shapes. Each tracked object in *shape* is assigned an ID, which is always indexed by *s*. While information stored in *blob* aids in tracking, information stored in *shape* aids in data analysis. *shape* is generated from *blob* in code enabled by *run(7)*. As with *blob*, the sections of code enabled by *run* load the last saved version of *shape*, though each section also saves a backup copy of *shape*. (*run(*7*)* and higher)

frame2shape: A list of the shape ID's in each frame. (*run(7)*)

B.4. How Dicty Analysis *works*

Analysis features of the code are turned on and off by changing the values of the binary array *run.* Each section below details the features that are enabled by an element of *run*. Section *B.3.1.* describes what is enabled by *run(*1*)*, and Section *B.3.2.* describes what is enabled by *run(*2*)*, *etc*.

B.4.0. Assigning parameters

shapes.m is a function that can be run with or without the input *parameters*. All fields of *parameters* are defined as variables by **assignParameters.m,** which is always called regardless of the value of *run*. For example, if you were to set *parameters.pixelsmm* to 1000, and then run shapes(*parameters*), the value of

pixelsmm hardcoded into **shapes.m** would be overwritten by 1000. **assignParameters.m** allows **accumulateShapes.m** to selectively reset the parameters of **shapes.m**.

B.4.1. Reading the directory

Given the name of a directory of images, *inDirectory*, **readDirectory.m** finds the names and numbers of the images within that directory, and saves that information in the variable *picture*. **readDirectory.m** assumes that the images in the directory are tif files, and that the image names end in consecutive numbers. (These assumptions will be met if you open your movie in ImageJ and save it, in an otherwise empty directory, as a grayscale image sequence.) **readDirectory.m** uses regular expressions to parse the image names, so if your image names are in a different format, you should only need to change the two parsing sections of **readDirectory.m**.

If *useROI* is enabled, **readDirectory.m** will also look for an image that will be used to define an ROI. This image is assumed to be a tif image without any numbers in its name.

B.4.2. Finding the approximate boundaries

Next, the approximate boundaries are found by **findBoundaries.m**. All of the parameters described here are set in **shapes.m**. In this function, a small amount, of uniform noise, *noiseLevelAdd*, is first added to the images to facilitate subsequent thresholding; images with low background variance would otherwise threshold badly. Since the brightness of images varies across experiments, the images are next gamma

corrected with a gamma of *adjustGammaPre* to deemphasize brightness differences at high intensities. Images are next preprocessed to find the approximate boundaries of the cells. The brightness and contrast of each image is adjusted until 1% of the pixels are saturated at low and high intensities. The images are again gamma corrected with a gamma of *adjustGammaPost*, since the intensities of dyed cells vary. Each image is binarized using Matlab's built-in thresholder, which uses Otsu's method (147). Objects that are too small to be cells (smaller than *minRegionSize*) are removed, and any holes in objects are filled in. To smooth the objects, the images are next eroded by *erodeImage* pixels and then dilated by *dilateImage* pixels. Objects that touch the border are removed, and objects that are too small to be cells are again removed. The convex hull, area, centroid position, and solidity of each object are then calculated for later use. The convex hull of a shape is the smallest convex polygon that encloses that shape, while the solidity of a shape is the area of the shape divided by the area of its convex hull. The images are next dilated by *dilateLargeCH* pixels, and the convex hulls of the resultant objects are calculated. Parameter values used for the analysis of *D. discoideum* are given in Chapter 5. **findBoundaries.m** saves data in fields of the variable *picture*, and saves the binarized images to the directory 'labeledImages' in the directory set by *savePath*.

The output of **findBoundaries.m** can be checked by using **plotApproxboundaries.m**, which is enabled by *verify(*1*)*, to plot the approximate boundaries on the original images. (To troubleshot **findBoundaries.m**, it is often easiest to visualize the image after each processing step. To do this, you may need to replace 'parfor' with 'for'.)

findBoundaries.m uses a parallel for loop ('parfor'). Unless you turn parallel computing on, though, Matlab will treat the 'parfor' loop as a 'for' loop, and so the program will likely run unnecessarily slowly. To enable parallel computing, type 'matlabpool open' on the command line before running **shapes.m**.

B.4.3. Tracking shapes

The approximate boundaries are next tracked using **trackBlobs.m**. All of the parameters described here are set in **shapes.m**. The tracking is done before the shapes are refined using a snake algorithm, because snaking is computationally expensive and tracking excludes some cells from further analysis. First, cells that overlap from frame to frame are found. Since the cells move little from frame to frame, we expect a cell in a given frame to overlap with itself in the next frame. An object A in the current frame is tracked to an object B in the next frame if B is the only object in the next frame to overlap with A and if A is the only object in the current frame to overlap with B. If multiple objects in the current frame overlap with the same object in the next frame, a new track is initiated for the object in the next frame and that track is marked as a clump of cells for later removal. Likewise, if multiple objects in the next frame overlap with the same object in the current frame, then new tracks are initiated for the objects in the next frame and the track associated with the object in the current frame is marked as a clump. New tracks are initiated for objects that do not overlap with objects in the previous frame. Tracked objects whose area changes by more than the percentage *areaChangeThresh* or whose centroid moves by more than *centerTravelThresh* pixels from frame to frame are split into two tracks. Finally, tracks that were marked as clumps or that have a duration of less than

minDuration frames are removed. Tracks that have a mean solidity less than *minSolidity* or that have a mean area larger than a cell (larger than *maxRegionSize*) are also removed, since these tracks might be clumps of multiple cells. Parameter values used for the analysis of *D. discoideum* are given in Chapter 5. **tracksBlobs.m** saves data in fields of the variable *blob*. The output of **trackBlobs.m** can be checked by using **plotBlobs.m**, which is enabled by *verify(2)*, to plot the convex hulls of the tracked, approximate boundaries on the original images. (**trackBlobs.m** has many edge cases and is vulnerable to extremely rare bugs (~1/500,000 shapes). No known errors of this sort exist, but they may be present.)

trackBlobs.m has been parallelized. See Section B.4.2. for more details.

B.4.4. Snaking shapes

The cell boundaries are next found to subpixel resolution using **findSnakes.m**, which uses an active contour (snake) algorithm (86). All of the parameters described here are set in **shapes.m**. The large, dilated convex hulls found in **findBoundaries.m** are first used as masks to select images of individual cells. Since the brightness of dyed cells varies, the brightness and contrast of the masked image of each cell is next adjusted until 1% of the pixels are saturated at low and high intensities. The binarization threshold is calculated using Otsu's method, but the image is not binarized. Instead, the image is nearly binarized by setting all pixel intensities below *paramsSnake.binLowerThresh* times the binarization threshold to 0 and all pixel intensities above *paramsSnake.binUpperThresh* times the threshold to 1. A gamma correction of *paramsSnake.blobGamma* is also applied. After filling the holes in the grayscale image, we next calculate the image gradient. Then, using code

described in (86), the gradient vector field is calculated. Again using code described in (86), we initialize an active contour with the convex hull of the approximate boundary, and then deform the snake *paramsSnake.numIterFirst* times. To analyze the *D. discoideum*, we use the following snaking parameters: *paramsSnake.alpha* (tension) 0.00002, *paramsSnake.beta* (rigidity) 0.00005, *paramsSnake.*gamma (step size) 1, *paramsSnake.*kappa (external force weight) 0.6, *paramsSnake.*dmin (minimum distance between boundary points) 0.5 pixels, and *paramsSnake.*dmax (maximum distance between boundary points) 1.5 pixels. We continue to deform the snake by *paramsSnake.numIterEvery* iterations at a time until it converges. Convergence is defined as an area change of *paramsSnake.convergeThresh* pixels or less over *paramsSnake.numIterEvery* snake iterations. Since objects that will later be removed, such as clumps of cells or cells that are too dim to snake effectively, take a disproportionate amount of time to snake, a maximum of *paramsSnake.runLimit* sets of *paramsSnake.numIterEvery* iterations is allowed beyond the initial *paramsSnake.numIterFirst* iterations. To achieve better boundary resolution, the snake is again deformed *paramsSnake.numIterEvery* times with dmin set to *paramsSnake.dmin*/2 pixels and dmax set to *paramsSnake.dmax*/2 pixels. Each boundary, regardless of length, is finally interpolated to have *paramsSnake.equidistantNum* boundary points. **findSnakes.m** saves data in fields of the variable *blob*, and saves backup data to the variable *blobSnake*. The output of **findSnakes.m** can be checked by using **plotSnakes.m**, which is enabled by *verify(3)* with *snakeType* set to 'snakeTrack', to plot the tracked boundaries on the original images.

findSnakes.m has been parallelized. See Section B.4.2. for more details.

More parameter values used for the analysis of *D. discoideum* are given in Chapter 5. The snaking parameters and the number of iterations allowed before checking were chosen so that the snakes would converge to the correct boundaries as quickly as possible.

If you are analyzing an image in which shapes are a hundred or more pixels across, you may need to adjust *alpha* and *beta*. Try increasing both *alpha* and *beta* one order of magnitude at a time until you reach ~0.1. You may also want to initialize the snake algorithm with the boundaries of the approximate shapes, rather than the convex hulls of the approximate shapes. **findBoundaries.m** saves the boundaries in the *boundary* field of *picture*.

B.4.5. Automatically removing bad snakes

Tracked shapes are next, optionally, automatically culled using **removeSnakes.m**. Snaked shapes can become pinched if they snag on objects outside of the cell or if a region of a cell edge is dim. We therefore remove shapes in which boundary points that are *pinchBPThreshLower* or more boundary points apart are less than *pinchThreshLower* pixels away from one another. We also remove shapes in which boundary points that are *pinchBPThreshHigher* or more boundary points apart are less than *pinchThreshHigher* pixels away from one another. Shapes that are smaller than a cell would be (smaller than *minRegionSize*) are also removed. When removing shapes, we divide the shape's track into two tracks, the first of which ends in the frame before the removed shape and the second of which starts in the frame after the removed shape. As before, we also remove tracks with durations less

than *minDuration* frames, tracks that have a mean solidity less than *minSolidity*, or tracks with a mean area larger than that of a cell (larger than *maxRegionSize*). Parameter values used for the analysis of *D. discoideum* are given in Chapter 5. **removeSnakes.m** saves data in fields of the variable *blob*, and saves backup data to the variable *blobAutoRemove*. The output of **removeSnakes.m** can be checked by using **plotSnakes.m**, which is enabled by *verify(3)* with *snakeType* set to 'snakeAutoRemove', to plot the tracked boundaries on the original images.

B.4.6. Manually removing bad snakes

Tracked shapes are next, optionally, manually culled using **selectSnakes.m**. The tracked shapes are checked by the user in every *checkEveryNth* frame, and tracks that the user clicks on are removed *removeRange*/2-1 frames before and after the frame in which they were selected. **selectSnakes.m** can be run in three different modes: 'begin', 'continue', and 'continueAt'. The mode is set by the parameter *remove*. 'begin' initiates track removal at the beginning of the image sequence, 'continue' initiates removal at the frame the user last checked, and 'continueAt' initiates removal at the frame *startAt*, and ends removal at the frame *endAt*. **selectSnakes.m** saves data in fields of the variable *blob*, and saves backup data to the variable *blobManRemove*. The output of **selectSnakes.m** can be checked by using **plotSnakes.m**, which is enabled by *verify(3)* with *snakeType* set to 'snakeManRemove', to plot the tracked boundaries on the original images.

B.4.7. Initializing shapes

The variable *shape* is next created by the variable *blob* using **makeShape.m**. While information stored in *blob* aids in tracking, information stored in *shape* aids in data analysis.

Boundary points are tracked from frame to frame using **initShape.m**. Tracking the local boundary requires mapping the boundary points in each frame to the boundary points in the next frame. Note that while within each frame neighboring points are equidistant along the perimeter, the distance between neighboring points varies across frames as the length of the cell perimeter changes. For ease of visualization and quantification, we would like to track all of the boundary points, and so we need to define a 1:1 tracking mapping. Mappings with crossing mapping vectors can be excluded, since these crossings are topological violations (21). (For instance, mapping point 1 in frame A to point 2 in frame B and point 2 in frame A to point 1 in frame B is a topological violation.) Thus the only possible remaining 1:1 mappings are rotations of one another. Among those, we chose the mapping that introduces the least rotation by minimizing the sum of the square distances between mapped points. **initShape.m** finds this mapping and shifts the snakes in every frame, so that the spatial index of the variable that stores the boundary points, *shape(s).snake*, always corresponds to the same, tracked boundary point.

B.4.8. Measuring shape

measureShape.m calculates various shape measures, such as area, perimeter, circularity, curvature, *etc*. (See **measureShape.m** for more details.) Measures that can be calculated from just one frame, are in **measureShape.m**, whereas measures

that compare the shape in multiple frames are calculated in **measureMotion.m**. **measureShape.m** saves data in fields of the variable *shape.*

At each boundary point, we calculate the boundary curvature by fitting a circle to that boundary point and the two points that are *boundaryPoint* boundary points away from it. The magnitude of the boundary curvature is then defined as the reciprocal of the radius of that circle. If the midpoint of the two points *boundaryPoint* boundary points away is inside the cell, the curvature is defined as positive, otherwise it is defined as negative. For visualization, the color scale is cut off at a maximum curvature magnitude, *curvatureThresh*. (In 'Cell Shape Analysis', curvature space-time plots are smoothed over space and time. You might consider smoothing your curvature space-time plots.)

B.4.9. Measuring motion

measureMotion.m calculates various motion measures, such as speed, local boundary motion, and protrusive/retractive area. (See **measureMotion.m** for more details.) Measures that can be calculated from just one frame, are in **measureShape.m**, whereas measures that compare the shape in multiple frames are calculated in **measureMotion.m**. **measureMotion.m** saves data in fields of the variable *shape.*

A global motion measure was already calculated by **initShape.m**, since the magnitude of the tracking mapping is a measure of global boundary point motion. However, this measure is not well suited to protrusive motion, since a single protrusion results in the measured movement of every boundary point. Instead, we would like a measure that finds motion in only the boundary points that comprise the

protrusion. We then need a local measure that is not based on a 1:1 mapping and that does not induce topological violations. One such measure is the distance from each boundary point to the boundary in a later frame. We mapped points in one frame (source points) to the boundary in a frame obtained *frameDelta* seconds later (target points), rather than to the one in the next frame, to reduce noise and to allow consistency across differing frame rates. Mapping each source boundary point to the closest target point in a later frame does not map boundary points into protrusions and can lead to large gaps or clusters in the point sequence that is mapped to. Therefore, we smoothed over the list of target points. In other words, in each frame the mapping can be represented by a list in which the *i*th value is the index of the boundary point to which the boundary point *i* is mapped. These lists were twice smoothed over using an averaging window. Notice that this method of smoothing does not induce topological violations. (The first smoothing had a window size of *smoothMotion* boundary points, while the second had a size of *smoothMotionAgain* boundary points.) The magnitude of the local motion measure was then defined as the distance between a source point and the corresponding target boundary point in the smoothed list. If the target boundary point is outside of the current boundary, the local motion measure was defined to be positive; otherwise it was defined to be negative. When visualized, the color scale for local motion was cut off at a maximum magnitude, *motionThresh*.

In the local motion mapping, vectors in protrusions diverge, while vectors in retractions converge. The magnitudes of protrusive and retractive motion are then difficult to compare using this measure. In order to compare the magnitudes, we

measure the protrusive/retractive area associated with each vector. First, the front and back of each cell is found. In each frame, the cell orientation is calculated as the orientation of the ellipse that has the same second moments as the pixel positions of the pixels within the cell boundary. Next, the angle of each boundary point relative to the center of the cell is calculated. The two boundary points closest to the cell orientation and the cell orientation plus π are then defined as the front and the back. The cell front is then distinguished from the back by finding the mean value of the local motion measure in the quarter of the cell boundary surrounding each of the two points. The boundary point in the more protrusive region is defined as the front of the cell, while the other boundary point is defined as the back. We measure the differential protrusive and retractive area change along the boundary by tiling the regions between the boundary in each frame and the boundary in the frame *frameDelta* seconds later. Each connection vector is associated with the area closest to it. Next, the boundary points are aligned such that the front is at boundary point 0 in every frame. The average protrusive and retractive areas are found as a function of arc length from the cell front.

B.4.10. Measuring directed shape and motion

initROI.m determines which cells are entirely inside of the ROI, partially inside of the ROI, or entirely outside of the ROI. It saves data in fields of the variable *shape,* and creates two new variables. For each frame, *frame2inROI* lists the IDs of the shapes that are entirely inside of the ROI, while *frame2outROI* lists the IDs of the shapes that are entirely outside of the ROI.

measureLines.m calculates the mean and standard deviations of measures of shapes both entirely inside of and entirely outside of the ROI. This function saves data to *meanOnLine*.

B.4.11. Entering shape space

For each shape in each frame, **enterShapeSpace.m** subtracts the mean position, reorients the shape so that its front is at zero degrees, and rescales the average radius to 20 pixels. It saves data in fields of the variable *shape.*

B.5. Generating plots with Dicty Analysis

Image sequences are turned on and off by changing the values of the binary array *verify,* while plots are turned on and off by changing the values of *plots*. Most of the image sequences and plots enabled by *verify* and *plots* have options as detailed below. All of the image sequences enabled by *verify* pause for ten seconds after the first image has been plotted to allow the user to adjust the image size.

Verify 1 - Approximate Boundaries

plotApproxboundaries.m plots the approximate boundaries on the original images and saves them in the directory 'approxBoundary', which is created in the directory specified by *savePath*. The approximate boundaries are generated by **findBoundaries.m**, which is enabled by *run(2)*.

Verify 2 - Tracked Approximate Boundaries

plotBlobs.m plots the convex hulls of the tracked approximate boundaries on the original images and saves them in the directory 'trackedBlobs', which is created in the directory specified by *savePath*. Each tracked boundary is

plotted in a different, randomly chosen color. Shape tracking is done by **trackBlobs.m**, which is enabled by *run(3)*.

Verify 3 - Snaked Boundaries

plotSnakes.m plots the tracked, snaked boundaries and saves them in the directory specified by *snakeType*, which is created in the directory specified by *savePath*. Each tracked boundary is plotted in a different, randomly chosen color. (The color of a given shape is not the same from plot type to plot type. If **shortenBlobs.m** were everywhere replaced with **removeBlobs.m**, the boundary colors would be consistent across plot types, but the software as a whole would not run as quickly.) Snaking is done by **findSnakes.m**, automatic removal of bad snakes by **removeSnakes.m**, and manual removal of bad snakes by **selectSnakes.m**. The three functions are enabled by *run(4)*, *run(5)*, and *run(6)*, respectively. **plotSnakes.m** has the following options, which are set in **shapes.m**.

snakeType: Several functions successively remove bad snakes from further analysis. This variable specifies the function whose output will be plotted.

'snakeTrack' - All of the tracked shapes. Plots the output of **findSnakes.m**.

'snakeAutoRemove' - The tracked shapes, after the shapes have been automatically culled. Plots the output of **removeSnakes.m**.

'snakeManRemove' - The tracked shapes, after the shapes have been automatically (optional) and manually culled. Plots the output of **selectSnakes.m**.

backgroundSnake: Sets the background on which the snakes are overlaid.

0 - White background.

1 - Original images.

2 - Accumulating (no background). The previous frame is used as the background for the current frame, and so, in each frame, all of the shapes from previous frames and the shapes in the current frame are shown.

Verify 4: Measures on Images

plotMeasuresOnImages.m plots boundaries colored by the values of various measures. Images are saved in the directory specified by *plotMeasure*, which is created in the directory specified by *savePath*. The measures are calculated by **measureShape.m**, **measureMotion.m**, and **initROI.m**, which are enabled by *run(*8*)*, *run(*9*)*, and *run(*10*)*, respectively.

plotMeasure: Sets the measure to be plotted.

'shape' - Plots boundaries colored by the shape measure (the distance from the centroid to each boundary point).

'curvature' - Plots boundaries colored by boundary curvature.

'motion' - Plots boundaries colored by the local motion measure.

'centroid' - Plots the centroids of boundaries. Each centroid is colored a different, randomly chosen color.

'frontBack' - Plots the boundaries in green, the boundary points at cell fronts in red, and the boundary points at cell backs in blue.

'roi' - Plots the boundaries of cells entirely inside the ROI in blue, entirely outside in red, and at the interface in green.

backgroundMeasure: Sets the background on which the shapes are overlaid.

0 - White background.

1 - Original images.

2 - Accumulating (no background). The previous frame is used as the background for the current frame, and so, in each frame, all of the shapes from previous frames and the shapes in the current frame are shown.

downSampleOutline: To save memory and speed up plotting, only every *downSampleOutline*th boundary point is plotted. While 1 or 2 are usually reasonable values for this parameter, if *backgroundMeasure* is set to 2 plotting is much faster when *downSampleOutline* is set to a higher value.

Plots 1: Plots corresponding to individual shapes

plotShapePlots.m shows plots corresponding to individual, tracked shapes. The type of plot, number of cells for which plots are shown, and the way in which the cells are chosen can be set. Requires **measureMotion.m**, which is enabled by *run(*8*)*.

To make some plots, **plotShapePlots.m** calls **plotMeasuresOnShape.m**. While not directly accessible via **shapes.m**, **plotMeasuresOnShape.m** is a versatile function that plots image sequences of shape boundaries colored by arbitrary measures. It can color boundaries by measure, plot a shape on various backgrounds, including on the original image, plot boundary point mappings between frames, and zoom-in on a shape as it moves.

plotPlots: Sets the type of plot.

'pathSpeed' - Plots the centroid path in real space and the centroid speed as a function of time. Calls **pathSpeed.m**.

'plotSpaceTime' - Plots space-time plots of the shape measure, the boundary curvature, the global motion measure (least-squares tracking mapping), and the local motion measure. Calls **plotSpaceTime.m**.

'trackingArrow' - For each shape, plots an image sequence of the least squares tracking mapping. Only every *everyNthVector*th mapping vector is shown. *everyNthVector* is set in the 'trackingArrow' section of **plotShapePlots.m**. Images are saved in the directory 'trackingArrow', which is created in the directory specified by *savePath*. Calls **plotMeasuresOnShape.m**.

'motionArrow' – For each shape, plots an image sequence of the local motion mapping. Only every *everyNthVector*th mapping vector is shown. *everyNthVector* is set in the 'motionArrow' section of **plotShapePlots.m**. Images are saved in the directory 'trackingArrow', which is created in the directory specified by *savePath*. Calls **plotMeasuresOnShape.m**.

numToPlot: Sets the number of shapes for which plots are shown.

shapeChoose: Sets the way in which shapes are chosen.

'random' - Randomly chosen shapes. (The randomization is done by **makeShape.m**, which is enabled by *run(7)*.)

'longestDuration' - Shapes that persist over the greatest number of frames.

'largestDisplacement' – Shapes with the greatest centroid displacement over their entire duration.

Plots 2: Overall statistics

plotOverallPlots.m shows plots of measures that use data from multiple shapes. Requires **measureMotion.m**, which is enabled by *run(*8*)*. **plotOverallPlots.m** is very modular, and so new types of plots could easily be added.

plotOverall: Sets the type of plot.

'clusterMeasures' - Plots the hierarchical clustering of various shape and motion measures and plots the covariance matrix of these measures. In the plot, measures are identified by number. The correspondence between these numbers and the measures is at the top of **clusterMeasures.m**. The *skip* parameter in the clusterMeasures section of **plotOverallPlots.m**, allows the user to cluster data from only every *skip*th frame. Calls **clusterMeasures.m**.

'motionAsEccentricity' - Ranks shapes by eccentricity, bins them, and then plots the protrusive and retractive motion along the boundary for each bin. Protrusive and retractive motion are both plotted relative to the front of the shape. The number of eccentricity bins is set by *numBins* in the motionAsEccentricity section of **plotOverallPlots.m**. Calls **motionAsEccentricity.m**.

'measureAutoCorrs' - Plots the auto-correlation of several measures and displays the exponential decay times. Only shapes that are at least

minDurationAutoCor in duration are used. For shapes whose duration is greater than *minDurationAutoCor*, a random sequence of frames of that duration is chosen. *minDurationAutoCor* is set in the measureAutoCors section of **plotOverallPlots.m**. Calls **measureAutoCorrs.m**.

Plots 3: Directed motion statistics

plotLinePlots.m shows plots of ridge specific measures. Almost all of the plots, however, can be made independent of the ridges by setting the ROI to the entirety of the image and the number of bins, with respect to the ridge direction, to 1. Requires **measureMotion.m**, which is enabled by *run(*8), and **initROI.m** and **measureLines.m**, which are both enabled by *run(9)*.

plotLine: Sets the type of plot.

'measureCompare' - Plots the mean and standard error of the speed, eccentricity, area, and solidity of shapes that are entirely inside of the ROI and shapes that are entirely outside of the ROI. Calls **measureCompare.m**.

'motionAsLineAngle' - Bins the shapes by orientation with respect to the ridges, and then plots the protrusive and retractive motion along the boundary. Protrusive and retractive motion are both plotted relative to the front of the shape. The number of orientation bins is set by *numBins*, which is in the motionAsLineAngle section of **plotOverallPlots.m**. Calls **motionAsLineAngle.m**.

'areaAsLineAngle' - Bins the shapes by orientation with respect to the ridges, and then plots the protrusive and retractive area distributions. *numBins* sets the number of orientation bins, while *numAreaBins* sets the number of area bins. Both parameters are set in the motionAsLineAngle section of **plotOverallPlots.m**. Calls **areaAsLineAngle.m**.

'eccentricityVsLineAngle' - Attempts to control for the affect of eccentricity on the plots produced by **motionAsLineAngle.m**. Does not work well. Calls **eccentricityVsLineAngle.m**.

'meanShape' - Plots the mean shape at various orientations with respect to the ridges. *numBins*, which is set in the meanShape section of **plotLinePlots.m**, sets the number of orientation bins. Calls **meanShape.m**.

'spider' – Plots spider plots of shapes that are initially at various orientations with respect to the ridges. A spider plot is a plot of the centroid motion of multiple shapes with the initial positions overlapped. Various parameters are set in the spider section of **plotOverallPlots.m**. *numBins* sets the number of shape orientation bins, and hence the number of spider plots, *spiderDuration* sets the duration of the shape tracks, *numTracks* sets the number of shapes plotted, and *eccCutoff* sets a minimum initial eccentricity. Shapes are randomly chosen. If there are not *numTracks* shapes that meet the various requirements, fewer shapes will be plotted. Calls **spider.m**.

References

1. Friedl P & Wolf K (2009) Plasticity of cell migration: a multiscale tuning model. *Journal of Cell Biology* 188(1):11-19.

2. Wagle MA & Tranquillo RT (2000) A self-consistent cell flux expression for simultaneous chemotaxis and contact guidance in tissues. *Journal of Mathematical Biology* 41(4):315-330.

3. Yang X, Dormann D, Munsterberg AE, & Weijer CJ (2002) Cell movement patterns during gastrulation in the chick are controlled by positive and negative chemotaxis mediated by FGF4 and FGF8. *Developmental Cell* 3(3):425-437.

4. Capogrosso Sansone B, Scalerandi M, & Condat CA (2001) Emergence of taxis and synergy in angiogenesis. *Physical Review Letters* 87(12):128102.

5. Kassis J, DA; L, Turner T, & A W (2001) Tumor invasion as dysregulated cell motility. *Seminars in Cancer Biology* 11(2):105-117.

6. Thompson DAW (1917) *On growth and form* (Cambridge).

7. Phillips R, Kondev J, & Theriot J (2009) *Physical biology of the cell* (Garland Science).

8. Wong SL, Zhang LV, & Roth FP (2005) Discovering functional relationships: biochemistry versus genetics. *Trends in Genetics* 21(8):424-427.

9. Sheetz MP, Felsenfeld D, Galbraith CG, & Choquet D (1999) Cell migration as a five-step cycle. *Biochemical Society Symposia* 65:233-243.

10. Fletcher DA & Mullins RD (2010) Cell mechanics and the cytoskeleton. *Nature* 463(7280):485-492.

11. Dominguez R & Holmes KC (2011) Actin structure and function. *Annual Review of Biophysics* 40:169-186.

12. Pollard TD & Cooper JA (2009) Actin, a central player in cell shape and movement. *Science* 326(5957):1208-1212.

13. Mogilner A & Oster G (1996) Cell motility driven by actin polymerization. *Biophysical Journal* 71(6):3030-3045.

14. Allard J & Mogilner A (2012) Traveling waves in actin dynamics and cell motility. *Current Opinion in Cell Biology*.

15. Ryan GL, Watanabe N, & Vavylonis D (2012) A review of models of fluctuating protrusion and retraction patterns at the leading edge of motile cells. *Cytoskeleton* 69(4):195-206.

16. Meili R, Alonso-Latorre B, del Alamo JC, Firtel RA, & Lasheras JC (2009) Myosin II is essential for the spatiotemporal organization of traction forces during cell motility. *Molecular Biology of the Cell* 21(3):405-417.

17. Killich T*, et al.* (1993) The locomotion, shape and pseudopodial dynamics of unstimulated Dictyostelium cells are not random. *Journal of Cell Science* 106:1005-1013.

18. Alt W, Brosteanu O, Hinz B, & Kaiser HW (1995) Patterns of spontaneous motility in videomicrographs of human epidermal keratinocytes (HEK). *Biochemistry and Cell Biology* 73(7-8):441-459.

19. Gerisch G*, et al.* (2004) Mobile actin clusters and traveling waves in cells recovering from actin depolymerization. *Biophysical Journal* 87(5):3493-3503.

20. Weiner OD, Marganski WA, Wu LF, Altschuler SJ, & Kirschner MW (2007) An actin-based wave generator organizes cell motility. *PLoS Biology* 5(9):2053-2063.

21. Machacek M & Danuser G (2006) Morphodynamic profiling of protrusion phenotypes. *Biophysical Journal* 90(4):1439-1452.

22. Barnhart EL, Lee KC, Keren K, Mogilner A, & Theriot JA (2011) An adhesion-dependent switch between mechanisms that determine motile cell shape. *PLoS Biology* 9(5):e1001059.

23. Case LB & Waterman CM (2011) Adhesive F-actin waves: a novel integrin-mediated adhesion complex coupled to ventral actin polymerization. *PLoS One* 6(11):e26631.

24. Driscoll MK*, et al.* (2012) Cell shape dynamics: from waves to migration. *PLoS Computational Biology* 8(3).

25. Ryan GL, Petroccia HM, Watanabe N, & Vavylonis D (2012) Excitable actin dynamics in lamellipodial protrusion and retraction. *Biophysical Journal* 102(7):1493-1502.

26. Iglesias PA & Devreotes PN (2012) Biased excitable networks: how cells direct motion in response to gradients. *Current Opinion in Cell Biology* 24(2):245-253.

27. Bretschneider T*, et al.* (2009) The three-dimensional dynamics of actin waves, a model of cytoskeletal self-organization. *Biophysical Journal* 96(7):2888-2900.

28. Dobereiner HG*, et al.* (2006) Lateral membrane waves constitute a universal dynamic pattern of motile cells. *Physical Review Letters* 97(3).

29. Discher DE, Janmey P, & Wang YL (2005) Tissue cells feel and respond to the stiffness of their substrate. *Science* 310(5751):1139-1143.

30. Pelham RJ, Jr. & Wang Y (1997) Cell locomotion and focal adhesions are regulated by substrate flexibility. *Proceedings of the National Academy of Sciences* 94(25):13661-13665.

31. Lo CM, Wang HB, Dembo M, & Wang YL (2000) Cell movement is guided by the rigidity of the substrate. *Biophysical Journal* 79(1):144-152.

32. Deroanne CF, Lapiere CM, & Nusgens BV (2001) In vitro tubulogenesis of endothelial cells by relaxation of the coupling extracellular matrix-cytoskeleton. *Cardiovascular Research* 49(3):647-658.

33. Engler AJ, Sen S, Sweeney HL, & Discher DE (2006) Matrix elasticity directs stem cell lineage specification. *Cell* 126(4):677-689.

34. Saha K*, et al.* (2008) Substrate modulus directs neural stem cell behavior. *Biophysical Journal* 95(9):4426-4438.

35. McCann CP, Rericha EC, Wang C, Losert W, & Parent CA (In Preparation) Dictyostelium cells regulate actin assembly to migrate similarly on surfaces of varying adhesivity.

36. Kane RS, Takayama S, Ostuni E, Ingber DE, & Whitesides GM (1999) Patterning proteins and cells using soft lithography. *Biomaterials* 20(23-24):2363-2376.

37. McBeath R, Pirone DM, Nelson CM, Bhadriraju K, & Chen CS (2004) Cell shape, cytoskeletal tension, and RhoA regulate stem cell lineage commitment. *Developmental Cell* 6(4):483-495.

38. Kilian KA, Bugarija B, Lahn BT, & Mrksich M (2010) Geometric cues for directing the differentiation of mesenchymal stem cells. *Proceedings of the National Academy of Sciences* 107(11):4872-4877.

39. Loesberg WA*, et al.* (2007) The threshold at which substrate nanogroove dimensions may influence fibroblast alignment and adhesion. *Biomaterials* 28:3944-3951.

40. Clark P, Connolly P, Curtis AS, Dow JA, & Wilkinson CD (1991) Cell guidance by ultrafine topography in vitro. *Journal of Cell Science* 99 (Pt 1):73-77.

41. Dalby M, Riehle M, Sutherland D, Aghelib H, & Curtis A (2004) Changes in fibroblast morphology in response to nano-columns produced by colloidal lithography. *Biomaterials* 25:5415–5422.

42. Cavalcanti-Adam EA*, et al.* (2007) Cell spreading and focal adhesion dynamics are regulated by spacing of integrin ligands. *Biophysical Journal* 92(8):2964-2974.

43. Chang-Hwan Choi C-H*, et al.* (2007) Cell interaction with three-dimensional sharp-tip nanotopography. *Biomaterials* 28:1672-1679.

44. Kunzler TP, Huwiler C, Drobek T, Voros J, & Spencer ND (2007) Systematic study of osteoblast response to nanotopography by means of nanoparticle-density gradients. *Biomaterials* 28:5000-5006.

45. Clark P, Connolly P, Curtis AS, Dow JA, & Wilkinson CD (1990) Topographical control of cell behaviour: II. Multiple grooved substrata. *Development* 108(4):635-644.

46. Wilkinson CDW, Riehle M, Wood M, Gallagher J, & Curtis ASG (2002) The use of materials patterned on a nano- and micro-metric scale in cellular engineering. *Materials Science & Engineering C-Biomimetic and Supramolecular Systems* 19(1-2):263-269.

47. Dalby MJ*, et al.* (2007) Nanomechanotransduction and interphase nuclear organization influence on genomic control. *Journal of Cellular Biochemistry* 102(5):1234-1244.

48. Kwon KW*, et al.* (2012) Nanotopography-guided migration of T cells. *Journal of Immunology* 189(5):2266-2273.

49. Bettinger CJ, Langer R, & Borenstein JT (2009) Engineering substrate topography at the micro- and nanoscale to control cell function. *Angewandte Chemie* 48(30):5406-5415.

50. Bagorda A & Parent CA (2008) Eukaryotic chemotaxis at a glance. *Journal of Cell Science* 121(16):2621-2624.

51. Kessin RH (2001) *Dictyostelium: evolution, cell biology, and the development of multicellularity.* (Cambridge University Press, Cambridge).

52. Bagorda A, Mihaylov VA, & Parent CA (2006) Chemotaxis: moving forward and holding on to the past. *Thrombosis and Haemostasis* 95(1):12-21.

53. Palsson E*, et al.* (1997) Selection for spiral waves in the social amoebae Dictyostelium. *Proceedings of the National Academy of Sciences* 94(25):13719-13723.

54. Garcia GL, Rericha EC, Heger CD, Goldsmith PK, & Parent CA (2009) The group migration of Dictyostelium cells is regulated by extracellular chemoattractant degradation. *Molecular Biology of the Cell* 20(14):3295-3304.

55. Kriebel PW, Barr VA, & Parent CA (2003) Adenylyl cyclase localization regulates streaming during chemotaxis. *Cell* 112(4):549-560.

56. Goldbeter A (1996) *Biochemical oscillations and cellular rhythms* (Cambridge University Press, Cambridge).

57. Wurster B, S.; B, & Gerisch G (1978) Control of cell contact sites by cAMP pulses in differentiating Dictyostelium cells. *Nature* 255.

58. Xiong Y & Iglesias PA (2010) Tools for analyzing cell shape changes during chemotaxis. *Integrative Biology* 2(11-12):561-567.

59. Yin Z & Kanade T (2011) Restoring artifact-free microscopy image sequences. *IEEE International Symposium on Biomedical Imaging*.

60. Kass M, Witkin A, & Terzopoulos D (1988) Snakes: active contour models. *International Journal of Computer Vision*:321-333.

61. Osher S & Sethian J (1988) Fronts propagating with curvature-dependent speed: Algorithms based on Hamilton-Jacobi formulations. *Journal of Computational Physics* 79(1):12-49.

62. Dormann D, Libotte T, Weijer CJ, & Bretschneider T (2002) Simultaneous quantification of cell motility and protein-membrane-association using active contours. *Cell Motility and the Cytoskeleton* 52(4):221-230.

63. Bosgraaf L, van Haastert PJM, & Bretschneider T (2009) Analysis of cell movement by simultaneous quantification of local membrane displacement and fluorescent intensities using Quimp2. *Cell Motility and the Cytoskeleton* 66(3):156-165.

64. Bosgraaf L & Van Haastert PJM (2010) Quimp3, an automated pseudopod-tracking algorithm. *Cell Adhesion & Migration* 4(1):46-55.

65. Tyson RA, Epstein DBA, Anderson KI, & Bretschneider T (2010) High resolution tracking of cell membrane dynamics in moving cells: an electrifying approach. *Mathematical Modelling of Natural Phenomena* 5(1):34-55.

66. Li L, Norrelykke SF, & Cox EC (2008) Persistent cell motion in the absence of external signals: a search strategy for eukaryotic cells. *PLoS One* 3(5):e2093.

67. Li L, Cox EC, & Flyvbjerg H (2011) 'Dicty dynamics': Dictyostelium motility as persistent random motion. *Physical Biology* 8(4).

68. Andrew N & Insall RH (2007) Chemotaxis in shallow gradients is mediated independently of PtdIns 3-kinase by biased choices between random protrusions. *Nature Cell Biology* 9(2):193-200.

69. Bosgraaf L & Van Haastert PJ (2009) The ordered extension of pseudopodia by amoeboid cells in the absence of external cues. *PLoS One* 4(4):e5253.

70. Bosgraaf L & Van Haastert PJM (2009) Navigation of chemotactic cells by parallel signaling to pseudopod persistence and orientation. *PLoS One* 4(8).

71. Maeda YT, Inose J, Matsuo MY, Iwaya S, & Sano M (2008) Ordered patterns of cell shape and orientational correlation during spontaneous cell migration. *PLoS One* 3(11):e3734.

72. Fujita S, Ohshima M, & Iwata H (2009) Time-lapse observation of cell alignment on nanogrooved patterns. *Journal of the Royal Society Interface* 6:S269-S277.

73. Teixeira AI, Abrams GA, Bertics PJ, Murphy CJ, & Nealey PF (2003) Epithelial contact guidance on well-defined micro- and nanostructured substrates. *Journal of Cell Science* 116(Pt 10):1881-1892.

74. Mitchison TJ & Cramer LP (1996) Actin-based cell motility and cell locomotion. *Cell* 84(3):371-379.

75. Vicente-Manzanares M, Webb DJ, & Horwitz AR (2005) Cell migration at a glance. *Journal of Cell Science* 118(21):4917-4919.

76. Capell BC & Collins FS (2006) Human laminopathies: nuclei gone genetically awry. *Nature Reviews Genetics* 7(12):940-952.

77. Capell BC*, et al.* (2005) Inhibiting farnesylation of progerin prevents the characteristic nuclear blebbing of Hutchinson-Gilford progeria syndrome. *Proceedings of the National Academy of Sciences* 102(36):12879-12884.

78. Driscoll MK, Fourkas JT, & Losert W (2011) Local and global measures of shape dynamics. *Physical Biology* 8(5):055001.

79. Stephens GJ, Johnson-Kerner B, Bialek W, & Ryu WS (2008) Dimensionality and dynamics in the behavior of C. elegans. *PLoS Computational Biology* 4(4):e1000028.

80. Steinmetz H (1996) Structure, function and cerebral asymmetry: In vivo morphometry of the planum temporale. *Neuroscience and Biobehavioral Reviews* 20(4):587-591.

81. Halazonetis DJ (2004) Morphometrics for cephalometric diagnosis. *American Journal of Orthodontics and Dentofacial Orthopedics* 125(5):571-581.

82. Gearhart JP, Partin AW, Leventhal B, Bruce Beckwith J, & Epstein JI (1992) The use of nuclear morphometry to predict response to therapy in Wilms' tumor. *Cancer* 69(3):804-808.

83. Wessels D*, et al.* (1998) A computer-assisted system for reconstructing and interpreting the dynamic three-dimensional relationships of the outer surface, nucleus and pseudopods of crawling cells. *Cell Motility and the Cytoskeleton* 41(3):225-246.

84. Machacek M*, et al.* (2009) Coordination of Rho GTPase activities during cell protrusion. *Nature* 461(7260):99-103.

85. King JS & Insall RH (2009) Chemotaxis: finding the way forward with Dictyostelium. *Trends in Cell Biology* 19(10):523-530.

86. Xu C & Prince JL (1998) Snakes, shapes, and gradient vector flow. *IEEE Transactions on Image Processing* 7(3):359-369.

87. Carmo Md (1976) *Differential geometry of curves and surfaces* (Prentice-Hall).

88. Heywood H (1954) Particle shape coefficients. *Journal of Imperial College Chemical Society* 8:15-33.

89. del Álamo JC*, et al.* (2007) Spatio-temporal analysis of eukaryotic cell motility by improved force cytometry. *Proceedings of the National Academy of Sciences* 104(33):13343-13348.

90. Yoo SK*, et al.* (2010) Differential regulation of protrusion and polarity by PI(3)K during neutrophil motility in live zebrafish. *Developmental Cell* 18(2):226-236.

91. McCann C, Kriebel P, Parent C, & Losert W (2010) Cell speed, persistence and information transmission during signal relay and collective migration. *Journal of Cell Science* 123(Pt 10):1724-1731.

92. Friedl P (2004) Prespecification and plasticity: shifting mechanisms of cell migration. *Current Opinion in Cell Biology* 16(1):14-23.

93. Parent CA & Devreotes PN (1999) A cell's sense of direction. *Science* 284(5415):765-770.

94. Rericha EC & Parent CA (2008) Steering in quadruplet: the complex signaling pathways directing chemotaxis. *Science Signaling* 1(22):pe26.

95. Rickert P, Weiner OD, Wang F, Bourne HR, & Servant G (2000) Leukocytes navigate by compass: roles of PI3Kgamma and its lipid products. *Trends in Cell Biology* 10(11):466-473.

96. Van Haastert PJM & Bosgraaf L (2009) The local cell curvature guides pseudopodia towards chemoattractants. *HFSP Journal* 3(4):282-286.

97. Soll DR, Wessels D, Kuhl S, & Lusche DF (2009) How a cell crawls and the role of cortical myosin II. *Eukaryotic Cell* 8(9):1381-1396.

98. Bosgraaf L & Van Haastert PJM (2009) The Ordered Extension of Pseudopodia by Amoeboid Cells in the Absence of External Cues. *PLoS ONE* 4(4):e5253.

99. Xiong Y*, et al.* (2010) Automated characterization of cell shape changes during amoeboid motility by skeletonization. *BMC Systems Biology* 4(1):33.

100. Xiong YA, Huang CH, Iglesias PA, & Devreotes PN (2010) Cells navigate with a local-excitation, global-inhibition-biased excitable network. *Proceedings of the National Academy of Sciences* 107(40):17079-17086.

101. Blanchard GB, Murugesu S, Adams RJ, Martinez-Arias A, & Gorfinkiel N (2010) Cytoskeletal dynamics and supracellular organisation of cell shape fluctuations during dorsal closure. *Development* 137(16):2743-2752.

102. Vicker MG (2000) Reaction-diffusion waves of actin filament polymerization/depolymerization in Dictyostelium pseudopodium extension and cell locomotion. *Biophysical Chemistry* 84(2):87-98.

103. Vicker MG (2002) Eukaryotic cell locomotion depends on the propagation of self-organized reaction-diffusion waves and oscillations of actin filament assembly. *Experimental Cell Research* 275(1):54-66.

104. Socol M, Lefrou C, Bruckert F, Delabouglise D, & Weidenhaupt M (2010) Synchronization of Dictyostelium discoideum adhesion and spreading using electrostatic forces. *Bioelectrochemistry* 79(2):198-210.

105. Barry NP & Bretscher MS (2010) Dictyostelium amoebae and neutrophils can swim. *Proceedings of the National Academy of Sciences* 107(25):11376-11380.

106. Baldacchini T*, et al.* (2004) Acrylic-based resin with favorable properties for three-dimensional two-photon polymerization. *Journal of Applied Physics* 95(11):6072-6076.

107. LaFratta CN*, et al.* (2004) Replication of two-photon-polymerized structures with extremely high aspect ratios and large overhangs. *Journal of Physical Chemistry B* 108(31):11256-11258.

108. Li L*, et al.* (2008) Binary and gray-scale patterning of chemical functionality on polymer films. *Journal of the American Chemical Society* 130(41):13512-13513.

109. Driscoll MK*, et al.* (2012) Automated image analysis of nuclear shape: What can we learn from a prematurely aged cell? *Aging* 4:119.

110. Gordon LB, Harling-Berg CJ, & Rothman FG (2008) Highlights of the 2007 Progeria Research Foundation scientific workshop: progress in translational science. *Journal of Gerontology Series A* 63(8):777-787.

111. Gordon LB*, et al.* (2007) Disease progression in Hutchinson-Gilford progeria syndrome: impact on growth and development. *Pediatrics* 120(4):824-833.

112. Merideth MA*, et al.* (2008) Phenotype and course of Hutchinson-Gilford progeria syndrome. *New England Journal of Medicine* 358(6):592-604.

113. Dahl KN*, et al.* (2006) Distinct structural and mechanical properties of the nuclear lamina in Hutchinson-Gilford progeria syndrome. *Proceedings of the National Academy of Sciences* 103(27):10271-10276.

114. Dechat T, Adam SA, Taimen P, Shimi T, & Goldman RD (2010) Nuclear lamins. *Cold Spring Harbor Perspectives in Biology* 2(11):a000547.

115. Eriksson M*, et al.* (2003) Recurrent de novo point mutations in lamin A cause Hutchinson-Gilford progeria syndrome. *Nature* 423(6937):293-298.

116. Goldman RD*, et al.* (2004) Accumulation of mutant lamin A causes progressive changes in nuclear architecture in Hutchinson-Gilford progeria

syndrome. *Proceedings of the National Academy of Sciences* 101(24):8963-8968.

117. Cao K, Capell BC, Erdos MR, Djabali K, & Collins FS (2007) A lamin A protein isoform overexpressed in Hutchinson-Gilford progeria syndrome interferes with mitosis in progeria and normal cells. *Proceedings of the National Academy of Sciences* 104(12):4949-4954.

118. Dechat T*, et al.* (2007) Alterations in mitosis and cell cycle progression caused by a mutant lamin A known to accelerate human aging. *Proceedings of the National Academy of Sciences* 104(12):4955-4960.

119. Mallampalli MP, Huyer G, Bendale P, Gelb MH, & Michaelis S (2005) Inhibiting farnesylation reverses the nuclear morphology defect in a HeLa cell model for Hutchinson-Gilford progeria syndrome. *Proceedings of the National Academy of Sciences* 102(40):14416-14421.

120. Young SG, Fong LG, & Michaelis S (2005) Prelamin A, Zmpste24, misshapen cell nuclei, and progeria - new evidence suggesting that protein farnesylation could be important for disease pathogenesis. *Journal of Lipid Research* 46(12):2531-2558.

121. Capell BC*, et al.* (2008) A farnesyltransferase inhibitor prevents both the onset and late progression of cardiovascular disease in a progeria mouse model. *Proceedings of the National Academy of Sciences* 105(41):15902-15907.

122. Cao K*, et al.* (2011) Rapamycin reverses cellular phenotypes and enhances mutant protein clearance in Hutchinson-Gilford progeria syndrome cells. *Science Translational Medicine* 3(89).

123. Graziotto JJ, Cao K, Collins FS, & Krainc D (2012) Rapamycin activates autophagy in Hutchinson-Gilford progeria syndrome Implications for normal aging and age-dependent neurodegenerative disorders. *Autophagy* 8(1):147-151.

124. Blagosklonny MV (2011) Progeria, rapamycin and normal aging: recent breakthrough. *Aging* 3(7):685-691.

125. Scaffidi P & Misteli T (2006) Lamin A-dependent nuclear defects in human aging. *Science* 312(5776):1059-1063.

126. Cao K*, et al.* (2011) Progerin and telomere dysfunction collaborate to trigger cellular senescence in normal human fibroblasts. *Journal of Clinical Investigation* 121(7):2833-2844.

127. McClintock D*, et al.* (2007) The mutant form of lamin A that causes Hutchinson-Gilford progeria is a biomarker of cellular aging in human skin. *PLoS One* 2(12).

128. Olive M*, et al.* (2010) Cardiovascular pathology in Hutchinson-Gilford progeria: correlation with the vascular pathology of aging. *Arteriosclerosis Thrombosis and Vascular Biology* 30(11):2301-U2636.

129. Richards SA, Muter J, Ritchie P, Lattanzi G, & Hutchison CJ (2011) The accumulation of un-repairable DNA damage in laminopathy progeria fibroblasts is caused by ROS generation and is prevented by treatment with N-acetyl cysteine. *Human Molecular Genetics* 20(20):3997-4004.

130. Hutchison CJ (2011) The role of DNA damage in laminopathy progeroid syndromes. *Biochemical Society Transactions* 39:1715-1718.

131. Demidenko ZN & Blagosklonny MV (2009) Quantifying pharmacologic suppression of cellular senescence: prevention of cellular hypertrophy versus preservation of proliferative potential. *Aging* 1(12):1008-1016.

132. Pospelova TV*, et al.* (2009) Pseudo-DNA damage response in senescent cells. *Cell Cycle* 8(24):4112-4118.

133. Pankotai T, Hoffbeck AS, Boumendil C, & Soutoglou E (2009) DNA damage response in the absence of DNA lesions continued ... *Cell Cycle* 8(24):4025-4026.

134. Demidenko ZN*, et al.* (2009) Rapamycin decelerates cellular senescence. *Cell Cycle* 8(12):1888-1895.

135. Weiss P & Garber B (1952) Shape and movement of mesenchyme cells as functions of the physical structure of the medium. *Proceedings of the National Academy of Sciences* 38(3):264-280.

136. Zaidel-Bar R, Cohen M, Addadi L, & Geiger B (2004) Hierarchical assembly of cell-matrix adhesion complexes. *Biochemical Society Transactions* 32(3):416-420.

137. Seftor E*, et al.* (2002) Molecular determinants of human uveal melanoma invasion and metastasis. *Clinical and Experimental Metastasis* 19(3):233-246.

138. Friedl P & Wolf K (2003) Tumour-cell invasion and migration: diversity and escape mechanisms. *Nature Reviews Cancer* 3(5):362-374.

139. Eckert B, Warren R, & Rubin R (1977) Structural and biochemical aspects of cell motility in amoebas of dictyostelium discoideum. *Journal of Cell Biology* 79:339-350.

140. Anselme K*, et al.* (2010) The interaction of cells and bacteria with surfaces structured at the nanometre scale. *Acta Biomaterialia* 6(10):3824-3846.

141. Faix J & Rottner K (2006) The making of filopodia. *Current Opinion in Cell Biology* 18(1):18-25.

142. Li L & Fourkas J (2007) Multiphoton polymerization. *Materials Today* 10:30-37.

143. Kemkemer R, Jungbauer S, Kaufmann D, & Gruler H (2006) Cell orientation by a microgrooved substrate can be predicted by automatic control theory. *Biophysical Journal* 90(12):4701-4711.

144. Masoliver J & Porr JM (1993) Harmonic oscillators driven by colored noise: Crossovers, resonances, and spectra. *Physical Review E* 48(6):4309-4319.

145. Schirenbeck A, Bretschneider T, Arasada R, Schleicher M, & Faix J (2005) The Diaphanous-related formin dDia2 is required for the formation and maintenance of filopodia. *Nature Cell Biology* 7(6):619-625.

146. Stocker MP, Li LJ, Gattass RR, & Fourkas JT (2011) Multiphoton photoresists giving nanoscale resolution that is inversely dependent on exposure time. *Nature Chemistry* 3(3):223-227.

147. Otsu N (1979) A threshold selection method from gray-level histograms. *IEEE Transactions on Systems, Man, and Cybernetics* 9(1):62–66.

148. Schienbein M & Gruler H (1993) Langevin equation, Fokker-Planck equation and cell migration. *Bulletin of Mathematical Biology* 55(3):585-608.

149. Van der Maaten LJP, Postma EO, & Van Den Herik HJ (2009) Dimensionality reduction: A comparative review. *Journal of Machine Learning Research* 10:1-41.

150. Saeys Y, Inza I, & Larranaga P (2007) A review of feature selection techniques in bioinformatics. *Bioinformatics* 23(19):2507-2517.

151. Stephens GJ, Osborne LC, & Bialek W (2011) Searching for simplicity in the analysis of neurons and behavior. *Proceedings of the National Academy of Sciences* 108:15565-15571.

152. Stephens GJ, de Mesquita MB, Ryu WS, & Bialek W (2011) Emergence of long timescales and stereotyped behaviors in Caenorhabditis elegans. *Proceedings of the National Academy of Sciences* 108(18):7286-7289.

153. Keren K*, et al.* (2008) Mechanism of shape determination in motile cells. *Nature* 453(7194):475.

154. Pincus Z & Theriot JA (2007) Comparison of quantitative methods for cell-shape analysis. *Journal of Microscopy* 227(Pt 2):140-156.

155. Liu Y, Collins RT, & Tsin Y (2004) A computational model for periodic pattern perception based on frieze and wallpaper groups. *IEEE Transactions on Pattern Analysis and Machine Intelligence* 26(3):354-371.

156. Postma M*, et al.* (2003) Uniform cAMP stimulation of Dictyostelium cells induces localized patches of signal transduction and pseudopodia. *Molecular Biology of the Cell* 14(12):5019-5027.

157. Driscoll M*, et al.* (2009) The adventures of Dicty, the Dictyostelium cell. *Chaos* 19(4):041110.